**NTNU – Trondheim**
Norwegian University of
Science and Technology

# Ice Detection and Tracking Based on Satellite and Radar Images

Guro Larssen

Master of Science in Engineering and ICT
Submission date: June 2015
Supervisor: Roger Skjetne, IMT

Norwegian University of Science and Technology
Department of Marine Technology

**NTNU Trondheim**
**Norwegian University of Science and Technology**
*Department of Marine Technology*

# PROJECT DESCRIPTION SHEET

**Name of the candidate:** Guro Larssen

**Field of study:** Marine control engineering

**Thesis title (Norwegian):** Deteksjon og overvåkning av is basert på satelitt- og radarbilder.

**Thesis title (English):** Ice detection and tracking based on satellite and radar images.

**Background**

Ice Management for Arctic offshore stationkeeping operations is the sum of all activities where the objective is to reduce or avoid actions from any kind of ice feature on the protected structure. It is distinguished between sea-ice management and iceberg management.
Sea-ice management typically consists of:

- Sea-ice observation and monitoring:
  - Online estimation of ice parameters such as ice concentration, floe size distribution, ice geometry/thickness, ice age, density, salinity, etc.
  - Sea-ice tracking (drift speed and direction, ice floe identification)
  - Severe ice feature detection and tracking, such as ice ridges and icebergs.
- Threat evaluation:
  - Forecasting evolution of ice situation.
  - Threat assessment with respect to protected structure.
- Physical ice management, such as operation of icebreakers, emergency disconnect capabilities.

For iceberg management, the following is involved:

- Iceberg detection and tracking.
- Threat evaluation:
  - Forecasting of iceberg drift.
  - Threat assessment with respect to protected structure.
- Iceberg handling such as iceberg towing, propeller washing, water cannon, ramming, etc.

Obviously, handling icebergs already frozen into sea-ice is more challenging than open-water iceberg management. In any case, it follows that the ice surveillance system is a critical part of any ice management system. The main responsibilities of ice surveillance are to continuously monitor the sea-ice situation, detect and track ice hazards, and forecast the future ice situation.

There are many sensors and sensor platforms available as a component in ice surveillance, such as various cameras, radars, and underwater sonars. In this project we will study the use of satellite and marine sensors. The application is ice detection and tracking, using sequential satellite images. In addition, an objective is to investigate how to classify different target types, specifically, distinguishing between ice and vessel targets.

**Work description**

1. Perform a literature review to provide background and relevant references on:
   - Use of satellites to monitor sea-ice, icebergs, and Arctic offshore operations, considering relevant satellite systems, sensor technologies, service providers, and properties of service.
   - Use of marine radars and customized ice detection radars for detection and tracking of icebergs, considering onboard radars and permanent land-based radar systems, service providers, and properties/performance of the service and technologies.
   - Relevant image processing algorithms for detection of icebergs from satellite images.
   - Tracking and forecasting of ice.
   - Discrimination of different target types in satellite images.

   Write a list with abbreviations and definitions of terms and concepts, explaining relevant concepts related to iceberg detection by satellites and radars.

2. Make an algorithm that detects and tracks targets in images. The software should be able to recognize targets that have already been detected, and re-detect them in a sequence of time-separated images.

3. Use satellite images with different characteristics (polarization), and analyze and discuss how this affects the target detection capability.

4. Add a classification feature to the software, so that it can discriminate between different targets (vessels, icebergs, etc.). Investigate if combining the imagery with AIS-data can be helpful in the discrimination process.

***Tentatively:***

5. Investigate how current and wind fields can be used to distinguish free-floating icebergs from human-controlled vessels.

**Guidelines**

The scope of work may prove to be larger than initially anticipated. By the approval from the supervisor, described topics may be deleted or reduced in extent without consequences with regard to grading.

The candidate shall present his personal contribution to the resolution of problems within the scope of work. Theories and conclusions should be based on mathematical derivations and logic reasoning identifying the various steps in the deduction.

The report shall be organized in a rational manner to give a clear exposition of results, assessments, and conclusions. The text should be brief and to the point, with a clear language. The report shall be written in English (preferably US) and contain the following elements: Abstract, acknowledgements, table of contents, main body, conclusions with recommendations for further work, list of symbols and acronyms, references, and optional appendices. All figures, tables, and equations shall be numerated. The original contribution of the candidate and material taken from other sources shall be clearly identified. Work from other sources shall be properly acknowledged using quotations and a Harvard citation style (e.g. *natbib* Latex package). The work is expected to be conducted in an honest and ethical manner, without any sort of plagiarism and misconduct. Such practice is taken very seriously by the university and will have consequences. NTNU can use the results freely in research and teaching by proper referencing, unless otherwise agreed upon.

The thesis shall be submitted with a printed and electronic copy to 1) the main supervisor and 2) the external examiner, each copy signed by the candidate. The final revised version of this thesis description must be included. The report must appear in a bound volume or a binder according to the NTNU standard template. Computer code, pictures, videos, data series, and a PDF version of the report shall be included electronically.

**Start date:** 15 January, 2015 **Due date:** As specified by the administration.
**Supervisor:** Professor Roger Skjetne

**Trondheim, 21.04.2015**

_____

**Roger Skjetne,** Supervisor

# Abstract

The tracking and management of ice is a topic of great importance, due to the dangers these ice targets pose to vessels and marine structures. As the marine activity increase in ice affected areas, the motivation for developing good methods for detection and tracking of ice is increased accordingly. An important tool for this purpose is satellites. Satellites can produce imagery of a range of resolutions, covering large areas.

An algorithm, implemented in MATLAB, for automatic tracking of targets in satellite images is proposed. The algorithm have three stages: detection of targets, matching targets in the image with targets from previous images, and classification of targets. The matching is carried out using a geometrical shape representation rendered for each target, and the classification feature uses a set speed limit to distinguish between vessel and ice targets. The algorithm's performance was assessed by applying it to a set of RADARSAT-2 images covering the Greenland East Coast. The results proved the detection to be effective for targets not completely enclosed by ice. However, tracking is not possible for very small targets only spanning a few pixels. This proved to be an issue when trying to identify targets as vessels with the classification feature.

To further investigate target discrimination in satellite images, an analysis of the brightness return from different targets in multi-polarized imagery was carried out. Vessel and ice targets were observed to have considerably different polarization responses. By using a multi-polarized area ratio, it was showed that this could be used for discrimination between vessel and ice targets. A further indication of target types was found by comparing motion patterns of free-floating ice targets with human-controlled vessels.

To be able to forecast the motion of ice, a dynamic model for iceberg drift is presented. By using a Kalman filter, the velocity of the iceberg can be estimated. The Kalman filter uses measurements from weather data and the position of the iceberg. The position measurements needed in the filter can be found from using the tracking algorithm on the satellite images. However, in this thesis, the model

was only simulated on synthetic data, and not by using satellite images.

# Sammendrag

Overvåkning og håndtering av is er et viktig tema på grunn av de farene is-objekter kan utrette mot fartøy og marine strukturer. Når aktiviteten i is-affekterte områder øker, observeres det en tilsvarende økning i motivasjonen for å utvikle gode metoder for å detektere og å overvåke is. Et viktig verktøy i denne sammenheng er satellitter. Satellitter kan produsere bilder med varierte oppløsninger, og som dekker store områder.

En algoritme, implementert i MATLAB, for automatisk overvåkning av objekter i satellittbilder er foreslått. Algoritmen har tre stadier den går gjennom for hvert bilde: deteksjon av objekter, sammenligning av objekter i bildet med objekter fra tidligere bilder, og klassifisering av objekter. Sammenligningen er gjort ved å bruke en geometrisk representasjon funnet for hvert av objektene. Algoritmens ytelse ble vurdert ved å bruke den på et sett av RADARSAT-2 bilder som dekker Grønlands østkyst. Resultatene viste at deteksjonen er effektiv for objekter som ikke er fullstendig omringet av is. Det er imidlertid ikke mulig å automatisk følge veldig små objekter som kun dekker noen få piksler. Denne oppdagelsen viste seg å skape problemer når vi skulle identifisere objekter som fartøy ved hjelp av klassifiseringsfunksjonen.

For å videre undersøke hvordan man kan skille mellom objekttyper i satellittbilder ble det gjort en analyse av lysstyrken som ble returnert fra ulike objekter i multi-polariserte bilder. Det ble observert at den returnerte lysstyrken fra fartøy- og is-objekter er av vesentlig forskjell. Ved å bruke en multi-polarisert areal rate, ble det vist at dette kunne bli brukt for å diskriminere mellom fartøy- og is-objekter. En videre indikasjon på objekttyper ble funnet ved å sammenligne bevegelsesmønstre for fritt flytende is-objekter med menneske kontrollerte fartøy.

For å kunne forutsi bevegelsen til is, en dynamisk modell for drift av isfjell er presentert. Ved å bruke et Kalman filter er det mulig å estimere hastigheten til et isfjell. Kalman filteret bruker målinger fra værdata og av isfjellets posisjon. Posisjonsmålingene som skal brukes i filteret kan man finne ved å bruke overvåkningsalgoritmen på satellittbildene. I denne masteroppgaven ble modellen kun simulert ved

hjelp av syntetisk data, og ikke ved å bruke satellittbilder.

# Acknowledgment

I would like to thank my supervisor Roger Skjetne for his contributions to this master thesis. Roger has guided me on deciding the scope of the thesis, and has given good advice on how to structure the text. I would also like to thank Qin Zhang for the help given when I struggled with the use of image processing methods. Further on, I want to mention my office mates Bjørnar Brende Smestad for providing me with tools for processing AIS data, and Sigurd Holsen for always helping me when I am in need.

Lastly, I want to thank Elise Bokneberg Mæland and Anne Marthine Rustad for patiently reading through my thesis, and giving me advice on grammar and structure.

# Abbreviations and Definitions

## Abbreviations

**AIS** - Automatic Identification System

**ASAR** - Advanced Synthetic Aperture Radar

**ESA** - European Space Agency

**EGC** - The East Greenland Current

**FLAR** - Forward-Looking Airborne Radar

**GPR** - Ground Penetrating Radar

**GPS** - Global Positioning System

**GVF** - Gradient Vector Flow

**IC** - Ice Concentration

**KF** - Kalman filter

**KSAT** - Kongsberg Satellite Services

**LOS** - Line-Of-Sight

**MMSI** - Maritime Mobile Service Identity

**NEST** - Next ESA SAR Toolbox

**RADAR** - Radio Detection And Ranging

**RAR** - Real Aperture Radar

**S-AIS** - Space-based Automatic Identification System

**SAR** - Synthetic Aperture Radar

**SLAR** - Side-Looking Airborne Radar

**UV** - Ultraviolet

**VHF** - Very High Frequency

**VTS** - Vessel Traffic Services

# Definitions

### Aperture

An opening which light travels through.

### Bimodal distribution

A distribution where the values have two different modes that appear as distinct peaks (local maxima) in the distribution graph.

### Centroid

The centroid, also known as the geometric center, of a two-dimensional region is the mean position of all the points in the shape. This can also be extended to n dimensions.

### Dead reckoning (navigation)

Dead reckoning is a prediction calculation used to find the position of a vessel at a given time. This is done by using a previously determined position, and thus advancing that position based upon known or estimated speed over a given time period.

### Dihedral and trihedral surface scattering

Dihedral is the angle between two planes, while trihedral is the intersection of three planes. In reflection (or surface scattering) a dihedral reflection is caused by two surfaces that are on orthogonal planes. In trihedral reflection, there are three surfaces.

### The Doppler effect

The Doppler effect is the change in frequency of a wave for an observer that is moving relative to its source. Compared to the emitted frequency, the received frequency is higher during the approach, identical at the instant of passing by, and lower during the recession.

**Geolocation**

The process of identifying the geographical location of a target by means of digital information processed via the Internet.

**Hyperspectral imagery (optical)**

The same concept as multispectral imagery (see definition), but the bands are much narrower (10-20 nm). Thus, a hyperspectral image could have hundreds of thousands of bands.

**Interpolation**

Given some known data points, interpolation is a method of constructing or inserting new data points within a range of the known data.

**Isotropic scattering**

Isotropic means identical in all directions. Thus, isotropic scattering means that something (light, power etc.) is divided in equal intensity and amount in all directions, and this forms a uniformity in all orientations.

**Multispectral imagery (optical)**

A multispectral image can capture image data at a large range of frequencies. These frequencies include visible light, but also infrared light and other frequencies beyond the visible light range. In multispectral imagery, the spectrum is divided into many bands. Usually 3 to 10 bands, that are represented in pixels.

**The Prewitt and Sobel operators**

The Prewitt and Sobel operators are both discrete differentiation operators, used for computing an approximation of the gradient intensity function in an image. It is used in image processing, particularly within edge detection algorithms, and creates an image which emphasizes edges and transitions. The difference between the operators is that they use different masks to compute a gradient.

**Remote sensing**

Remote sensing is the collecting of information about an object or phenomenon without making physical contact. The term generally refers to the use of aerial sensor technologies to detect objects on Earth.

**SAR signature**

A SAR signature is the backscatter associated with a particular surface type at a given band, polarization, and incidence angle.

**Swath width**

Swath width refers to the strip of the Earth's surface from which geographic data are collected by a moving vehicle such as a satellite, aircraft or ship in the course of swath mapping.

**Timestamp**

A timestamp identifies when a certain event occurred. An example is the Unix Timestamp, where the time of the given event is recorded as the total number of seconds passed since the 1th of January, 1970. This number is then used to derive the date and time of the event.

**Variance**

Variance measures how far a set of numbers is spread out. For instance, a variance of zero indicates that all the values are identical.

# Contents

# List of Figures

# List of Tables

# Chapter 1

# Introduction

## 1.1 Motivation

Since the 1970s the extent of sea ice on the globe has been measured from satellites. From these measurements it is shown that the sea ice extent today is significantly smaller than 40 years ago (Kwok and Rothrock, 2009). This, in combination with a higher need for energy and the huge amount of undiscovered resources in areas like the Arctic, have resulted in an increased activity in ice affected areas. Other reasons for the increased activity include the expansion of Arctic tourism, and an increase in commercial shipping in the north-west and north-east passages. For all marine operations in these areas, icebergs and sea-ice can pose a serious threat. Therefore, it is important to investigate methods for detection and tracking of ice, so that these threats can be managed. In addition, the identification of ice extent and movement is an important tool in the study of climate variability (Spreen et al., 2006). By observing the movement of sea ice and icebergs in polar areas, information about the ocean surface currents can be derived.

Today, satellite observations play an important role in ice identification services. Using satellites to obtain imagery is both cost effective and efficient compared with doing extensive field campaigns. Satellites can cover large areas fast and can produce imagery with a range of resolutions. By using satellites it is possible to retrieve information about the location and movement of ice. The information can also be used for classification of different types of ice.

## 1.2 Thesis Statement and Contributions

The overall aim of this thesis is to present methods for detection and tracking of ice in satellite images. For this purpose, the following contributions are presented:

- An algorithm capable of tracking targets in sequential images. The algorithm includes image processing methods for detection of targets, especially suited for satellite imagery, and a methodology for tracking these targets. In addition, it includes a simple classification feature for distinguishing between vessel and ice targets. The development and design choices of the algorithm is presented in Chapter 3 and in Chapter 4.
- An investigation on how to use multi-polarized satellite imagery and motion patterns of targets for aid in target discrimination. The investigation is carried out in Chapter 6.
- A dynamic model for forecasting of iceberg drift, and a filter for estimation of the iceberg velocity. The implementation and simulations of the model is found in Chapter 7.

## 1.3 Organization of the Thesis

**Chapter 2** presents the literature review, which provides all the background and the relevant references for the thesis. It includes an extensive background for remote sensing and image processing in relation to target tracking. In addition, methods for discrimination of targets and for motion forecasting are investigated. The sections in the literature review include all previous work related to the scope of this thesis.

**Chapter 3** presents the development of the detection and tracking algorithm. This includes a presentation of image processing methods used for detection, and the explanation of the tracking methodology. A synthetic test case is included to verify the logic of the algorithm.

**Chapter 4** presents a simple classification feature added to the detection and tracking algorithm. The purpose of this feature is to classify targets as ice or vessel. A synthetic test case is included to verify the logic of the feature.

**Chapter 5** presents a case study which illustrates the testing of the algorithm in a real case scenario. The imagery of the Greenland East Coast is acquired by RADARSAT-2 ScanSAR and Standard Quadpol sensors, and is from August 2013. In this chapter, two pieces of ice are tracked in a sequence of images to

show the algorithms ability to track certain objects of interest. Then, a test for classification of different vessel targets is performed, showing how the algorithm can identify targets as vessels.

**Chapter 6** presents an investigation on how to better discriminate between different target types. Here, images from the case study are used to see how multi-polarized imagery and motion patterns can be used to distinguish between ice and vessel targets.

**Chapter 7** presents a dynamic model for forecasting of iceberg drift, and a filter for estimation of the iceberg velocity.

**Chapter 8** presents the conclusion of the thesis. This includes a summary on the detection, tracking and classification abilities of the algorithm, on the results from the investigation on target discrimination and on the forecasting of ice drift with the dynamic model. The conclusion also includes recommendations for further work.

**Appendix A** presents information on satellites, including a list of operational and not operational satellites. It also presents the specifications of the satellite RADARSAT-2.

**Appendix B** presents an overview of vessels identified from the Automatic Identification System (AIS).

**Appendix C** presents the geographical data and timestamps for satellite images and detected vessels.

**Appendix D** presents the contents in the source code and explains how to run the algorithm and the dynamic model.

# Chapter 2

# Background

This chapter presents the literature review for this thesis. It includes background for remote sensing and image processing in relation to target tracking. In addition, methods for discrimination of targets and for motion forecasting are investigated.

## 2.1 Remote Sensing of Sea Ice and Icebergs

Remote sensing is a process which enables us to gain information from locations all over the world. Various sensors are mounted on air- and space-borne platforms, with the purpose of collecting various types of data. Satellite imagery is one of those types of data, and it allows us to view vast areas of the Earth's surface. Across the Arctic and other ice-affected areas, national ice services rely routinely on satellite imagery to generate ice information in near real-time. The primary source is satellite radars, synthetic aperture radar (SAR) imagery in particular, but data from optical satellites are used to aid interpretation.

This section of the literature review presents the principles of various sensor types used for remote sensing. It considers the properties for both airborne and marine sensors, and the sensor technologies are put in context with monitoring of sea ice and icebergs.

### 2.1.1 Passive and Active Sensors

The sensors used to obtain satellite imagery usually transmits microwaves. These waves are neither daylight dependent, nor affected by clouds. They are especially

appropriate for polar areas, due to longer periods of darkness and cloudy weather. The microwave sensors can be divided into two categories; active passive sensors.

An active sensor is a radar instrument used to measure signals transmitted from the sensor and then reflected or scattered by the Earth's surface.

A passive sensor is a microwave instrument designed to receive and measure natural emissions produced by components of the Earth's surface and atmosphere. It is often referred to as an optical sensor. Optical data are easy to use for visual interpretation, as the images represent the surface of the Earth the same way as the human eye views Earth. This type of imagery has been available since the 1970s, and well-established processing algorithms are available for automated feature extraction and classification. However, since a passive sensor receives natural emissions, the resulting imagery will be distorted by possible clouds or darkness. Therefore, in most polar areas an active sensor would be more suitable.

### 2.1.2 Basic Principles of Radars

In simplification, radars emit pulses of waves from an antenna. These waves will then bounce of objects in their path, and the radar signals are scattered in different directions, depending on the object's surface (Figure 2.1). Some waves will be directly reflected back to the transmitter (the antenna), and these signals are called backscatter.

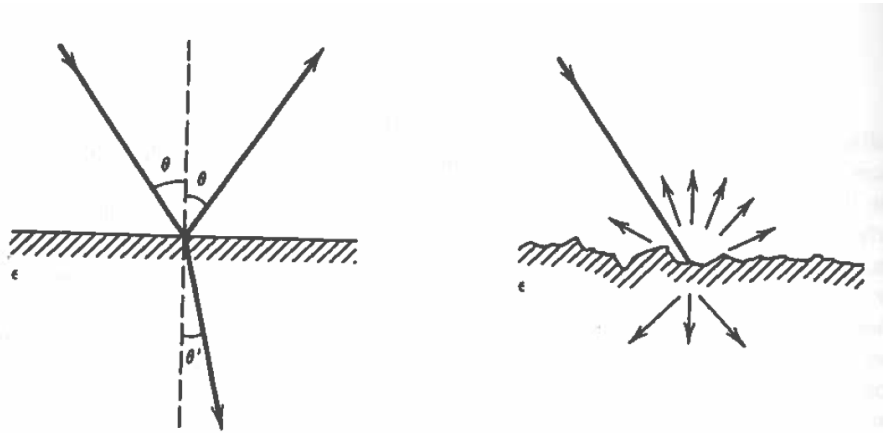

Figure 2.1: Surface scattering on a smooth surface (left) and a rough surface (right) (Elachi and Van Zyl, 2006).

To quantify the power scattered back in the direction of the sensor from a target

located at range R, one first makes the simplification of defining a radar cross sectional area, $\sigma$, as follows:

$$\sigma = \frac{I_{received}}{I_{incident}} 4\pi R^2 \quad [m^2] \tag{2.1.1}$$

where $\sigma$ is a target area that one would get from the measured intensity, $I_{received}$. It comes by assuming the target area, $\sigma$, intercepted the power transmitted ($I_{incident}$) and then scattered that power isotropically (Woodhouse, 2005).

Radars are used as detection and tracking tools, because they are able to recognize the objects in an area, their geometry and their movement. When an object moves, either towards or away from the transmitter, there is a slight change in the frequency of the waves. This is caused by the Doppler effect.

Most current radars operate in C-Band (wavelength 5 cm) or X-Band (wavelength 3 cm), although L-band (15 to 30 cm) and P-Band (30 to 100 cm) systems have been used on airborne and satellite platforms (Puestow et al., 2013). Seasonal changes can require different wavelengths. A longer wavelength (L-Band) would be better in summer and for mapping deformation features, while a shorter wavelength (X- and Ku-Bands) would be better in winter (Dierking and Busche, 2006). The C-Band represents a compromise between these, and is therefore widely used for all season capability. When data from various different sensors become more affordable and more widely available, the use of a combination of different bands will probably become more common place. For an overview of all the bands, see Table 2.1.

Table 2.1: Radar bands

| Band | Wavelength (mm) | Frequency (GHz) |
|---|---|---|
| L | 150-300 | 1-2 |
| S | 80-150 | 2-4 |
| C | 40-80 | 4-8 |
| X | 25-40 | 8-12 |
| Ku | 16-25 | 12-18 |
| K | 11-16 | 18-27 |

The spatial resolution of the imagery is affected by the length of the antenna, where the resolution improves as the length of the antenna increases (Van Zyl and Kim, 2011). The resulting image is influenced by data processing, and sometimes trade offs have to be made between noise reduction and resolution loss.

### Scatter Dependencies

There are various parameters determining how the imaging will turn out. Geometrical features like size, shape, orientation toward the sensor, and roughness are all important. In addition, dielectrics can play a role in how the emitted waves behave. This include factors such as water content, aggregate state, salt content and mineralogy.

The radar backscatter from an iceberg is a combination of surface and volume scattering. Volume scattering refers to returns from within an object, caused by internal inhomogeneities. Volume scattering is the dominant part of backscatter from icebergs, which is due to the low absorption of the non-saline glacial ice (Lubin and Massom, 2006). The low absorption allows a considerable amount of the radar energy to penetrate the the iceberg volume.

Surface scattering refers to the return from the surface of an object. As is seen in Figure 2.1, the backscattering from a surface is strongly affected by the geometrical properties of the surface. Thus, ice with a rough surface sends back different signals, and in a higher quantity than ice with a smooth surface. This makes it possible to distinguish between different surfaces; water, ice, snow, etc.

The backscatter is also dependent on the frequency of the incident wave, and the angle of incidence (Elachi and Van Zyl, 2006). The incidence angle at any given point on the illuminated surface depends on the pointing of the instrument and the relative position of the sensor with respect to that point. For instance, at lower incidence angles, surface roughness can increase the radar cross chapter of the target by allowing more of the pulse to interact with the sides of ridges in the surface. The incidence angle varies from one side of an image to the other, with the effects of this becoming more noticeable the wider the swath of the image is.

Sensitivity to changes of incidence angle depends on the scattering medium. For example, the backscatter from water varies greatly with incidence angle (Walker et al., 2006). If the images then are wide swath, the intensity will not be evenly distributed across the image. The water will appear much brighter on one side of the image than on the other side of the image, thus causing trouble when classifying the image (Haarpaintner and Solbø, 2007; Dierking and Dall, 2007). This complicates the separation of ice from water because the contrast between the two is not constant from one time or place to the next (Williams et al., 1999; Walker et al., 2006).

If there is a snow cover on the ice, this can affect the radar backscatter. The properties of the snow are dependent on temperature, density and ice crystal size distribution among others (Langlois and Barber, 2007). Dry winter snow will allow

penetration to the ice beneath, and will therefore reflect backscatter from the ice properties rather than the snow (Marko et al., 2003). Damp snow on the other hand, has low penetration at most frequencies, which means that it gives a low surface reflection and can act as a wave absorber.

Radars can also be sensitive to inhomogeneities in the ice volume, such as cracks and air bubbles (Dierking and Dall, 2007).

### 2.1.3 Airborne Sensors

There exists many different types of airborne sensors. These sensors are mounted on either aircrafts or satellites, which travel in trajectories over the regions that are going to be observed. This thesis will mainly focus on the imagery from synthetic aperture radars (SAR), which is a type of radar mounted on satellites.

#### Synthetic Aperture Radar

The synthetic aperture radar (SAR) is emerging as the predominant means of ice surveillance over large areas. It is widely used by national ice centers around the world.

SAR uses the forward motion of the sensor platform, while taking the Doppler shift of the collected signal into account to synthetically increase antenna aperture (Gade et al., 1996). Due to the fact that SAR uses an active sensor, it is typically inferred that brighter regions in the image represent a higher degree of surface roughness (such as ridges or hummocks) because of increased radar scatter. Melt ponds, thin ice and open water show up as darker features in the image because the radar signal undergoes spectacular reflection and less energy returns to the sensor over these areas (Blunt et al., 2012).

The achievable azimuth resolution of a SAR is approximately equal to one-half the length of the actual (real) antenna and does not depend on platform altitude. In addition, the SAR-sensors are largely weather-independent, and can acquire images both day and night. However, during high wind speed the contrast between open water and ice is reduced.

The characteristics of an acquired SAR image are influenced by characteristics of the SAR system used. Some of these features are determined by the specifications of the system while others can be influenced by the acquisition parameters. The parameters comprise repeat frequency, pulse repetition frequency, bandwidth, polarization, incidence angle, imaging mode and orbit direction. For a satellite

antenna, the polarization refers to the orientation of the waves transmitted or received by the antenna.

Radars can be configured to transmit and receive horizontally or vertically polarized radiation. By emitting a mixture of polarizations and using receiving antennas with a specific polarization, several images can be collected from the same series of pulses. Denoting the transmit and receive polarizations by a pair of symbols, a radar system using H and V linear polarization can thus have the following channels:

- HH - for horizontal transmit and horizontal receive
- VV - for vertical transmit and vertical receive
- HV - for horizontal transmit and vertical receive and
- VH - for vertical transmit and horizontal receive.

The radar system can have different levels of polarization complexity:

- single polarized - one of the mentioned channels
- dual polarized - a combination of two of the channels
- four polarizations - all the channels.

Different kinds of polarization, combined with different beam modes such as Ultra-Fine, Fine, Standard and Wide to mention some, give a wide range of resolutions and swath widths. A specification of the different beam modes of the satellite RADARSAT-2 can be found in Appendix A. This range creates a great number of unique SAR signatures. High resolution SAR information is important if an objective characterization of a particular ice floe is desired.

SAR-images usually contain some speckle noise. This noise is seen as bright spots in the SAR-images, which could be confused with ice. Thus, this noise has a severe impact on the use of SAR data for iceberg detection, because it can cause false detections. To improve iceberg detection in SAR images, it is necessary to filter out as much as possible of the high frequency speckle noise by using image processing. However, filtering out the noise may also result in filtering out some ice objects. A solution is to use SAR images with higher resolution initially, allowing speckle filtering to be done without loosing to much iceberg information. The choice of SAR mode is therefore important.

SAR data is a good alternative to optical satellite data. Some background information and analysis experience is necessary for SAR data interpretation, but with

the right processing and interpretation the data can deliver valuable and unique information that is not detectable through visual interpretation alone.

#### Other Airborne Radars

In addition to SAR, other types of radars can be used for ice observation. SAR is actually a of type side-looking airborne radar (SLAR), which is an imaging radar pointing perpendicular to the direction of flight. However, instead of being fitted with a SAR antenna, the SLAR can be fitted with a real aperture antenna. This is called a real aperture radar (RAR). In contrary to SAR, the achievable resolution of the RAR is dependent on altitude and incidence angle. For a given altitude the ground-range resolution improves for larger incidence angles, while the azimuth resolution improves for smaller incidence angles. Therefore, RAR are limited to short range and low altitude missions. RAR do have a proven iceberg detection capability. However, discrimination between ships and icebergs, and size estimation are unreliable (Shaw et al., 1988).

In addition to side-looking airborne radars, there are forward-looking airborne radars (FLAR). These are, reported to be less reliable than SLAR for small target detection (Ezman et al., 1991), but offers some level of target classification.

The ground-penetrating radar (GPR) has been used to characterize ice and snow structures in the Arctic. It uses radar pulses to image the subsurface, and can be used to determine ice thickness. However, it is not suitable for ice target detection.

A new type of SAR, developed by the European Space Agency (ESA), is the Advanced Synthetic Aperture Radar (ASAR). Compared to SAR, it features enhanced capability in terms of coverage, range of incident angles, polarization, and modes of operation (ESA, 2015). One of the differences is that it offers five polarization modes (VV, HH, VV/HH, HV/HH, and VH/HH). These capabilities makes the ASAR a good tool for ice detection and target discrimination (Howell et al., 2004, 2006).

### 2.1.4 Marine Radars

Ship-borne and land-based radars operate at more shallow angles compared to air-borne radars. Consequently, there is less backscatter, making discrimination between individual objects in the scene more challenging. To compensate for this, some marine radars integrate successive radar images to produce stable images of potential targets. The integration is possible since marine radars are able to dwell

on an area of interest for many revolutions of the antenna, and thus improve the ability to discriminate between different objects in the scene. For typical marine radars (20 – 30 RPM), a four to six minutes dwell time would be needed to create a stable image (Puestow et al., 2013). Also, the range of a ship-borne radar is limited from eight to 30 km, which is largely due to the height of the antenna (Puestow et al., 2013).

The vessel traffic service (VTS) is an example of a coastal radar network, which has many stations all over the world. Some of them are within the Arctic circle. Ship-borne radars have been used extensively for years as an aid to navigation, and is very common on ships of a certain size.

Ship-borne marine radars are often used to supplement aerial and satellite sensors (Egset and Nost, 2007). However, radars are usually developed for detection of targets. Echoes due to ice and waves are often filtered out, which makes these radars unsuitable for ice detection. Marine radars that are optimized for ice detection must therefore be used. One example of such a radar, is presented by O'Connell (2006) in the "Ice Hazard Radar" project. This radar includes technologies such as a high-speed scanner to improve the detection of small targets, a cross-polarized system which will be able to discriminate between different types of ice, and it uses digital signal filtering techniques to enhance and detect weak targets. Another example is the RADAR-Technology Ice radar, which in addition to having good detection capabilities, is winterized to perform at extremely cold temperatures.

### 2.1.5 Issues with Satellite Imagery

There are some factors that need to be considered when extracting ice condition data from images. One issue, is that satellite images are not obtained continuously. The images are obtained intermittently, with a different frequency of acquisition for each satellite. This means that there will be periods of time where real-time images are not available. Since satellites are in orbit, the span between images in a region will always be at least several hours. It could also be days between each image. Thus, prediction and estimation of the ice parameters are needed.

Another problem is that for satellite obtained images, there is a trade-off between coverage and resolution. Images with large coverage will have coarse resolution, and if a higher resolution is wanted, this would affect the available swath width. Lower resolution, makes the images more ambiguous, and it is harder to get accurate information when using image processing.

Another disadvantage in only using image-based data, is that there are no data in the vertical dimension. For this, some additional knowledge would be necessary.

### 2.1.6 Combination of Radars and Optical Sensors

As mentioned earlier, optical sensors are passive imaging devices, and they are sensitive in the Ultraviolet (UV), visible, and near-infrared spectral region (Puestow et al., 2013). Optical sensors include hyperspectral sensors, multispectral imaging systems, still, and video cameras. This kind of imagery can either be air-borne on satellites, drones, or other aerial vehicles, or it can be cameras or sensors placed on a ship or on shore.

Combining radar imagery (both air-borne and marine radars) with optical imagery can help solving the continuity problem mentioned in Section 2.1.5. By using optical imagery in addition to marine radars when satellite images are unavailable, it is possible to achieve better continuity in the image stream. Optical imagery can also help in getting a closer view in selected areas, enabling the detection of ice floes and icebergs of a smaller size than possible by simply using SAR-imagery. Studies have shown that combined use of optical and SAR images for iceberg detection does indeed give better results compared to previous studies where SAR and optical images were used separately (Sandven et al., 2007). This study shows that an optimal solution for iceberg detection is to use a synergy of optical and SAR images, both with a resolution of 10 m or better.

However, optical imagery can not see through clouds or fog, which is a great disadvantage, especially in Arctic areas. A daily acquisition scheme should be used to ensure that data are captured under favorable conditions, which means no-cloud for optical images and low-wind for SAR images.

Satellites can observe the largest icebergs in the Barents Sea, typically 100 m or more in horizontal extent, and under specific wind and sea ice conditions (Sandven et al., 2007). Iceberg observations in high-resolution optical images are not hampered by the speckle noise that is characteristic for the SAR images. Observations in optical images are therefore more reliable for icebergs of size of 100 m or less.

When combining different sensor technologies, image co-registering is required to ensure that images from different sensors over the same region align. Georeferencing ties the imagery to the geographic reference system used and is usually achieved by GPS measurements.

Both optical and radar sensors are sensitive regarding different surface characteristics. Thus, an integrated use of satellite data from both sensors can greatly

improve the ability to detect, identify and discriminate among different objects.

In addition, when frequent updates are needed, having images from more than one sensor is useful. Depending on weather conditions and monitoring demands, different sensors can substitute for others, depending on access and cloud-cover constraints.

### 2.1.7 Commercial Use of Radar Data

There are a number of different satellite systems which acquire SAR-data systematically. For instance, the European Space Agency's (ESA) SENTINEL-1, which carries a single C-band SAR and among other applications is made for monitoring sea ice zones, the Arctic environment, and for surveillance of marine environment. Another example is the RADARSAT-2, which has a SAR with multiple polarization modes and was launched by the Canadian Space Agency. Both of these satellites deliver data to users in near real-time. The Kongsberg Satellite Services (KSAT) is a norwegian operator of satellite group stations. They manage several satellites, including RISAT-1, which is commercially available, and carries a C-band radar sensor with a variety of resolutions and polarization modes. An extensive list of existing satellite systems is available in Appendix A.

## 2.2 Image Processing Methods for Detection of Objects

There exist several techniques and methods for segmenting images, as will be discussed in this chapter. Segmentation subdivides an image into different regions with different properties. This is a powerful tool in ice management, because it enables us to divide ice and water into two separate partitions. A separation like this can be very valuable when deciding the properties of sea ice. However, segmentation of images is not always trivial. Therefore, to perform a proper partition, a combination of methods are often necessary.

This section presents a set of image processing methods for detection of objects, and discuss the identification of targets in ice affected waters.

### 2.2.1 Thresholding

Image segmentation algorithms are generally based on one of two basic properties of intensity values: similarity and discontinuity (Gonzalez and Woods, 2002). In the first category, the approach is to partition an image into regions that are similar according to a set of predefined criteria. Thresholding is an example of a method from this category.

The gray-level histogram is a representation of an image's distribution of gray tones. In an image with light objects on a dark background, like ice floes in water, the gray levels are grouped into two dominant modes. For an image like this, using thresholding is a natural way to segment the picture into an "object-region" and a "background-region". A threshold value $T$, which separates these regions, should be chosen. By using this technique, it is possible to turn a gray-scale image into a binary image. This is done by making the image into a matrix, where each element represent a pixel with a gray-scale value. Then, a transformation is performed, where the values that are higher than the threshold $T$ are replaced by a ones, and the values that are lower than the threshold $T$ are replaced by zeros. The result is a binary image, where the zeros represent water (in black color), and the ones represent ice (in white color).

Multilevel thresholding is also possible. An example is when a point $(x, y)$, with the gray level $f(x, y)$, belongs to one object class if $T_1 < f(x, y) \leq T_2$, to another object class if $f(x, y) > T_2$, and to the background if $f(x, y) \leq T_1$. Here two threshold values, $T_1$ and $T_2$, are needed to make three different regions.

Sometimes, the illumination of the image is uneven. In those cases, it can be

advantageous to use local threshold instead of a global threshold for the whole image (Gonzalez and Woods, 2002). This is usually done by dividing the original image into sub-images, and then different threshold values are utilized to segment each sub-image.

### The Otsu Thresholding Method

To obtain an accurate result while using thresholding, it is important to chose the most suitable threshold value. In an ideal case, the histogram has a deep and sharp valley between two peaks representing objects and background, respectively, so that the threshold can be chosen at the bottom of this valley (Prewitt and Mendelsohn, 1966). However, this is not always the case. The Otsu thresholding method (Otsu, 1975) is a method where a threshold is automatically selected from the histogram. The threshold is selected by maximizing the separability of the resultant classes in gray levels. Thus, the selected value is based on integration of the histogram, and not the differentiation (i.e., local properties such as valleys).

In the Otsu thresholding method, two assumptions are made (Zhang, 2012);

- The histogram of the image is bimodal.
- The illumination of the image is uniform.

Having a bimodal histogram, means that the distribution of gray levels have two different modes that appear as distinct peaks (local maxima) in the distribution graph.

The goal is to find the threshold value $T$ that minimizes the within-class variance, given by:

$$\sigma_\phi{}^2(T) = \omega_1(T)\sigma_1^2(T) + \omega_2(T)\sigma_2^2(T), \tag{2.2.1}$$

where $\omega_1$ and $\omega_2$ are the probabilities of the two classes separated by the threshold $T$, and $\sigma_1^2$ and $\sigma_2^2$ are the variances of these two classes (Otsu, 1975).

The threshold with the maximum between-class variance also has the minimum within-class variance. The between-class variance is given by:

$$\sigma_b^2 = \omega_1(T)[\mu_1(T) - \mu(T)]^2 + \omega_2(T)[\mu_2(T) - \mu(T)]^2 \tag{2.2.2}$$

$$\cong \omega_1(T)\omega_2(T)[\mu_1(T) - \mu_2(T)]^2 \tag{2.2.3}$$

where $\mu_1$ and $\mu_2$ are the means of the two classes, and $\mu(T) = \omega_1(T)\mu_1(T) + \omega_2(T)\mu_2(T)$. This expression can be used to find the best threshold and to update the threshold value iteratively.

An example of thresholding using the Otsu method is in Figure 2.2.

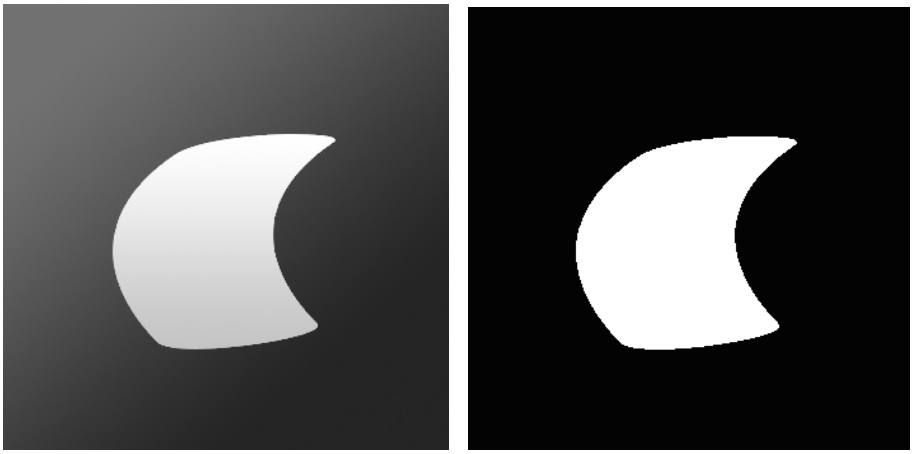

(a) A simple gray-scale image of a bright object on a dark background.

(b) The segmented image using the Otsu threshold method.

Figure 2.2: A segmentation example using thresholding.

### 2.2.2 Clustering

Clustering is as thresholding a way to use the similarities in intensity values to segment images. A cluster is a collection of data objects, where the data within the same cluster is similar to another, and dissimilar to the data in other clusters (Madigan, 2012). By using this technique, it is possible to can identify different types of ice by dividing the image into two or more clusters, e.g., ice floe, brash ice, etc.

Several clustering algorithms exist (Anderberg, 1973), such as

- **Hierarchical**: Find successive clusters by using previously established clusters.
- **Partitional**: Determine all clusters at once.
- **Subspace**: Look for clusters that can only be seen in a particular projection of the data.

To achieve high quality clustering, the similarities must be measured. The similarity is expressed in terms of a distance function, which is typically metric. This distance measurement will affect the shape of the clusters.

### K-means Method

K-means clustering is a widely used clustering method. The algorithm is composed of the following steps (MacQueen et al., 1967):

1. Place K points into the space represented by the objects that are being clustered. These points represent initial group centroids. In image processing, these groups are sets of gray-levels.
2. Assign each object to the group that has the closest centroid.
3. When all objects have been assigned, recalculate the positions of the K centroids.
4. Repeat Steps 2 and 3 until the centroids no longer move. This produces a separation of the objects into groups from which the metric to be minimized can be calculated.

Finally, this algorithm aims at minimizing an objective function, in this case a squared error function:

$$J = \sum_{j=1}^{k} \sum_{i=1}^{n} ||x_i^j - c_j||^2, \tag{2.2.4}$$

where $||x_i^j - c_j||^2$ is a chosen distance measure between a data point $x_i^j$ and the cluster center $c_j$.

In an image processing setting, these steps will equal

1. For a set of gray-levels: $f(x_1, y_1), f(x_2, y_2), ..., f(x_n, y_n)$, partition this set into $k$ clusters:

$$f_i(x_1, y_1), f_i(x_2, y_2), ..., f_i(x_n, y_n) \text{ for } i = 1, 2, ..., k \tag{2.2.5}$$

2. Calculate the local means of each cluster

$$c_i = \frac{1}{n_i} \sum_{m=1}^{n_i} f_i(x_m, y_m) \text{ for } i = 1, 2, ..., k \tag{2.2.6}$$

3. Gray level $f(x_j, y_j)(j = 1, 2, ..., n)$ belongs to set $p$ if it has the shortest distance to set $p$ than any other sets:

$$|f(x_j, y_j) - c_p| \leq |f(x_j, y_j) - c_i| \text{ for } i = 1, 2, ..., k \tag{2.2.7}$$

4. Iterate steps 2 and 3 until the local means are unchanged.

An example of clustering using the k-means method is performed on the image in Figure 2.2a. The resulting segmented image (Figure 2.3) gives the same segmentation as when using the Otsu method.

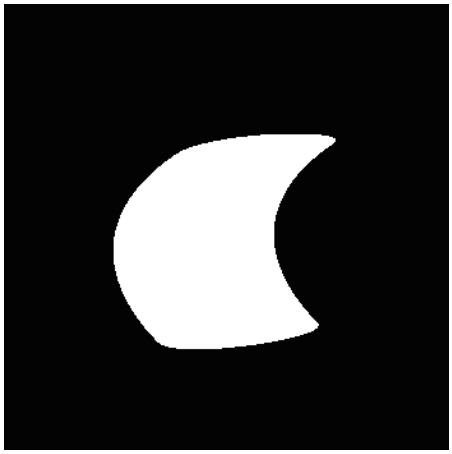

Figure 2.3: A segmented image using the k-means clustering method.

It is important to note that the algorithm is very sensitive to the initial randomly selected cluster centers. Also, the k-means method is not suitable for discovering clusters with non-convex shapes.

Both clustering and thresholding can effectively be used for segmenting images, and from the results the exact ice concentration (IC) in the segmented image can be calculated (Zhang, 2012). The deviation between the calculated IC and the actual IC is dependent on the choice of segmentation algorithm, and the quality and resolution of the image.

In addition to use the clustering method for separation between ice and water, the method can be used to gain information about the surface of the ice. Both in optical- and SAR-imagery, rougher ice tend to give a brighter return than smooth ice. Thus, by making clusters that separates the different intensity values of the surface in regions, it is possible to make a surface texture characterization. The windowed statistical analysis (WSA) have been proposed by Kumaran (2012) and

Blunt et al. (2012) as a means to distinguish variations in surface texture. The method consist of the following steps:

1. Window selection and local statistical distribution computation.

2. Distance computation between local distribution.

3. Clustering local distributions for segmentation.

### 2.2.3 Edge Detection

The second category of image segmentation algorithms is based on discontinuity. For these algorithms, the approach is to partition an image based on abrupt changes in intensity, such as edges in an image (Gonzalez and Woods, 2002).

Edges is a set of connected pixels that lie on the boundary between two regions. This gives a rapid change in image brightness between neighboring pixels, which enables us to identify objects in an image.

The edges are identified by finding the difference between regions, and this is measured by the image gradient vector.

$$\Delta f = \begin{bmatrix} G_x \\ G_y \end{bmatrix} = \begin{bmatrix} \frac{\partial f}{\partial x} \\ \\ \frac{\partial f}{\partial y} \end{bmatrix} \tag{2.2.8}$$

The gradient vector is directed towards the most rapid change in intensity. Certain criteria, based on this vector, enables us to identify which pixels in an image that may belong to an edge.

In Figure 2.4 edge detection has been performed on the example image (Figure 2.2a). To compute an approximation of the image gradient vector, the Sobel operator has been utilized.

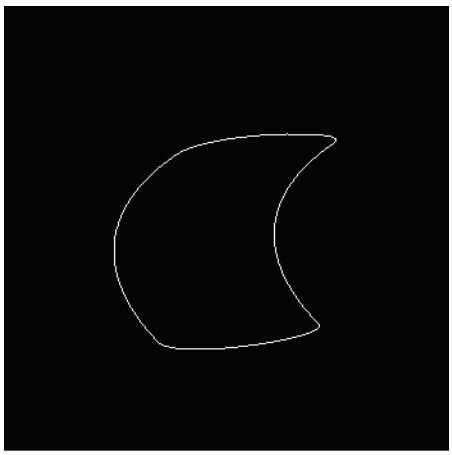

Figure 2.4: Edge detection using the Sobel operator to compute the image gradient vector.

Another operator often used to find the image gradient vector, is the Prewitt operator. These two operators, Prewitt and Sobel, are among the most used in practice for computing digital gradients. They are both discrete differentiation operators, used for computing an approximation of the gradient intensity function in an image. The Prewitt masks are simpler to implement than the Sobel masks, but the latter have slightly superior noise-suppression characteristics (Gonzalez and Woods, 2002).

Edge detection of ice floes can be used to extract some ice properties, such as area, perimeter, and shape measurements. This is valuable information when trying to manage ice.

A common method to detect edges is by estimating the gradient of the image at every point to generate a "gradient" image, and then thresholding the gradient image.

Ideally, the edge detection techniques should only yield pixels lying on edges. In practice, this set of pixels seldom characterizes an edge completely because of noise, breaks in the edge from nonuniform illumination, and other effects that can introduce intensity discontinuities (Gonzalez and Woods, 2002). Because of this, edge detection algorithms are typically followed by linking procedures to assemble edge pixels into meaningful edges. A way to do this, is by analyzing the pixels in a small neighborhood around each of the edge-pixels. All points that are similar according to a set of predefined criteria are linked, forming an edge of pixels that share those criteria. The criteria for similarity can for instance be based on the strength of the response of the gradient operator, or the direction of the gradient

vector (Gonzalez and Woods, 2002).

### 2.2.4 Identification of Sea-Ice Floes

The identification of sea-ice floes and icebergs are more difficult to find in ice-affected water with a high concentration of ice, compared to open water. It would be necessary to separate seemingly connected ice floes, which may be challenging, because the junctions can be difficult to identify.

To overcome this problem, some research have been done by Zhang et al. (2013) and Blunt et al. (2012) on the watershed transform. However, watershed segmentation has a tendency to over segment, and this will affect the ice floe detection results. This method will be further explained in Section 2.2.5.

Banfield and Raftery (1992) have suggested a method of estimating closed principal curves using the erosion-propagation algorithm, which combines erosion from mathematical morphology with local propagation of information about floe edges. The theory of erosion is presented more thorough in Section 2.2.6.

Another method that can be applied for separating connected floes, is the gradient vector flow (GVF) snake algorithm, developed by Xu and Prince (1998). Snakes, or active contours, are curves defined within an image domain that can move under the influence of internal forces coming from within the curve itself and external forces computed from the image data. The gradient vector flow (GVF) is an external force for active contours, and is computed as a diffusion of the gradient vectors of a gray-level or binary edge map derived from the image.

The classic snake algorithm is effective in solving "weak" boundary connections, but the algorithm is sensitive to the initial contour, which should be somewhat close to the true boundary. The GVF Snake is faster and less restricted by the initial contour (Zhang and Skjetne, 2013; Sheng et al., 2012).

### 2.2.5 The Watershed Transform

The watershed transform is a way of segmenting an image which embodies both of the segmentation concepts (similarity and discontinuity) that has been mentioned. It often produces more stable segmentation results, including continuous segmentation boundaries (Gonzalez and Woods, 2002). The concept was first introduced by Beucher and Lantuéjoul (1979), and was later implemented as a computationally efficient method by Vincent and Soille (1991).

To understand the watershed transform, the grayscale image must be envisioned as a topological surface, where the values of $f(x, y)$ are interpreted as heights. Thus, the height of the "mountains" and the depth of the "valleys" are proportional to gray-level values in the input image. The goal of the transform is to identify the watershed lines. These lines divide the topological surface into "valleys", also called catchment basins. When imagining drops of water falling on the topological surface, the water would all collect in these catchment basins. The watershed lines would act as ridges, and drops falling exactly on the ridges would be equally likely to collect in either of the basins separated by the watershed line.

The watershed lines is actually found by constructing a dam around each catchment basin. In the water drops scenario, if the basins start to fill up, and the water in two basins is about to merge, a dam is built to prevent the merging. These dam boundaries correspond to the divide lines of the watershed. To construct the dams, morphological dilation is used (see Section 2.2.6) by applying the same concept as when an actual basin is being filled up with water. Figure 2.5 shows an illustration of the watershed transform.

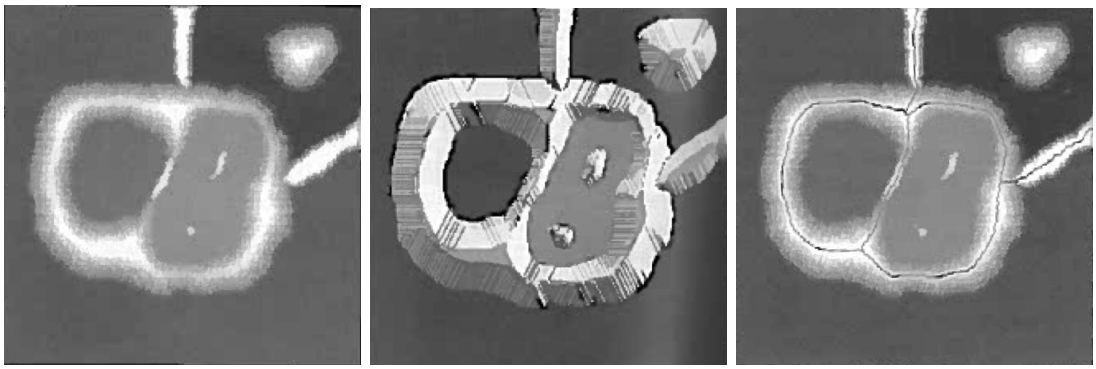

(a) Original image. (b) Topographic view of (a). (c) Final watershed segmentation lines.

Figure 2.5: An illustration of the watershed transform. Image courtesy of Beucher (1994).

An issue with the watershed transform is that it is prone to oversegmentation. This means that objects are not segmented properly, and are therefore split into several segments. To avoid this, the gradient magnitude is often used to preprocess the gray-scale image prior to using the watershed transform for segmentation. To do this, a morphological gradient must be computed, as described in Section 2.2.3. This is used to make the gradient magnitude image. Before using the watershed transform, the gradient image should be made smooth. A way of doing that, is

by using a close-opening technique, which will be described in Section 2.2.6. The image can now be used in the watershed transform.

Another approach used to avoid oversegmentation is a method called basin dynamics (Grimaud, 1992). The method is based on mathematical morphology operators, which eliminate local minima deeper than a defined threshold. This basically means that the the deepest catchment basins are made more shallow. The basin dynamics method was tested among a set of other watershed transform approaches by Silva (2006). When testing the techniques on SAR images, watershed with basin dynamics showed the best results, with the fewest number of incorrectly classified pixels.

### 2.2.6 Dilation and Erosion

Mathematical morphology is a collectively used term for operations which are used for extracting image components that are useful in the representation and description of region shape. Dilation and erosion are fundamental operations in morphology, and are used in many image processing algorithms.

Dilation is an operation that makes an object bigger by adding pixels along the outer boundary of the object in a binary image. It is a way of gradually "growing" or "thicken" the object. The extent or manner of the thickening is controlled by a shape referred to as a structuring element. This element can be in the shape of various elements; a diamond, a disk, an octagon, and a line, just to mention some.

If $A$ is the object that should be dilated, and $B$ is the structuring element, and both are sets in $\mathbb{Z}^2$, the dilation of $A$ by $B$, denoted $A \oplus B$, is defined as

$$A \oplus B = \{z|(\hat{B})_z \cap A \neq \emptyset\} \tag{2.2.9}$$

where $\emptyset$ is the empty set (Gonzalez and Woods, 2002).

Erosion is the opposite of dilation. By removing the pixels along the outer boundary of the object, the erosion "shrinks" or "thins" objects in a binary image. Also in erosion, the manner of the shrinking is controlled by the structuring element, $B$.

For sets $A$ and $B$ in $\mathbb{Z}^2$ the erosion of $A$ by $B$, denoted by $A \ominus B$, is defined as

$$A \ominus B = \{z|(B)_z \subseteq A\} \tag{2.2.10}$$

(Gonzalez and Woods, 2002). The equation indicates that the erosion of $A$ by $B$ is the set of all the points $z$ such that $B$, translated by $z$, is contained in $A$.

An example with iterations of erosion on a target is found in Figure 2.6.

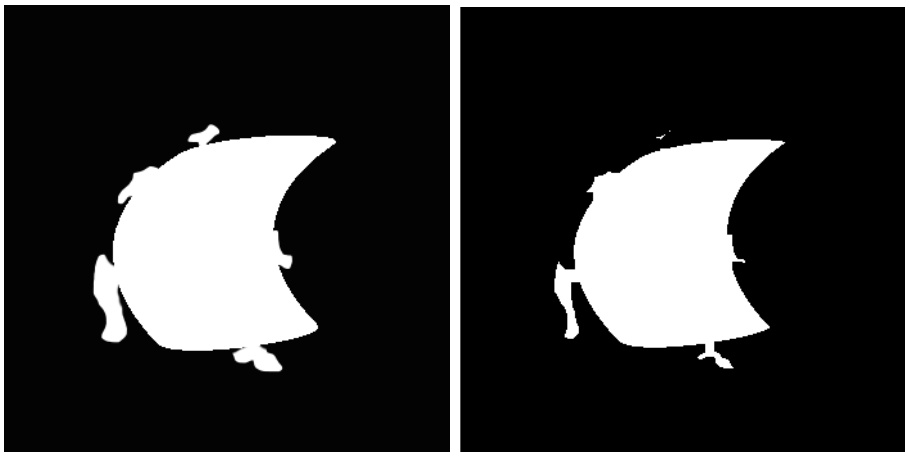

(a) The segmentation of image in Figure 2.2a with added protrusions.

(b) Erosion of (a) with 3 iterations.

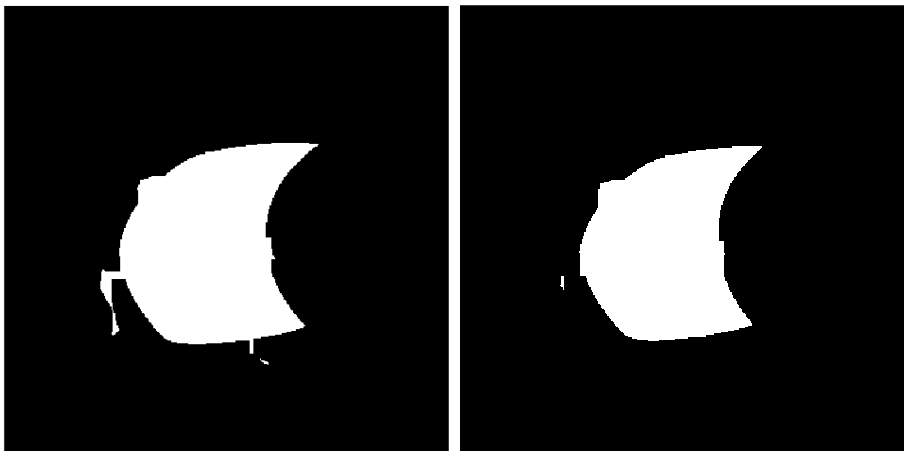

(c) Erosion of (a) with 5 iterations.

(d) Erosion of (a) with 8 iterations.

Figure 2.6: A target being eroded in 3, 5 and 8 iterations.

By combining dilation and erosion an image can undergo a series of dilations and/or erosions. Two of the most common combinations are called opening and closing. Opening generally smooths the contour of an object, removes regions of an object that cannot contain the structuring element, breaks thin connections, and removes thin protrusions.

The morphological opening of $A$ by $B$, denoted by $A \circ B$, is simply erosion of $A$

by $B$, followed by dilation of the result by $B$:

$$A \circ B = (A \ominus B) \oplus B \tag{2.2.11}$$

(Gonzalez and Woods, 2002).

Closing also smooths the contour of an object. However, in contrast to opening, closing joins narrow breaks, fills long thin gulfs, and fills holes smaller than the structuring element.

The morphological closing of $A$ by $B$, denoted by $A \bullet B$, is a dilation followed by an erosion:

$$A \bullet B = (A \oplus B) \ominus B \tag{2.2.12}$$

(Gonzalez and Woods, 2002).

Figure 2.7 shows an example of the opening and closing of a target, by using the same image as in Figure 2.6a.

(a) The opening of a target. (b) The closing of a target. (c) Both opening and closing of a target.

Figure 2.7: Morphological opening and closing of a target. For all figures a disk of radius 5 have been used as the structuring element.

### 2.2.7 Ocean Clutter

To detect icebergs with SAR imagery, the backscatter caused by icebergs must be distinguishable from the ocean clutter. Generally, clutter levels correlate well with

wind speed (Power et al., 2001). Also, both sea-state and radar incident angle are factors that might affect the intensity of the ocean clutter. Because of these factors the clutter will vary. It is therefore important to determine an appropriate threshold level when detecting targets in the images.

Higher wind speeds, generating greater sea clutter, may lead to icebergs being missed altogether in automatic detection (Howell et al., 2004; Lane et al., 2002; Power et al., 2001).

## 2.3 Tracking and Discrimination of Targets, and Motion Forecasting

By using the methods explained in Section 2.2, it is possible to develop algorithms for tracking targets. After the necessary image processing is finished, some parameters or features can be extracted which makes it possible to detect ice objects or track the ice motion in a sequence of images.

In this section, different methods and techniques for tracking ice are considered. In addition, methods for classification of the detected targets are discussed. Lastly, a dynamic drift model and a filter for estimation of the ice motion is presented.

### 2.3.1 Tracking of Ice-Objects

The use of automatic ice motion tracking techniques began in the late 1980s. The known techniques for tracking are usually in one of two categories.

The first one consist of methods for deriving sea ice movement vectors from cross correlation between pairs of images (Kwok and Rothrock, 1999; Haarpaintner, 2006). These cross correlation techniques are based on convolution; finding the same pattern of pixels in two images. These methods work best on packs of ice, where the floes moves together. Thus, they are not suitable for tracking in the summer months, because the the ice is more dispersed.

The other category consist of tracking methods which are feature or object based. In these methods, an object is detected in an image and then re-detected in consecutive images. The detection is achieved by segmentation of the image. Kwok et al. (1990) and Liu et al. (1997) describe a method for tracking which stores the coordinates of the object boundaries, and then generates a rotationally invariant representation to be used for matching.

A similar method is described in Silva and Bigg (2005), where they have made a semi-automated algorithm to track icebergs. The algorithm is called ITSARI (Ice Tracking from SAR images), and it makes a one-dimensional shape representation for each iceberg-object.

The algorithms was made for tabular Antarctic icebergs. However, Hall et al. (2012) have made an extension which can also be used on smaller ice objects in the northern hemisphere.

Something that is common for all object or feature based tracking methods, is that successful tracking relies on the object maintaining a distinctive shape throughout

its tracking life. In addition, the object must always be seen against a background of a different brightness value. Consequently, these kinds of techniques will work best in the summer months, due to ice objects having more distinctive shapes and also being better separated (Hall et al., 2012). In comparison, using these algorithms to track ice in the winter months will give a large number of false alarms.

Some detection algorithms uses a constant false alarm rate (CFAR) technique (Skolnik, 1990; Power et al., 2001) to determine the appropriate threshold level for image segmentation. Firstly, image regions of roughly consistent clutter are used to determine the clutter statistics. The mean and the variance of the clutter within each region are then used to derive the threshold value. This approach is especially useful in the presence of much ocean clutter.

The smallest iceberg that can be detected are of the order of a pixel in an image (Land, 2002), but objects this small cannot be tracked as they have no individual shape. It is generally more difficult to find a distinct shape when targets are small. Icebergs in the Arctic are typically smaller than those in the Antarctic, and therefore they are more difficult to detect and track. It is often the smaller icebergs that drift into shipping lanes. It is therefore crucial to continue developing this technology, to enable successful detection and tracking of smaller icebergs.

### 2.3.2 The Use of Different Polarizations and Bands to Identify Different Targets

Discrimination between icebergs and vessels in SAR imagery can be a difficult task with unreliable results. Misclassification can result in spending a significant amount of resources for investigation or avoidance. Target detection in SAR images can be made more reliable if several polarizations are acquired simultaneously at appropriate radar incidence angles. This can be useful for a classification procedure.

Finding patterns in the brightness return from targets in images with different polarizations and bands can be useful in target classification. These patterns can be used to develop classification features for discrimination between different types of targets.

Targets respond differently to varying polarizations (Alexandrov et al., 2004). Iceberg targets are known to have a combined surface and volume scattering mechanism while ships tend to have a combination of dihedral and trihedral surface scattering. This can be a cause for different targets having significantly different

responds in the HV and HH channels. In addition, the required rotation from horizontal to vertical in the cross channel (HV) response can also be a factor to consider.

In Howell et al. (2004, 2006) iceberg and ship targets in multi-polarization ASAR data have been analyzed. It was shown that the return from ship targets in the HH and HV channel were comparable. In contrast, iceberg targets had weak, or sometimes non-existing, HV responses compared to the HH channel. By using this fact, combined with two target discrimination methods; a multi-polarized area ratio and HV signal-to-clutter ratio (SCR), they were able to achieve target discrimination with 97 and 92 percent accuracy, respectively. However, the majority of the vessels in this research were large supply vessel, and the results could be different for smaller vessels.

Having dual-polarized SAR/ASAR data is advantageous compared to single polarization imagery. In single polarization, there is no possibility to compare the target properties in different channel. While quad-polarimetry SAR data have an obvious potential for marine target detection and discrimination of vessels and icebergs in Arctic regions, this data mode is only available for limited swath widths with todays technology. Therefore, when wanting to monitor large ocean areas operationally, SAR image products with lower resolution, dual polarization, and wider swaths are currently preferred.

It can be important to select appropriate incident angles to achieve successful detections. According to vessel detections done by Brekke and Anfinsen (2011) on dual-polarization SAR imagery, smaller incident angles have a higher peak-to-clutter ratio in the cross-polarized channel than in the co-polarized channel. In their research, a high ($> 10$ dB) peak-to-clutter ratio is an indication of a detected target. Thus, cross-polarization should be preferred for smaller incident angles, because more vessels will be detected. For larger incident angles, it was shown that both channels could be used for detection, as all targets had a peak-to-clutter ratio of more than 10 dB.

The wavelength does also affect how the backscatter from ice varies. For instance, C-Bands show a greater variation between young and old ice than L-Band does. This is due to its greater sensitivity to the surface roughness in relation to the wavelength (Dierking and Dall, 2007). At an even shorter wavelength, X-Band shows an even greater sensitivity to surface roughness. Consequently, the brightness of returns from an ice object will be very dependent on the roughness of that objects surface.

For C-Band, the HH polarization channel has been shown to produce better ice discrimination at low wind speed. The VV channel on the other hand, produces

better results in high wind speeds (Williams et al., 1999). As mentioned, C-Band has a higher sensitivity to surface roughness than the L-Band has. This results in C-Band backscatter differing more between co- and cross-polarization than L-Band backscatter. At L-Band, cross-polarization produces better discrimination between ice and water than co-polarization (Dierking and Dall, 2008).

### 2.3.3 Automatic Identification System

The Automatic Identification System (AIS) is a communication system which enables automatic exchange of information between vessels. All vessels of a certain size is required to use this system. It is based on low power, very high frequency (VHF) transponder broadcasts (English et al., 2013).

The information are sent as messages containing different pieces of information. Dynamic data are sent in different intervals according to the speed and status (USCG, 2015). The most crucial information, like position and corresponding accuracy indication, the vessel's Maritime Mobile Service Identity (MMSI), course and heading are broadcast at a high frequency. Usually every 2-10 seconds. Other types of information, like type of ship, dimensions of ship and destination are only broadcast every 6 minutes.

The prime purpose of AIS is collision avoidance. However, the broadcast information is very useful for surveillance and security purposes. By using the positional data and the timestamps for the vessels using the AIS, it is possible to identify these vessels in satellite acquired imagery. This is useful when trying to discriminate between ice and vessel targets.

The Norwegian Coastal Administration has a network of 44 base stations that retrieve AIS data from the Norwegian baseline and up to 60 nautical miles out at sea. Several years worth of AIS data is saved and made available to other official parties by request. In addition, in the sea areas outside Norway and Svalbard the satellites AISSat-1 and AISSat-2 are used to receive satellite based AIS information.

The AIS capability was developed for line-of-sight (LOS) applications. However, by having AIS receivers on satellites a more global coverage is possible. These types of systems are called Space-based automatic identification systems (S-AIS). The use of S-AIS vessel detections is expected to improve the accuracy of a SAR-based discrimination algorithm by reducing confusion between iceberg and ship targets (English et al., 2013).

There are some issues to consider when using S-AIS. When LOS and AIS are used in combination, the self organizing protocol of AIS ensures that signals from

different ships do not interfere with each other. However, when the sensors are satellite-mounted, a high density of ships in a region can cause collision of AIS messages (English et al., 2013). This can be troublesome, and cause loss of information. However, in regions that are frequented by icebergs, ship densities are relatively small. Thus, this limitation is not necessarily a limiting factor in the context of this project.

When combining S-AIS with SAR data, time synchronization is necessary. SAR and S-AIS data are derived from different satellites, therefore the SAR and S-AIS detections will differ in time. Sometimes the difference will be as much as several hours or more. Understandably, this creates issues when the vessels and icebergs move during the satellite acquisitions. These issues can be eliminated if the AIS receiver and SAR sensors are located on the same satellite. If they are not, a possibility is to use dead reckoning with navigational data from the AIS. Dead reckoning is a way of finding the position of a vessel at a given time, by using a previously determined position. This way, the position of the ship (or iceberg) can be predicted and compared with SAR target locations. An even simpler way is to use interpolation. However, there are uncertainties connected to these method, and they are influenced by factors like vessel activity, weather conditions, etc.

It is also important to note that AIS from satellite coverage are of an intermittent nature, and the tracks tend to be sparse. There can be a burst of messages lasting for a number of seconds, followed by a silence typically lasting from one to six hours.

### 2.3.4 Separation of Iceberg From Sea Ice

Icebergs and sea ice have different characteristics and properties, and it is therefore important to separate these two types of ice. When distinguishing between these, it is crucial to know that they do not produce the same radar returns, which is due to the different structure and salinity of the ice.

Pieces of sea ice have lower average backscattering than icebergs. This is due to a smoother surface on sea ice (Williams et al., 1999). This means that icebergs are expected to stand out from sea ice as brighter areas. If using a brightness threshold to segment the images, the threshold for sea ice must be lower than for an iceberg to accurately identify all targets. However, snow on the surrounding sea ice or water on the surface of the iceberg can lower the contrast between the two, which makes the separation more difficult (Gladstone and Bigg, 2002; Williams et al., 1999).

In addition, distinction between first year and multi-year ice is important when

choosing the threshold. These types of ice can have different radar returns, some strong and some weak. The physical properties of ice and snow vary enormously by type, age, season, time of day and region, posing difficulties for accurate characterization. Consequently, in some cases iceberg signatures may become confused with those from multi-year ice floes (Lane et al., 2002).

### 2.3.5 Models for Iceberg Drift

Several iceberg drift models, suited for various regions, exist today. Currently, one of these are successfully being used in operations on the east coast of Canada (Kubat et al., 2005). However, the models are not always proven to be accurate, because of an insufficient validation of the underlying model.

A simplified case of the iceberg's drift says that it is relative to the ocean current at 2% of the wind speed (Smith, 1987). However, in a real case, the drift is dependent on more factors than wind and current.

There have been a number of methods that have been developed in an attempt to forecast iceberg drift tracks (Smith, 1987). Some are dynamic models, based on Newton's second law. In these models the various forces acting on an iceberg are evaluated. The acceleration is integrated twice to obtain velocity and position as a function of time. There are statistical models which use the last known positions, together with statistical properties of previous trajectories, to estimate a probability distribution of the iceberg's position and velocity as a function of time. And then there are have kinematic models, which represent the drift track by empirical relationships with other phenomena. These kinematic aspects can be added to statistical or dynamic models. In this thesis, the focus will be on dynamic models.

In general, dynamic models depend on a detailed specification of the winds and currents, of iceberg mass and cross-sectional area, and on a representation of how these influence the drift (Smith, 1987). Usually, currents are considered as the most important parameter for iceberg drift in waters close to the ice edge or within sea ice. In open waters, however, the wave drift may become the most important forcing (Eik, 2009*b*).

The model being dependent on these data, makes it more difficult to make a good forecast of the ice drift. We need to have accurate data from the specific region of the modeled iceberg's location. This is not always easily obtained (particularly not the current); thus, the accuracy of the ice model is compromised.

### Assumptions

The dynamic model explained here, is an iceberg drift model that is valid for the Barents Sea, and is presented by Eik (2009*b*).

To use this model, the current, wind, and wave data of the region is assumed to be known.

The shape of the iceberg is an important feature, and a possible cause for error in the model. According to Kubat et al. (2005), the mass of the iceberg can be expressed by

$$M = C_b \rho_i L^3 \tag{2.3.1}$$

where $M$ is the iceberg mass and $\rho_i$ is the ice density. $C_b$ is a block coefficient equal to 0.45. $L$ is the length of the iceberg.

For simplicity, this model considers an iceberg in open water (waters with low ice concentration). This means that forces from the sea ice need not be considered in the model.

### Equations for Iceberg Drift

The momentum balance that enables us to compute the velocity and the position of the iceberg is given by

$$m \cdot \mathbf{a} = -m\mathbf{fk} \times \mathbf{V_i} + \mathbf{F_a} + \mathbf{F_w} + \mathbf{F_r} + \mathbf{F_p} + \mathbf{F_{si}} \tag{2.3.2}$$

where $m$, $\mathbf{a}$ and $\mathbf{V_i}$ are the mass, acceleration and velocity of the iceberg, respectively. $\mathbf{k}$ is the unit vector in vertical direction, and $\mathbf{F_{si}}$ is the sea-ice drag force, which is equal to zero since when assuming open water surroundings.

The Coriolis frequency $\mathbf{f}$, is given by

$$\mathbf{f} = 2\Omega sin(\phi), \tag{2.3.3}$$

where $\Omega$ is the earth's rate of rotation, equal to $7.2921 \times 10^{-5}$, and $\phi$ is the latitude.

$\mathbf{F_a}$ and $\mathbf{F_w}$ are the drag forces due to wind and current, respectively. These can be calculated by the following equations:

$$\mathbf{F_a} = \frac{1}{2}\rho_a C_a A_a |\mathbf{V_a} - \mathbf{V_i}|\mathbf{V_a} - \mathbf{V_i} \tag{2.3.4}$$

$$\mathbf{F_w} = \frac{1}{2}\rho_w C_w A_w |\mathbf{V_w} - \mathbf{V_i}|\mathbf{V_w} - \mathbf{V_i} \tag{2.3.5}$$

where $C_{a,w}$ are the air and current drag coefficients, $A_a$ is the cross chapteral area above the water surface, and $A_w$ is the cross chapteral area below the water surface. $\rho_{a,w}$ are the air and water densities, respectively, and $\mathbf{V_{a,w}}$ are the wind and current velocities. $\mathbf{V_i}$ is the iceberg velocity, and is subtracted to find the relative velocity.

The wave radiation force is given as

$$\mathbf{F_r} = \frac{1}{4} C_r \rho_w g a^2 L \frac{\mathbf{V_r}}{||\mathbf{V_r}||} \tag{2.3.6}$$

where $C_r$ is the wave drift radiation coefficient, $g$ is the gravity, $a$ is the wave amplitude, $L$ is the characteristic length of the iceberg and $\frac{\mathbf{V_r}}{||\mathbf{V_r}||}$ is the wave direction.

The pressure gradient force is calculated by

$$\mathbf{F_p} = m\left(\frac{d\mathbf{V_{mw}}}{dt} + \mathbf{f} \times \mathbf{V_{mw}}\right) \tag{2.3.7}$$

where $\mathbf{V_{mw}}$ is the mean current velocity.

The first expression on the right hand side in (2.3.2) is the Coriolis force:

$$\mathbf{F_c} = m\mathbf{f} \times \mathbf{V_i}. \tag{2.3.8}$$

The presented model is considered to provide good results in situations with strong winds (and waves) and low currents, while situations with low winds will give less reliable results (Eik, 2009*b*).

For short-term forecasts (1 hour to 2 days) it is not necessary to incorporate deterioration of the iceberg into the model (Kubat et al., 2005). For forecasts over a longer period, deterioration becomes more important.

### 2.3.6 Estimation of Model States using a Kalman Filter

The basic idea of an estimator is to reconstruct the state vector of a dynamic system from a limited set of measurements. No mathematical system model is perfect, because it is only an approximation of the real system. Also, sensors do not provide perfect and complete data about the system. Therefore, state estimation is often necessary.

The Kalman filter (Kalman, 1960) is a powerful tool for the state estimation problem. Kalman filtering is basically a way to separate signal from noise. It is a

recursive procedure that uses the measurements and the previously found results to update the estimates.

To implement a Kalman filter, it is assumed that the process can be modeled in the form

$$\mathbf{x_{k+1}}(t_i) = \mathbf{\Phi_k x_k}(t_{i-1}) + \mathbf{B_k u}(t_{i-1}) + \mathbf{G_k w_k}(t_{i-1}), \tag{2.3.9}$$

and that the measurements will occur in accordance with

$$\mathbf{z_k}(t_i) = \mathbf{H_k x_k}(t_i) + \mathbf{v_k}(t_i) \tag{2.3.10}$$

(Brown and Hwang, 2012).

In these equations

$\mathbf{x_k}$ is the Kalman filter model state vector,
$\mathbf{\Phi_k}$ is the Kalman filter model state transition matrix
$\mathbf{B_k}$ is the Kalman filter model control input matrix,
$\mathbf{u}$ is the system input vector and
$\mathbf{G_k}$ is the Kalman filter model noise input vector.
$\mathbf{w_k}$ is an additive white discrete-time dynamics noise input used in the Kalman filter model, with zero-mean and

$$E\{\mathbf{w_k}(t_i)\mathbf{w_k^T}(t_j)\} = \begin{cases} \mathbf{Q_k}, & t_i = t_j \\ \mathbf{0}, & \mathbf{t}_i \neq t_j. \end{cases} \tag{2.3.11}$$

$\mathbf{z_k}$ is the Kalman filter model measurement vector,
$\mathbf{H_k}$ is the Kalman filter model output matrix, and
$\mathbf{v_k}$ is an additive white measurement noise input that is used in the Kalman filter model.

The measurement noise $\mathbf{v_k}$ is assumed to be independent of $\mathbf{w_k}$, and to have zero-mean, and

$$E\{\mathbf{v_k}(t_i)\mathbf{v_k^T}(t_j)\} = \begin{cases} \mathbf{R_k}, & t_i = t_j \\ \mathbf{0}, & \mathbf{t}_i \neq t_j. \end{cases} \tag{2.3.12}$$

The Kalman filter uses this model to define the time propagation and measurement update equations of the state estimates, $\hat{\mathbf{x}}_\mathbf{k}$ and the state estimate covariance matrix, $\mathbf{P_k}$.

The state estimation is given by

$$\hat{\mathbf{x}}_\mathbf{k}(t_i^-) = \mathbf{\Phi_k}\hat{\mathbf{x}}_\mathbf{k}(t_{i-1}^+) + \mathbf{B_k}\mathbf{u}(t_{i-1}) \tag{2.3.13}$$

$$\hat{\mathbf{z}}_\mathbf{k}(t_i^-) = \mathbf{H_k}\hat{\mathbf{x}}_\mathbf{k}(t_i^-) \tag{2.3.14}$$

where

$\mathbf{z_k}(t_i^-$ is the estimate of the measurement vector before it becomes available, $t_i^-$ is the time just before the measurement update at the $i$th time sample, and $t_{i-1}^+$ is the time at the $(i-1)$ time sample.

The state estimate covariance matrix is given by

$$\mathbf{P_k}(t_i^-) = \mathbf{\Phi_k}\mathbf{P_k}(t_{i-1}^+){\mathbf{\Phi_k}}^T + \mathbf{G_k}\mathbf{Q_k}\mathbf{G_k^T}. \tag{2.3.15}$$

To update the state estimates, the Kalman filter uses

$$\hat{\mathbf{x}}_\mathbf{k}(t_i^+) = \hat{x}_k(t_i^-) + \mathbf{K_k}(t_i)\mathbf{r_k}(t_i) \tag{2.3.16}$$

where $\mathbf{K_k}$ is the Kalman filter gain, and is given by

$$\mathbf{K_k}(t_i) = \mathbf{P_k}(t_i^-)\mathbf{H_k^T}\mathbf{S_k}(t_i)^{-1}. \tag{2.3.17}$$

The residual covariance matrix is computed by

$$\mathbf{S_k}(t_i) = \mathbf{H_k}\mathbf{P_k}(t_i^-)\mathbf{H_k^T} + \mathbf{R_k}, \tag{2.3.18}$$

and the residual vector, $\mathbf{r_k}$ is defined as

$$\mathbf{r_k}(t_i) = \mathbf{z}(t_i) - \mathbf{H_k}\hat{\mathbf{x}}_\mathbf{k}(t_i^-) = (z_T)(t_i) - \mathbf{H_k}\hat{\mathbf{x}}_\mathbf{k}(t_i^-). \tag{2.3.19}$$

Finally, the state estimate covariance matrix is updated using

$$\mathbf{P_k}(t_i^+) = \mathbf{P_k}(t_i^-) - \mathbf{K_k}(t_i)\mathbf{H_k}\mathbf{P_k}(t_i^-). \tag{2.3.20}$$

By iterating this recursive procedure, it is possible to compute the steady state values of the Kalman filter estimates by propagating the state estimates

$$\hat{\mathbf{x}}_\mathbf{k}(t_i^-) = \mathbf{\Phi_k}\hat{\mathbf{x}}_\mathbf{k}(t_{i-1}^+) + \mathbf{B_k}\mathbf{u}(t_{i-1}) \tag{2.3.21}$$

and by updating the state estimates

$$\hat{\mathbf{x}}_\mathbf{k}(t_i^+) = \hat{\mathbf{x}}_\mathbf{k}(t_i^-) + \mathbf{K_k}\mathbf{r_k}(t_i) \tag{2.3.22}$$

### Kalman Filtering with Intermittent Observations

It is possible to combine the dynamic model of an iceberg with images obtained from radars and optical sensors. By tracking an iceberg in the images, its position will be known each time an image is available. The position can then be used as measurements in the Kalman filter. However, due to the nature of satellite image acquisition, the measurements are not continuous. This should be taken into account in the model.

If trying to perform an iteration of the Kalman filtering algorithm with no observations, the result will be that the variance $\sigma \to \inf$. To get around this problem, an approach is to rederive the Kalman filter equations using a "dummy" observation with a given variance when the real observation does not arrive (Sinopoli et al., 2004).

One issue with this methodology is that the time between measurements should not be too long. Research have shown that there exist a critical value for the arrival rate of the observations. If the time between measurements is too long, an unbounded state error covariance occurs (Sinopoli et al., 2004).

# Chapter 3

# Detection and Tracking of Targets

This chapter presents the development and testing of a detection and tracking algorithm.

The purpose of the algorithm is that it should be able to detect all targets in an image. The algorithm should also be able to re-detect these targets in sequential images, thus being able to track the movement of targets in a sequence of images.

To improve the range of images the algorithm can be used on, the detection part of the algorithm is adapted for tracking in satellite images. In particular, the intention is to track targets in images provided by SAR-sensors.

The method chosen for the algorithm is object based, as described in Section 2.3.1. Similar to the ITSARI algorithm (Silva and Bigg, 2005; Hall et al., 2012), some features are chosen to represent the target. These target features are then used to compare the targets in sequential images. However, instead of using a boundary representation, it is in this thesis chosen to use a set of geometrical features to represent the targets.

When using an object based tracking method it is important that each target maintain a distinctive shape. If a target is in close proximity to other targets, it can be difficult to distinguish one target from another. This can compromise the algorithm's ability to identify the shape of a target. In an attempt to solve this issue, a set of image processing methods is combined with the purpose of identifying all target boundaries. By doing this, the algorithm should be able to identify the boundary of a shape despite a high amount of surrounding targets.

In the following sections the detection and tracking algorithm will be explained in detail. The algorithm is implemented MATLAB, and is tested on a synthetic test case for verification.

## 3.1 Image Segmentation and the Geometrical Representation of Targets

The detection and tracking of targets in this thesis is carried out using an algorithm divided into two significant parts: the identification of objects within an image, and the matching of objects from one image to the next. In this section the identification of the objects will be explained.

Firstly, the image is loaded into MATLAB. Then, a segmentation of the image is necessary. For this purpose, the images are converted to grayscale images, with 256 gray levels. The global Otsu thresholding method can be then implemented by applying the expression given in (2.2.2). By using this method, it is possible to find a suitable gray level threshold, which will segment the image into two different types of segmentations: targets and background. The result of the segmentation is a binary matrix with zeros representing the background, and ones representing the targets. Each cell in the matrix represent a pixel in the image. For images with targets that have a distinct shape with a clear brightness difference from the background, this amount of image processing is sufficient.

However, to adjust the algorithm to work with noisy satellite images, and to properly separate targets from each other, the watershed transform is chosen for segmentation of the image. To avoid oversegmentation, the basin dynamics method is applied to suppress catchment basins with shallow minima. This is done by the function `imhmin` in MATLAB, which uses a 8-connected neighborhood to find the minimas. To use this function, it is necessary to find a suitable threshold to decide which minimas that should be excluded. This is done by finding the Otsu threshold for each image, and then increasing this threshold by a percentage unique to each scenario. This way, the threshold for the basin dynamics method is dynamic and will change according to the brightness threshold of the image.

After this, all targets are made completely continuous by filling any holes that might exist. This is done by the MATLAB function `imfill`.

When the segmentation of the image is finished, it is possible to extract the required properties, which will be used in the tracking algorithm. This can be done very efficiently by using a combination of the functions `bwlabel` and `regionprops` on the segmented image. These functions will label all objects found in the image, and then measure the properties of the objects. These properties are geometrical features which defines each of the detected targets. The features extracted are area, perimeter, and major and minor axis length. The values are all given in number of pixels, and are stored in a property matrix. In addition to this, the $x$- and $y$-coordinates of the center pixel for each target are also stored.

If not wanting to track all targets in the image, the algorithm can remove all targets with an area smaller or bigger than than a given limit. This limit can be changed according to what kind of targets the algorithm is looking for, and according to image resolution.

## 3.2 The Tracking Algorithm

This section explains the methodology behind the tracking of targets will be explained. The basic workflow of the program is presented as a flow chart in Figure 3.1.

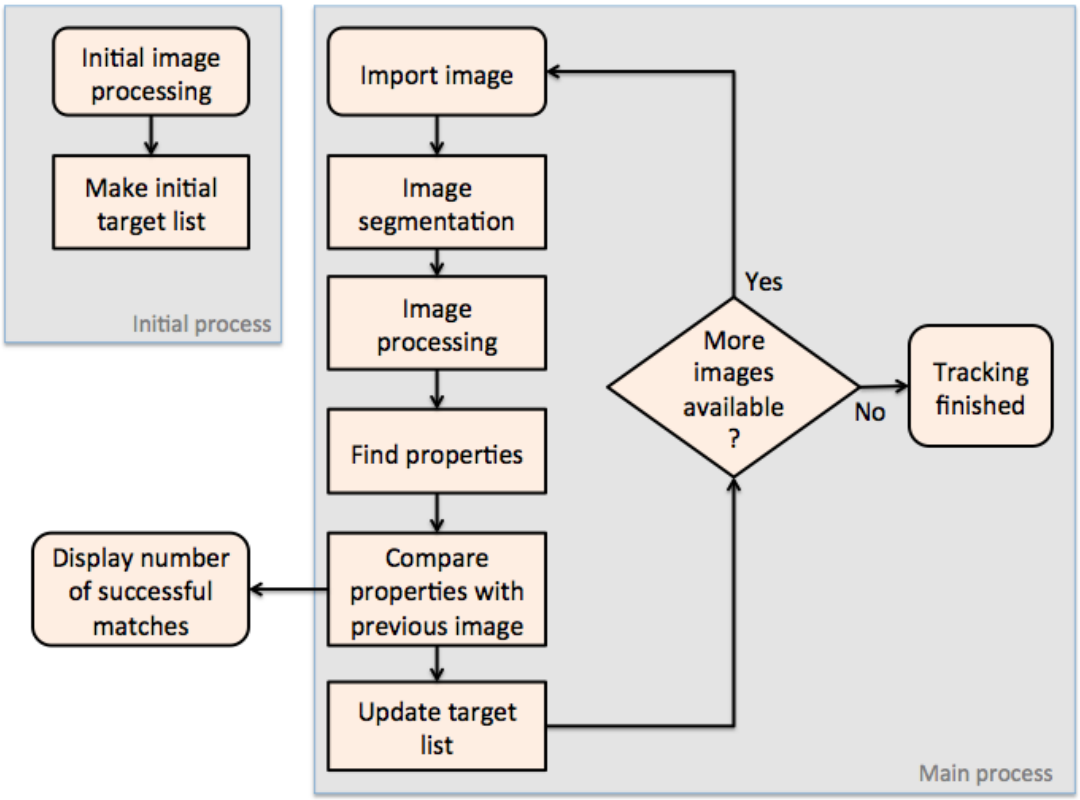


Figure 3.1: Flow chart of the detection and tracking process.

When initializing the tracking algorithm, the user must specify a value, $n$, which tells how long the image sequence is. The image index can thus be denoted by $i = 1, 2, ..n$. The algorithm will then launch an initial process, which loads the first image, segments it, and makes a property matrix which includes all the the properties for the targets in the image. After this, the algorithm will start looping

through the rest of the images: $i = 2, 3, ..n$. Image $i$ is uploaded, segmented, and then the target properties are found. These are then stored in a temporary property matrix, which is used for comparison with the property matrix from image $i - 1$.

To achieve a successful match between two targets, some criteria must be achieved:

1. The target must not be from the same image
2. Targets must have similar perimeter
3. Targets must have similar area
4. Targets must have similar major axis length or minor axis length

The first criteria will always be fulfilled, due to the structure of the algorithm. How similar the properties should be is decided by how large the allowed deviation of a target's shape is in the sequence of images. It is necessary to allow some deviations due to two factors; loss of resolution and deformations in target shape. The allowed deviations varies with each test scenario, and can be decided by checking the similarities of some targets in the the scene before initiating the tracking.

To limit the processing time, the algorithm only compare one property at a time. The properties are checked in the same order as they are stated in the list above. This way, if the two targets being compared have dissimilar perimeters, the algorithm will not compare the remaining properties. Consequently, the algorithm will rule out the most unlikely matches, to save processing time.

When a target from image $i - 1$ is re-detected in image $i$, the match is recorded in a detection list. This list contains a cell for each target in the property matrix, and keeps track of how many times a target have been tracked in the sequence of images.

When the tracking algorithm have finished comparing all targets in the property matrix for image $i - 1$ and the temporary matrix for image $i$, the property matrix will be updated. All targets which are found in both images are already in the property matrix. These entries will not be altered. Targets which are in image $i-1$, but are not found in image $i$, will be removed from the property matrix. This is done under the assumption that if a target is no longer within the location of interest, it will not return. This is to prevent the property matrix from becoming excessively big. The argument for this assumption is that since ice targets usually move with the current, the direction will most likely be similar for all targets. Thus, when a target drifts out of the area of interest, it will most likely not drift back again. This is not the case for vessels targets, but for vessels it is mainly the detection and not the tracking which is of importance.

Lastly, targets which are detected in image $i$, but are not matched with any of the targets in image $i-1$ are added as new objects in the property matrix. The property matrix is now fully updated, and can now be used for the comparison with image $i+1$. The segmentation, comparing, and updating will be repeated for all the images in the sequence: a total of $n$ times.

## 3.3 Synthetic Data Testing

To verify the tracking capabilities of the algorithm, a set of images (Figure 3.2) containing a total of ten different objects were synthetically made. Each object is labeled with an identification number to show the correlation between objects in each image.

The synthetic data represent a trivial case with easily distinguishable targets. The purpose of this test scenario is to show how the tracking algorithm works, and that the logic behind the algorithm is not faulty. It is, however, important to note that this test does not verify the algorithm's ability to detect targets in satellite imagery. It only tests the algorithm's ability to compare properties, and the process of updating the property matrix between each sequential image.

The deviations allowed in the geometrical representation for each shape are found by comparing some of the targets which are known to be the same. The percentage of deviation allowed for each property are shown in Table 3.1.

Table 3.1: Deviations allowed for the geometrical parameters in the matching process for the tracking test

| Geometrical parameter | Deviations allowed [%] |
|---|---|
| Area | 1 |
| Major axis length | 1 |
| Minor axis length | 1 |
| Perimeter | 2 |

These deviations were implemented in the comparison part of the tracking algorithm, and the algorithm was then tested on the four images. Table 3.2 shows the results from the object tracking.

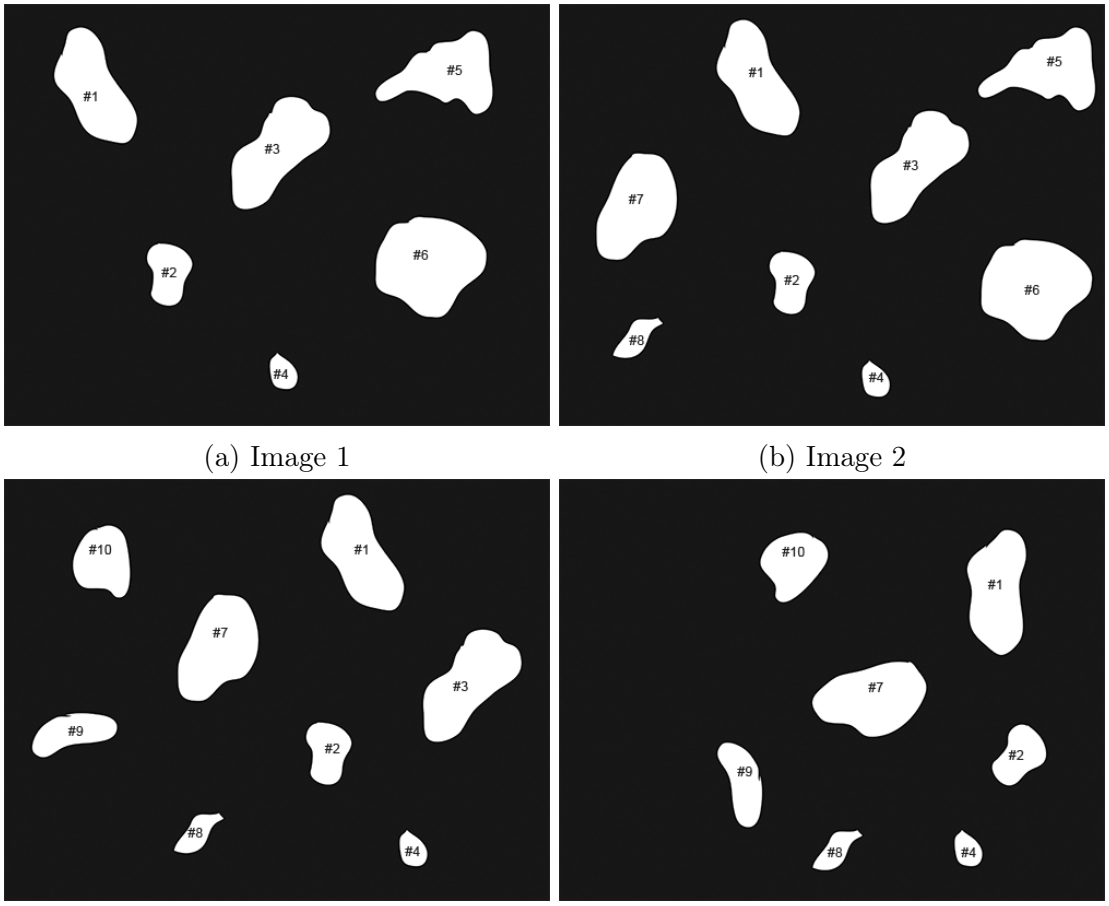


(a) Image 1

(b) Image 2

(c) Image 3

(d) Image 4

Figure 3.2: Images containing objects for synthetic iceberg tracking.

For the four images, all targets are accurately detected and tracked. In all image pairings, the algorithm is successful in matching the six targets which appear in both images. In image pairings 1-2 and 2-3 the algorithm recognizes the targets 7 and 8, and targets 9 and 10, respectively, as new objects. In addition, in image pairings 2-3 and 3-4 the algorithm shows its ability to keep track of objects which are not found. Consequently, the logic behind the tracking is sufficient.

However, the algorithm does not take into consideration the possibility of a target having a successful match with several other targets in the same image, also called having false alarms. For a scenario where there are many very similar objects, or where the targets are very small and thus have less distinct shapes, this can be a problem. In addition, the tracking capabilities are highly influenced by the choice of deviations allowed for the geometrical representation of a target. It is important

Table 3.2: Tracking results of synthetic data testing.

| Image pairing | Matches found | Objects not found | New objects | Correct matches |
|---|---|---|---|---|
| 1-2 | 6 | 0 | 2 | 100 % |
| 2-3 | 6 | 2 | 2 | 100 % |
| 3-4 | 6 | 3 | 0 | 100 % |

that these deviation limits are set to suitable values to ensure that all targets are successfully tracked while not giving any false alarms.

As mentioned earlier, the deviations of the properties of a target is due to loss of resolution or by deformations in the shape of the target. Deformations can occur due to natural causes like when a target crashes into another target, melting (in the case of ice targets) or smaller targets being attached to the target in question. These are all factors that should be considered in a real case scenario. However, since this test scenario was made synthetically there were no deformations of the targets. The only way a target changed was by translation and rotation, thus the limit for the deviations allowed could be very strict. All deviations were due to pixel differences between each image. In this scenario, these differences were small, but when processing satellite images covering large areas the differences will rely heavily on the image resolution. It is then likely that the deviations will increase.

# Chapter 4

# Classification of Targets

By adding a classification feature to the tracking algorithm, the functionality of the algorithm could be enhanced to a new level. The goal was that this feature should be able to classify the detected targets by deciding if they were ice targets or vessel targets. For simplicity, it was decided not to distinguish between different ice types like ice floes, icebergs, brash ice etc.

In the following sections the development and testing of this added feature will be explained.

## 4.1 Classification Feature

The classification feature made is based on target motion. By observing how targets move, it is obvious that vessels and ice have different motion patterns. These patterns will be further discussed in Section 6.2. Often, a distinct difference between ice and vessel motion is the speed of travel. The speed of an ice target is limited to a lower value than the speed of a vessel, which is a piece of information that can be used to distinguish between these two types of targets.

By calculating the total distance traveled for each target between each sequential image, the speed of travel for all targets are available. That is, of course, given that the timestamp for each image is known. Then, by setting an upper speed limit for ice targets, all targets maintaining a speed higher than the limit will be classified as vessels.

The total distance traveled for a target is given by the translation of the target's centroid. Thus, to find the distance, it is necessary to find the centroids for all

targets in all images. The coordinates of the centroids are given as the row and column number for the cell representing the centroid-pixels in the image matrix.

To calculate the distance $d$ between the centroid coordinates of a target, the formula for the Euclidian distance is used:

$$d = \sqrt{(x - x_0)^2 + (y - y_0)^2} \tag{4.1.1}$$

where $(x_0, y_0)$ are the column and row coordinates of the target in the first image, respectively, and $(x, y)$ are the column and row coordinates of the target in the second image. The resulting value is the total distance traveled, given in pixels. To convert this distance from pixels to meters, the value is multiplied with the resolution of the image. Then, the speed of travel can be found using the time difference between the two images in question.

One assumption that has to be made when using this method, is that all images have the exact same geographical location. If this is not the case, the distance calculated will not be correlated with the actual travel distance of the targets. A possibility is to keep track of how the position of the images is in relation to each other, and then take this into consideration when calculating the distance. However, when tracking in a long sequence of images, this can soon become complicated.

## 4.2 Synthetic Data Testing

To verify the classification capabilities of the method, the two scenarios shown in Figure 4.1 were synthetically made. These two images are both of size 800 x 600 pixels, and represent a scene with different targets surrounded by water. Each target is labeled, to show the correlation between the targets in image 1 and image 2.

The rectangles represent vessels, while the other shapes represent ice objects. To make the scenario as realistic as possible, the vessel targets have been moved so that their traveled distance is higher than the traveled distance of the ice targets. However, one of the vessels (target 5), is not moved far enough to be classified as a vessel. This is to illustrate the fact that this classification feature will not always be able to accurately decide if a target is of type vessel or ice. It can, however, decide if a target is not ice, and thus it is possible to deduct that is must be a vessel. The logic can be explained like this; if a target has a speed of travel higher

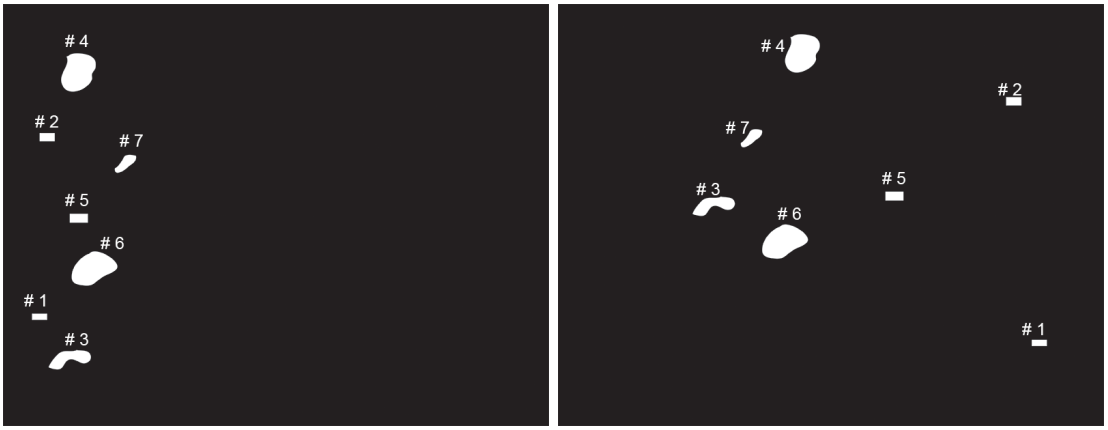


(a) Test image 1 (b) Test image 2

Figure 4.1: Test images to test the classification feature in the tracking algorithm.

than the speed limit, it is definitely not ice. It must therefore be a vessel. However, if the speed is below the speed limit, the target type can be both vessel and ice. Thus, the results will be inconclusive.

The deviations allowed for this set of images in the matching part of the tracking algorithm was found by testing the similarities of a few targets. The resulting values are given in Table 5.8.

Table 4.1: Deviations allowed for the geometrical parameters in the matching process for the classification test

| Geometrical parameter | Deviations allowed [%] |
|---|---|
| Area | 20 |
| Major axis length | 5 |
| Minor axis length | 10 |
| Perimeter | 5 |

The speed limit for ice targets was in this scenario set to 0.25 $^{m}/_{s}$, and the resolution was decided to be 40 x 40 meters per pixel.

The tracking algorithm with the added classification feature was then tested on the two images. All targets were successfully detected in the first image, re-detected in the second image, and there were no false detections. The classification results are shown in Table 4.2.

Table 4.2: Tracking results of synthetic data testing.

| Target number | Speed of travel [$^m/_s$] | Target type |
|---|---|---|
| 1 | 0.30215 | Vessel |
| 2 | 0.28022 | Vessel |
| 3 | 0.12018 | Vessel or ice |
| 4 | 0.11532 | Vessel or ice |
| 5 | 0.17747 | Vessel or ice |
| 6 | 0.093699 | Vessel or ice |
| 7 | 0.051212 | Vessel or ice |

Target number 1 and 2 were successfully classified as vessels. Target number 5, as intended, was not. Consequently, the classification feature will successfully classify targets which move at a speed higher than a given speed limit.

# Chapter 5

# Case study on the East Greenland Coast

This chapter presents a case study where the detection and tracking algorithm is carried out on a real case scenario. Two pieces of ice are tracked in a sequence of images to show the algorithms ability to track certain objects of interest. Then, a test for classification is performed on a set of vessel targets, showing the algorithm's ability to identify targets as vessels.

## 5.1 Data Acquisition

The images used in this case study is a time-sequence of images acquired by the RADARSAT-2 satellite in August 2013 on the East Greenland coast. The series consist of 15 images, over a span of 12 days. The imagery is acquired by a synthetic aperture radar, with the modes ScanSAR and Standard Quadpol.

RADARSAT is an official mark of the Canadian Space Agency, and the imagery was delivered by the MDA Geospatial Services. The imagery was then distributed by the Kongsberg Satellite Services (KSAT).

All the images were georeferenced, which enabled matching the images with positional data. To find these positional data, the Next ESA SAR Toolbox (NEST), supplied by the European Space Agency (ESA), was used.

In addition, AIS-data has been collected for the same time period as the images. The data was procured by The Norwegian Coastal Administration, using the satellites AISSat-1 and AISSat-2, and consists of AIS-messages from vessels all over the

globe. Each image from the RADARSAT-2 satellite was matched with the AIS data, and used as an area restriction when searching the AIS-data for vessels. A more detailed description of this process follows in Section 5.3. Table 5.1 shows all image acquisition dates and associated vessels detections.

Table 5.1: Overview of satellite images and corresponding AIS-data

| RADARSAT-2 | | | AIS data |
|---|---|---|---|
| Image number | Acquisition date | Mode | Vessels found |
| 1 | 20-Aug-13 | Dual-pol | 2 |
| 2 | 21-Aug-13 | Dual-pol | 4 |
| 3 | 22-Aug-13 | Dual-pol | 3 |
| 4 | 23-Aug-13 | Dual-pol | 3 |
| 5 | 24-Aug-13 | Dual-pol | 3 |
| 6 | 24-Aug-13 | Quad-pol | 1 |
| 7 | 25-Aug-13 | Dual-pol | 3 |
| 8 | 26-Aug-13 | Quad-pol | 0 |
| 9 | 26-Aug-13 | Dual-pol | 3 |
| 10 | 27-Aug-13 | Dual-pol | 4 |
| 11 | 28-Aug-13 | Dual-pol | 5 |
| 12 | 29-Aug-13 | Dual-pol | 3 |
| 13 | 30-Aug-13 | Dual-pol | 3 |
| 14 | 30-Aug-13 | Quad-pol | 0 |
| 15 | 31-Aug-13 | Dual-pol | 4 |

In the case study, the satellite images will be referred to by the image numbers in this table.

## 5.2 Tracking Two Pieces of Ice

Two pieces of ice have been tracked on the East Coast of Greenland in August 2013, using the images from Table 5.1 in HH polarization. Local sub-images of the two targets are shown in Figure 5.1.

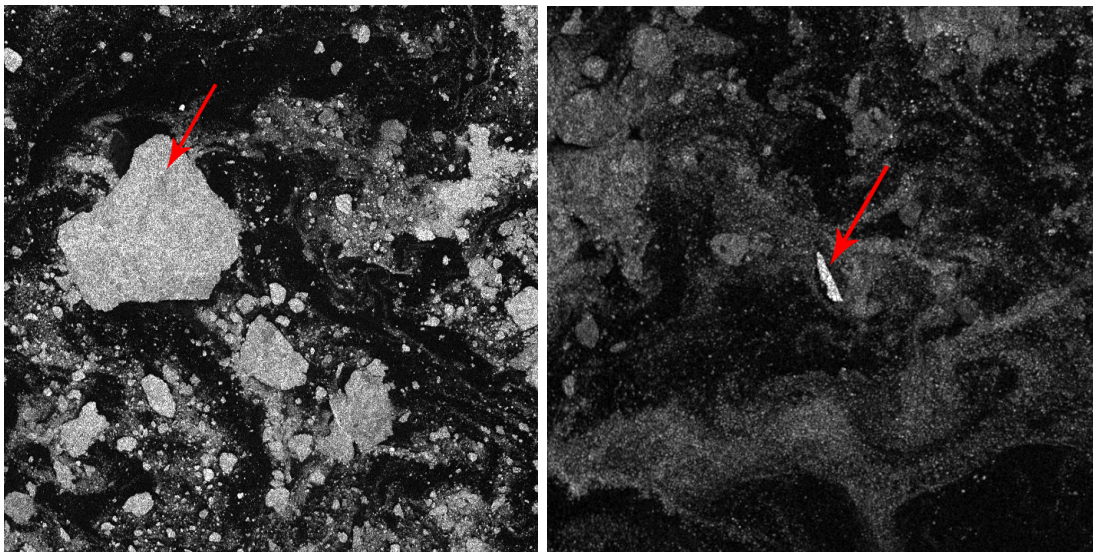

(a) Local image of ice object 1. (b) Local image of ice object 2.

Figure 5.1: Local images of two pieces of ice. RADARSAT-2 Data and Products © MacDonald, Dettwiler and associates LTD. (2013) – All Rights Reserved.

Both ice floes are in close proximity to other clusters of ice. Consequently, identification of the target boundaries is important to distinguish the wanted targets from surrounding targets.

The first piece, ice object 1, is a huge ice floe with a length of over 20 km. The ice floe was tried tracked in the 15 satellite images available. For simplicity, sub-images containing a more local region of the ice object of interest were used. This was to avoid having to process too much data, and thus using an unnecessary amount of time. The resolution of the images are 100 x 100 meters per pixel.

In Figure 5.2 an example of the segmentation process is shown. It shows the segmentation of the detected object in a sub-image of satellite image 3, which is the same image as is shown in Figure 5.1a.

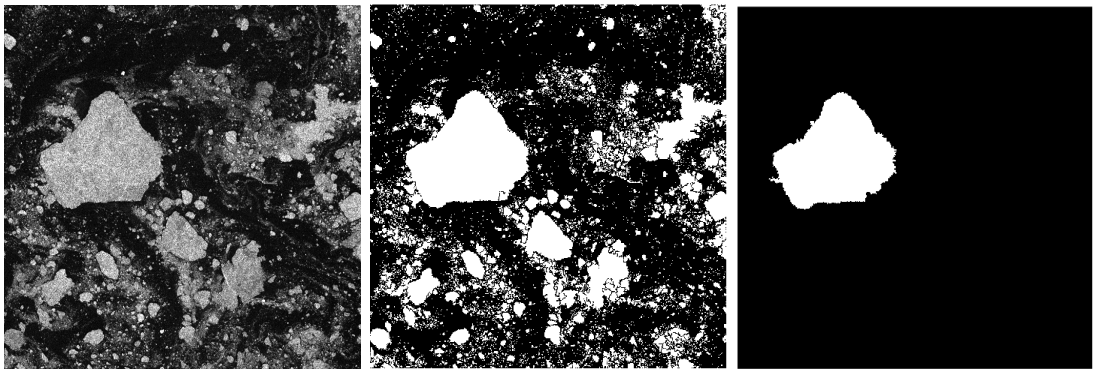

(a) A local section of image 3.

(b) (a) after the image processing is done.

(c) The object of interest alone

Figure 5.2: The segmentation process of ice object 1 in satellite image 3.

In Figure 5.2c all surrounding targets are removed to illustrate how the segmented version of ice object 1 looks. The resulting segment does have a few protrusions due to attached targets. Also, some cut offs due to oversegmentation are observed. However, these are small deviations compared to the total area of the object.

The deviation limits were set by comparing the properties of the target in a few images. The chosen limits are shown in Table 5.2.

Table 5.2: Deviations allowed for the geometrical representation of ice object 1

| Geometrical parameter | Deviations allowed [%] |
|---|---|
| Area | 5 |
| Major axis length | 5 |
| Minor axis length | 5 |
| Perimeter | 25 |

By allowing these deviations when comparing the geometrical representation of the target in each image, ice object 1 was successfully detected in image 1-5, 7 and 9 by the detection and tracking algorithm. Table 5.3 displays the distance traveled and the average speed for the target between each image pairing. For the calculation of the distance traveled the Haversine formula was used. This formula will be explained in Section 6.2 while discussing motion patterns of targets. The exact timestamps of the satellite images, used for calculating the average speed, can be found in Appendix C.1.

Table 5.3: Results from the detection of a ice object 1 in a sequence of satellite images from the East Coast of Greenland

| Start date | End date | Distance traveled [km] | Average speed [m/s] |
|---|---|---|---|
| 20-Aug-2013 | 21-Aug-2013 | 11.0985 | 0.1311 |
| 21-Aug-2013 | 22-Aug-2013 | 6.1451 | 0.0726 |
| 22-Aug-2013 | 23-Aug-2013 | 7.9975 | 0.0882 |
| 23-Aug-2013 | 24-Aug-2013 | 4.1974 | 0.0496 |
| 24-Aug-2013 | 25-Aug-2013 | 5.8279 | 0.0689 |
| 25-Aug-2013 | 26-Aug-2013 | 18.4961 | 0.1535 |

The reason for the target not being detected in image 6 and 8 was that these images are Standard Quadpol images, which have a lower swath width than the other images. Consequently, images 6 and 8 cover a much smaller are, and therefore the target was not included.

Manually, ice object 1 was also detected in satellite image 10. There, the ice floe still had a distinguishable shape which could be manually recognized as the same target detected in the preceding images. However, the shape of the target had become too deformed to be successfully matched with the preceding target representations by the algorithm. Further on, in the images following image 10, the target was too deformed to even be recognized as the same object.

Table 5.4 shows the properties that represents the target in each of the images, including the "unmatched" target in image 10. Figure 5.3 contains the target segmentations corresponding to these properties.

From the sequence of images it becomes obvious that the target changes over time. The algorithm is invariant to rotation, however, the amount of deformations allowed is limited. Some deformations are accepted, which can clearly be seen by the segments in figures 5.3a-5.3g, where the boundaries of the target gradually changes. However, when comparing the segment in image 10 with the preceding images, a more distinct difference in area can be observed. Since the deviation in area is higher than the allowed limit of five percent, the algorithm concluded that the target is too different to be matched with the previous occurrences of the target.

When looking at Figure 5.3d compared to the other segments in Figure 5.3, it is obvious that the shape of the target have been altered considerably. Therefore,

Table 5.4: Geometric properties for ice object 1

| Image number | Area | Perimeter | Major axis length | Minor axis length |
|---|---|---|---|---|
| 1 | 35132 | 1031 | 235 | 201 |
| 2 | 35778 | 954 | 240 | 203 |
| 3 | 34694 | 838 | 236 | 198 |
| 4 | 34329 | 862 | 234 | 197 |
| 5 | 36509 | 981 | 234 | 206 |
| 7 | 35410 | 883 | 241 | 198 |
| 9 | 36065 | 1175 | 250 | 195 |
| 10 | 31185 | 1120 | 220 | 193 |

the author finds it acceptable that the algorithm is not able to make a match with this target. Making a tracking algorithm invariant to any deformations would be a very complex and challenging task, which would result in a scope of work too large for this thesis.

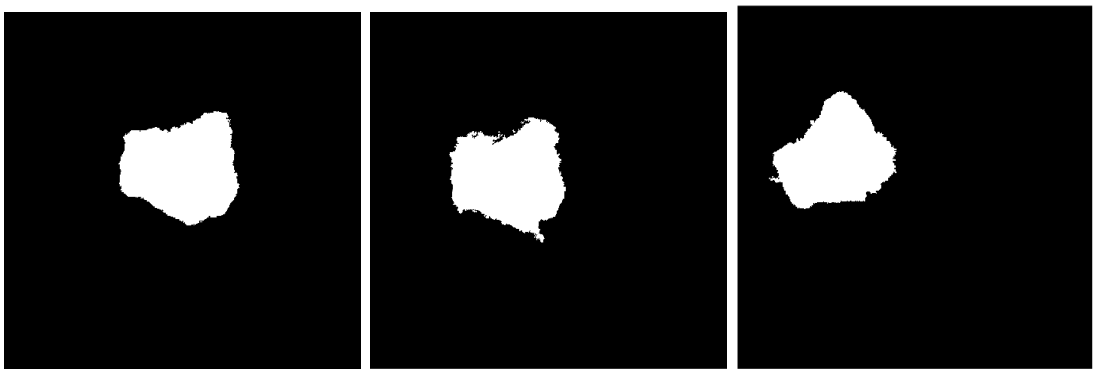

(a) The segment in image 1 (b) The segment in image 2 (c) The segment in image 3

(d) The segment in image 4 (e) The segment in image 5 (f) The segment in image 7

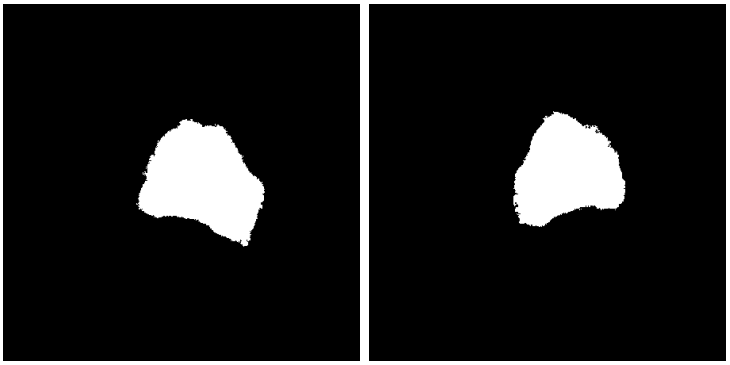

(g) The segment in image 9 (h) The segment in image 10

Figure 5.3: The segmentations of ice object 1 in each image

Next up, the tracking algorithm was tested on ice object 2. This object is also an ice floe, but is smaller in size than ice object 1. Yet, with a length of 3 km, ice object 2 is still a large ice floe.

Following the same procedure as with ice object 1, the deviation limits were set by comparing the properties of the target in a few images. The chosen limits are shown in Table 5.5.

Table 5.5: Deviations allowed for the geometrical representation of ice object 2

| Geometrical parameter | Deviations allowed [%] |
|---|---|
| Area | 30 |
| Major axis length | 10 |
| Minor axis length | 10 |
| Perimeter | 85 |

As a result, the object was detected in images 2, 4, 5 and 7 by the algorithm. The distance traveled and the average speed for the target between each image pairing can be seen in Table 5.6.

Table 5.6: Results from the detection of ice object 2 in a sequence of satellite images from the East Coast of Greenland

| Start date | End date | Distance traveled [km] | Average speed [$^m/_s$] |
|---|---|---|---|
| 21-Aug-2013 | 23-Aug-2013 | 11.0322 | 0.0629 |
| 23-Aug-2013 | 24-Aug-2013 | 11.6509 | 0.1376 |
| 24-Aug-2013 | 25-Aug-2013 | 9.1310 | 0.1079 |

The detected segments of the target is presented in Figure 5.4.

When comparing these segments with the segments of ice object 1, it can be observed that the shape of the ice object 2 is more compromised by protrusions and added sections. Ergo, it can be concluded that the identification of the target boundary is more challenging when the target is smaller, and the deviation limits must be set accordingly.

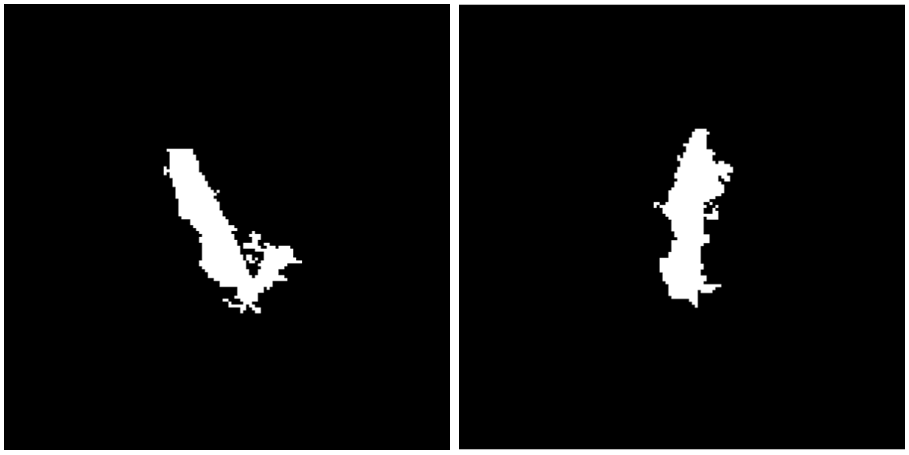

(a) The segment in image 2



(b) The segment in image 4

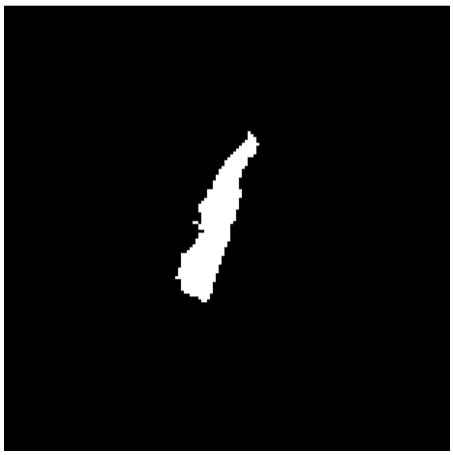

(c) The segment in image 5

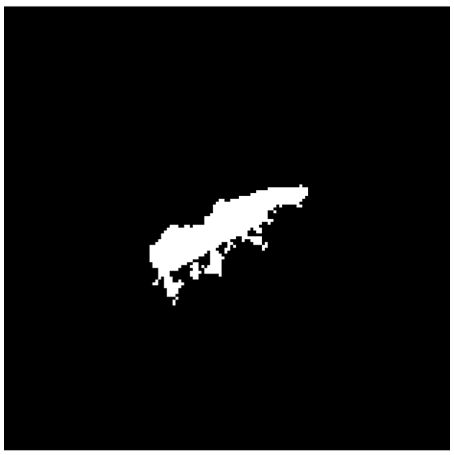

(d) The segment in image 7

Figure 5.4: The segmentations of ice object 2 in each image

Similar to the tracking of ice object 1, the object was manually detected in an image that did not result in a successful detection from the algorithm. This was in image 1, and the object is shown in Figure 5.5.

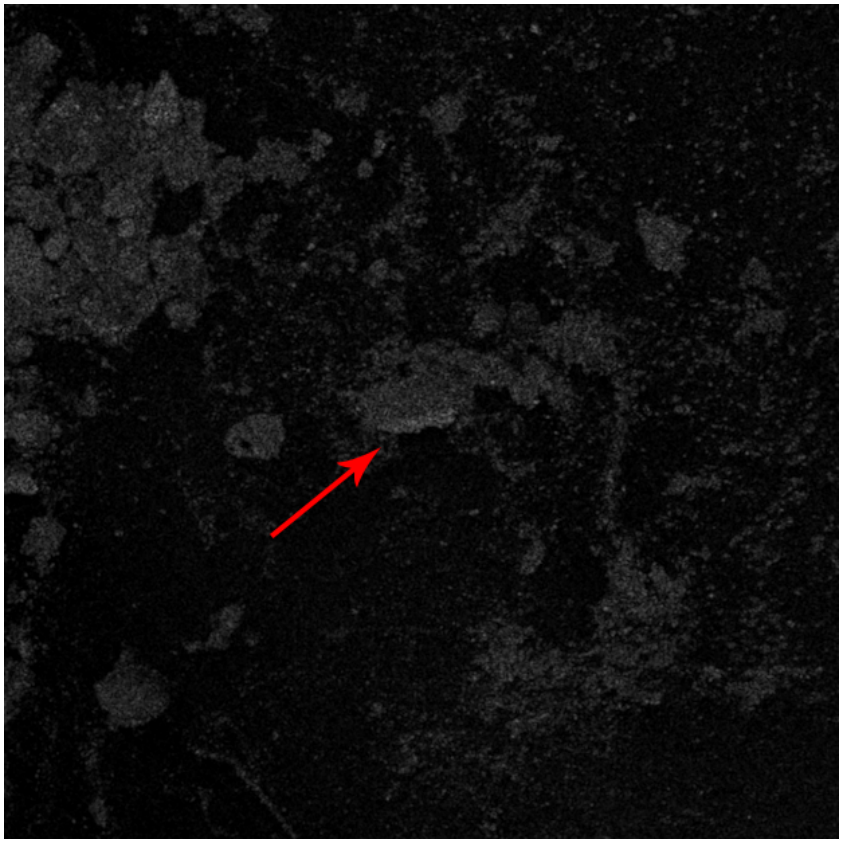

Figure 5.5: Ice object 2 in satellite image 1.

In the case of ice object 1, the "untracked" target segment was detected, but too deformed to be successfully matched by the algorithm. In contrary to this, ice object 2 could not even be detected in image 1. As can be seen from Figure 5.5, the target is barely distinguishable by sight, and the brightness is not very different from the background. However, since ice object 2 has a slightly higher brightness return, the target is most likely thicker and have more ridges than the surrounding ice. As can be deducted from this, the ice surrounding the target must be a combination of thinner ice floes and brash ice. Further on, it can be concluded that the detection process of the algorithm is insufficient in these circumstances.

So, to conclude, the detection and tracking capabilities of the algorithm relies on the successful shape matching of objects between one image and the next. For the detection to be successful, the objects must be present in both images, and it must have a distinct shape with a brightness return which is moderately different than the background. If an object is identified in both images then it should be matched as long as the shape has not changed dramatically.

The algorithm is robust to rotations, and allows deformations to some extent. Deformations can be caused by natural causes, for instance when a target is split in several pieces due to forces working on the target. A deformation can also be caused by adjacent ice attaching itself to the target. In these circumstances, the segmentation of the algorithm is not always sufficient enough to identify the actual target boundaries, which will therefore result in protrusions in the segment of the target. This kind of deformation can prove to be problematic when tracking small targets. As the case with ice object 2 proved, the deviations allowed must be set to a high value for the algorithm to successfully match the target segments. When comparing the deviation limits used for ice object 1 and ice object 2, the limits were set significantly higher for ice object 2.

When deciding the limits for the deviations, it is important to find a good balance. If the limit is too strict the algorithm may miss the correct matching. However, if the algorithm is too tolerant to deviations, it will most likely match the target with more than one object, hence, cause false alarms. Finding a limit which balance these issues can be difficult when tracking many targets of varying sizes.

## 5.3 Finding Vessels in Images Using AIS-Data

Before testing the classification capabilities of the algorithm, it was necessary to find truth data to be used for verification. For this purpose, it was decided to use data from the Automatic Identification System (AIS) to identify all vessels in the area of interest. It was concluded that this would be sufficient as truth data, because all vessels of a certain size are required to use this system.

To classify objects in images as vessels, the AIS data needed to be correlated with the images. To do this, it was necessary to find the desired area in which to look for instances in the AIS data file. The geographical location of each image was found from geolocation, and then used as a restriction while sorting through the AIS data files. Figure 5.6 shows the geographical location, and thus the AIS-data restriction, for each of the 15 images. The geographical locations and timestamps for all images can be found in Appendix C.

Further on, a time restriction was required, since each AIS-datafile contained 24 hours worth of data. Due to the nature of AIS data collection, signals from the vessels are not continuously available, but is available as a list of messages sent from the vessels. The frequency of these messages are dependent on the satellite passing rate, which can vary from hours to days. Because of this, the probability for matching AIS data with the timestamps of the images is very small. A larger

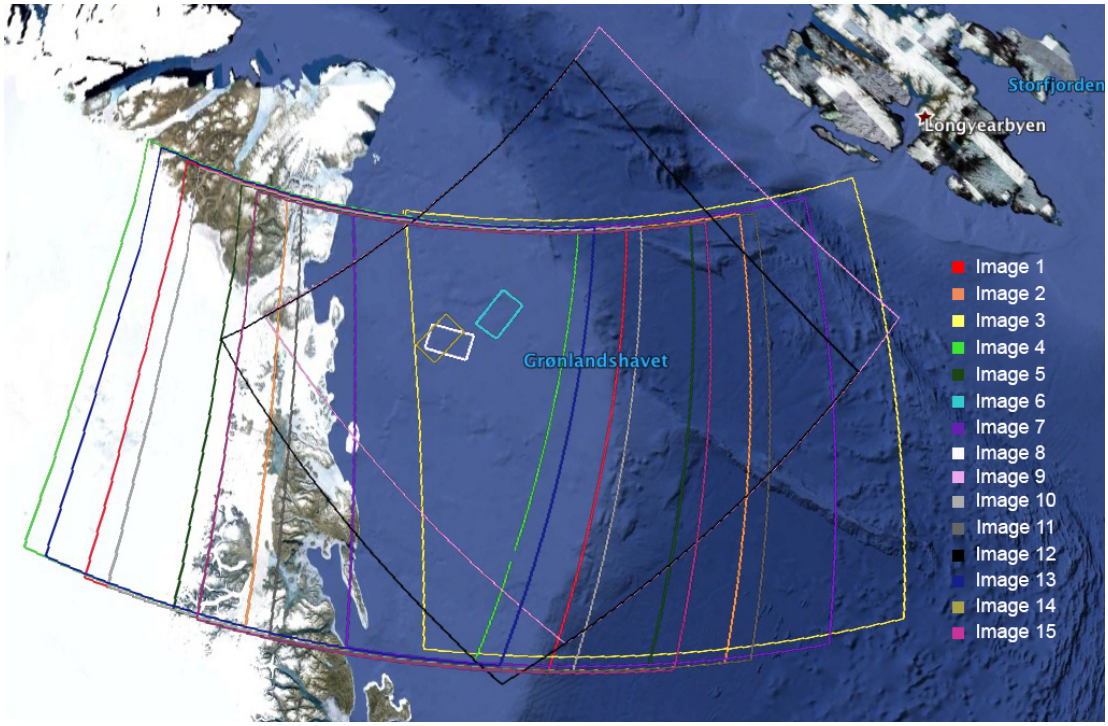


Figure 5.6: Overview of the geographical locations for the images. Image Landsat ©2015 Google earth.

timeframe was therefore set when searching for vessels in the given geographical location of the image.

Initially, the time frame was three hours long; starting 1.5 hours before the image's timestamp and ending 1.5 hours after the image's timestamp. This resulted in a list of AIS-messages from several different vessels for each image. To find the exact latitude and longitude position for each vessel, interpolation was performed using the position and timestamp from the AIS-messages and the timestamp of the image of interest. In some cases it was necessary to extend the time frame to have enough input for the interpolation. By using the resulting latitudes and longitudes, it was possible to manually identify each vessel in each of the images. A list of all identified vessels and their positions can be found in Appendix C.2.

## 5.4 The Classification Feature

Initially, it was necessary to decide the upper speed limit for the ice targets. This limit is the deciding factor of the classification feature in the algorithm, and is therefore an important parameter. Of the two pieces of ice being tracked in Section 5.2, the highest average speed reached was 0.1535 $m/s$. By visually observing the ice surrounding these targets, it was found that all the ice had a common movement pattern, which is most likely due to the Greenland East Current. It follows that the average speed observed for the two pieces of ice is indicative for the speed of all ice targets in the area. By adding some margins to the maximum speed observed, the limit was set to 0.25 $m/s$. A further investigation on the movement patterns of ice, and on the determination of the speed limit will be presented in Section 6.2.

The classification feature was tested on a sub-image of satellite image 2 and a sub-image of satellite image 3, both covering the same geographical location. The sub-images contained targets of similar size and brightness return. The images, with the vessel targets marked by rectangles, and in enlarged versions, can be seen in Figure 5.7.

In each image, two targets (vessel 1 and vessel 2) had been identified as vessels by the AIS-data processing. These have a strong brightness return, which results in bright spots in the satellite images.

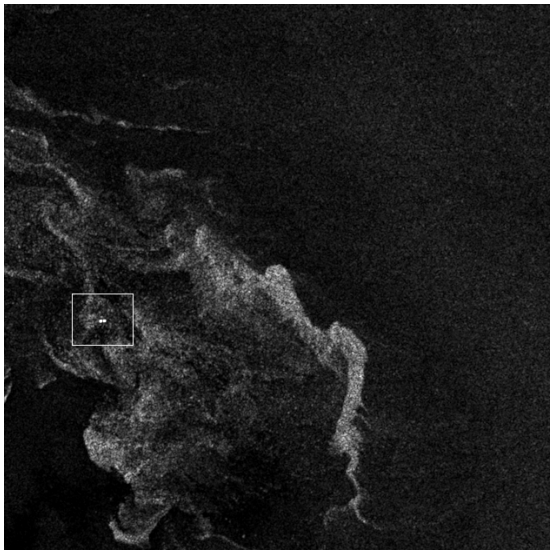

(a) Vessel 1 and 2 in sub-image of image 2.

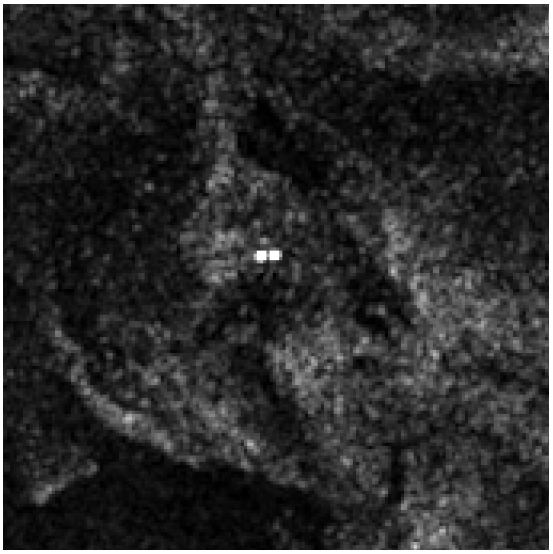

(b) Enlarged version of 5.7a.

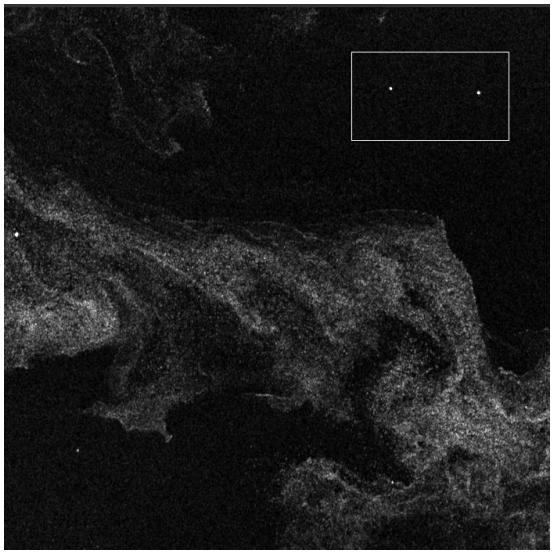

(c) Vessel 1 and 2 in sub-image of image 3.

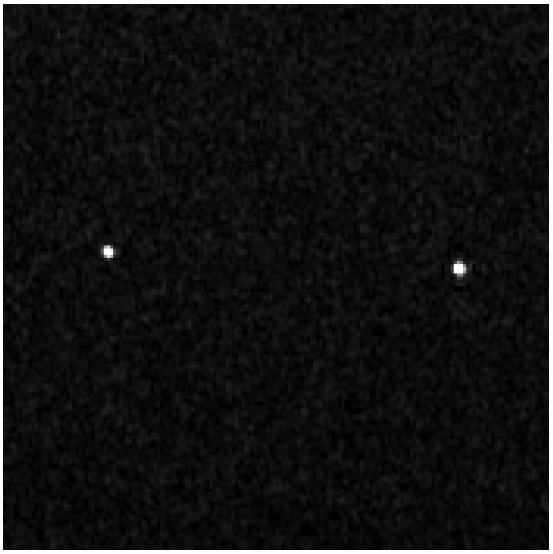

(d) Enlarged version of 5.7c.

Figure 5.7: Vessels in satellite images.

The resolution of the images is 50 x 50 meters per pixel and the images are converted to grayscale images with 256 gray levels prior to segmentation.

When segmenting the images, a high brightness threshold was used. The threshold was found by adding a constant value to the Otsu threshold found in each image. The result of this, was that the parts in the images in Figure 5.7 which look like smoke or clouds were removed. These areas typically consist of slush and brash

ice, and makes it difficult to distinguish targets. Since the purpose of this scenario was to test the classification capabilities of the algorithm, it was better to remove these parts entirely, as they were not vessels. Thus, it was possible to only focus on similar targets which look identical by sight.

When segmenting the images using a threshold of graylevel 240, three targets were detected in image 2 and five targets were detected in image 3. These targets can be seen in the segmented images in Figure 5.9. The target numbering in each of the images are not correlated, but represent the order that each target was detected by the detection algorithm.

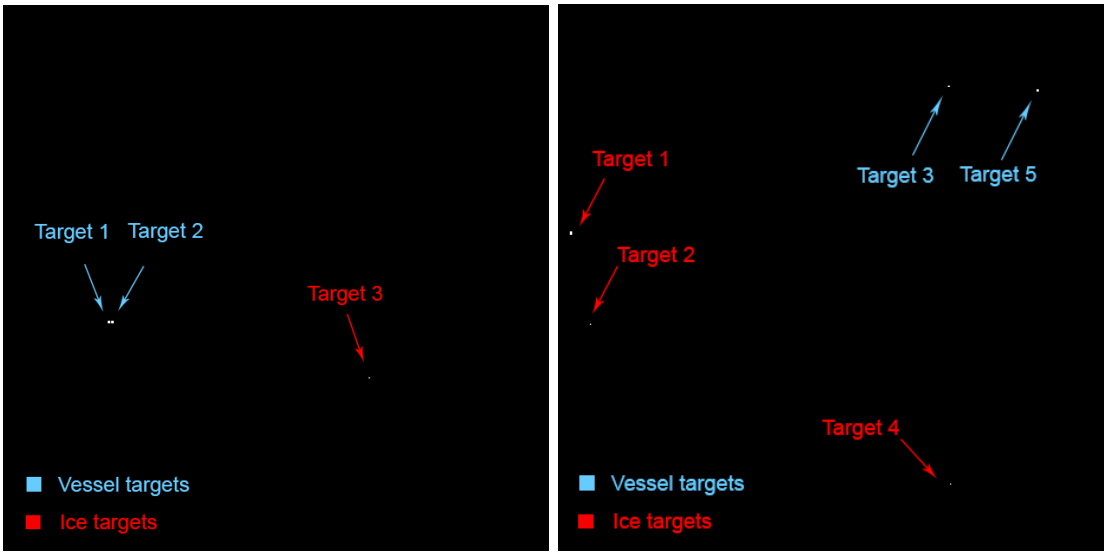


(a) Segmentation of sub-image 2 (b) Segmentation of sub-image 3

Figure 5.8: The segmented versions of the images in Figure 5.7.

The first identified vessel (vessel 1) correspond to target 1 in image 2 and target 5 in image 3. The second identified vessel (vessel 2) correspond to target 2 in image 2 and target 3 in image 3. The remaining targets are assumed to be ice targets, as they were not identified as vessels by the AIS data processing.

Firstly, the classification feature was tested in isolation. The detection was performed as usual, and the coordinates for the centroids were found for all targets in both images. However, the comparison part of the algorithm was skipped, thus not excluding any target matches. Consequently, the speed of travel was calculated for all possible matches. A summary of the classification results can be found in Table 5.7. As described earlier, the classification feature will either classify a match as a vessel, or as inconclusive (the target can be both a vessel and ice). In addition

to showing the classification results, the table also show the actual target types of the two targets being compared.

Table 5.7: Classification results of an isolated classification test. The true matches are outlined in red.

| Target number | | Speed of travel [m/s] | Classification | Actual target types | |
|---|---|---|---|---|---|
| Image 2 | Image 3 | | | Image 2 | Image 3 |
| 1 | 1 | 0.09112 | Ice or vessel | Vessel | Ice |
| 1 | 2 | 0.069899 | Ice or vessel | Vessel | Ice |
| 1 | 3 | 0.25429 | Vessel | Vessel | Vessel |
| 1 | 4 | 0.24927 | Ice or vessel | Vessel | Ice |
| 1 | 5 | 0.3081 | Vessel | Vessel | Vessel |
| 2 | 1 | 0.0932 | Ice or vessel | Vessel | Ice |
| 2 | 2 | 0.07212 | Ice or vessel | Vessel | Ice |
| 2 | 3 | 0.25242 | Vessel | Vessel | Vessel |
| 2 | 4 | 0.24734 | Ice or vessel | Vessel | Ice |
| 2 | 5 | 0.30605 | Vessel | Vessel | Vessel |
| 3 | 1 | 0.26892 | Vessel | Ice | Ice |
| 3 | 2 | 0.24228 | Ice or vessel | Ice | Ice |
| 3 | 3 | 0.1934 | Ice or vessel | Ice | Vessel |
| 3 | 4 | 0.10925 | Ice or vessel | Ice | Ice |
| 3 | 5 | 0.20989 | Ice or vessel | Ice | Vessel |

A correlation can be seen between the matching of actual target vessels and the classification of targets as vessel. However, when using the classification feature in isolation, the speed of travel calculated is only actually valid when the targets being matched are the same target. The only two matches that are known to be true matches are entry five and eight, which are outlined in red in the table. The classification of the remaining entries are not valid. Therefore, the classification feature should only be used on targets successfully matched by the tracking algorithm.

Following this reasoning, the classification feature was tested in combination with the tracking algorithm. The deviation limits used are found in Table 5.8 and a summary of the results are presented in Table 5.9.

Table 5.8: Deviations allowed for the geometrical representation of vessel and ice targets

| Geometrical parameter | Deviations allowed [%] |
|---|---|
| Area | 20 |
| Major axis length | 5 |
| Minor axis length | 10 |
| Perimeter | 5 |

Table 5.9: Results of the classification feature in combination with the tracking algorithm

| Target in image 2 | Target in image 3 | Speed of travel [m/s] | Classification | Actual target types |
|---|---|---|---|---|
| 1 | 5 | 0.3081 | Vessel | Both are vessels, and they are the same vessel |
| 2 | 5 | 0.30605 | Vessel | Both are vessel, but they are not the same vessel |

The tracking algorithm found a match between target 1 in image 2 and target 5 in image 3. These targets both correspond to vessel 1, thus the calculated speed of travel is valid. The algorithm successfully classified this target as a vessel.

The tracking algorithm also found a match between target 2 in image 2 and target 5 in image 3, which is a false matching. These targets correspond to vessel 2 and vessel 1, respectively. The algorithm classified this match as a vessel, however, the calculated speed is not valid since both targets do not correspond to the same vessel.

The algorithm was not able to successfully match vessel 2 in image 2 with vessel 2 in image 3. Compared to the ice targets tracked in Section 5.2, the vessel targets are very small, and only span a few pixels each. Vessel 1 has an area of 9 pixels in

both images, while vessel 2 has an area of 5 pixels in image 2 and 9 pixels in image 3. Enlarged versions of these segments, with pixel grids, are shown in Figure 5.9.

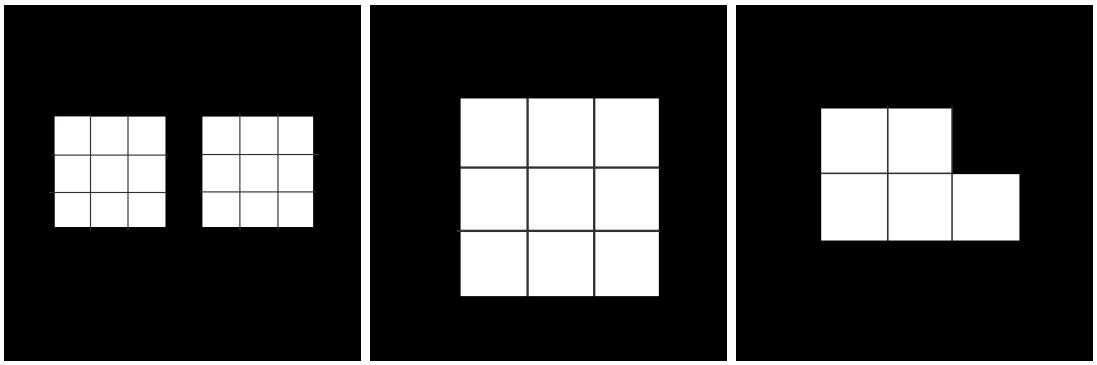

(a) Vessel 1 and 2 in image 2

(b) Vessel 1 in image 3

(c) Vessel 2 in image 3

Figure 5.9: Enlarged images of the segmented vessels with grids illustrating the pixel size.

The difference in area for vessel 2 is due to the satellite not receiving the exact same backscattering from the target in each image. This results in a different brightness return, and thus a different pixel count. In contrary to when tracking large targets, this difference has a huge impact on the shape of the target. This kind of deformation can render the target unrecognizable, thus making the tracking of the target impossible. Another issue which will arise when the targets are very small is that there are too few pixels to form a distinct shape. As is seen in Figure 5.9a, both vessel 1 and vessel 2 are portrayed as a square with 9 equal sized pixels. These two targets are not distinguishable, thus making it impossible to track the targets without false alarms. If the tracking algorithm is insufficient, the classification results are superfluous. Consequently, the classification feature does not work well on targets only spanning a few pixels.

For better classification of vessels of this size, images with a better resolution could be used. Then, the tracking would be improved, rendering more true matches. However, vessels are often very similar in shape, and it will always be difficult to distinguish them from each other.

Another issue with the classification feature is the assumption that all images are at the exact same geographical region. This is rarely the case. For each orbit, the swath of the satellite may vary, the angle may vary, and the position may vary. Therefore, to geographically match all the images, they must be cropped to a common region. This can be difficult, because the positional data follow

longitudal and latitudal lines, and a image crop will not follow these curved lines. In addition, different angles may also prove troublesome when cropping the images.

The best solution to this problem would be to use the positional data from the geolocation of the images in the classification feature. This would involve linking the positional data with the images in MATLAB. The positional data could be stored in a matrix of equal size as the image matrix, so that the a latitude and longitude position for each pixel was available. Then, instead of using the distance formula (4.1.1) to find the distance between the x- and y-coordinates of each centroid, the longitude and latitude for each centroid could be used to calculate the distance. By doing this, the images would not need to be correlated geographically for the distance calculation to work.

In addition, when having the actual position of each target available in MATLAB, it is possible to automatically link targets up with the detected targets from the AIS data. So, when a target is classified as a vessel, it is possible to verify this by checking it up against the AIS-data. Alternatively, the classification feature could be skipped all together, and the AIS data could be used to classify vessels in combination with the tracking algorithm. It would however require some work to enable an automatic synchronization of the AIS data and the images.

# Chapter 6

# Further Discrimination Between Target Types

Since the classification feature of the algorithm was not satisfactory, we wanted to further investigate target discrimination in satellite images. As proved in the previous chapter, it can be hard to distinguish between different targets by just comparing geometrical features. By using the images from the case study presented in Chapter 5, it is in this chapter discussed how multi-polarized imagery and motion patterns can be used to distinguish between ice and vessel targets.

## 6.1 Target Comparison in Different Polarizations

In this section different target types have been identified in dual-polarized RADARSAT-2 ScanSAR images. By comparing these targets in the HH and HV polarized channels, the goal was to detect patterns that can be useful in classification of target types. HH and HV channels corresponds to the satellite radar either having a horizontal transmit and a horizontal receive, or having a horizontal transmit and a vertical receive.

Shown in Figure 6.1 is a section of the area tracked on the Coast of Greenland. The section is shown in three images: a map showing the land and sea segments, a SAR-image in HH polarization, and the same SAR-image in HV polarization.

(a) Screenshot from a Google Maps viewing of the Coast of Greenland.

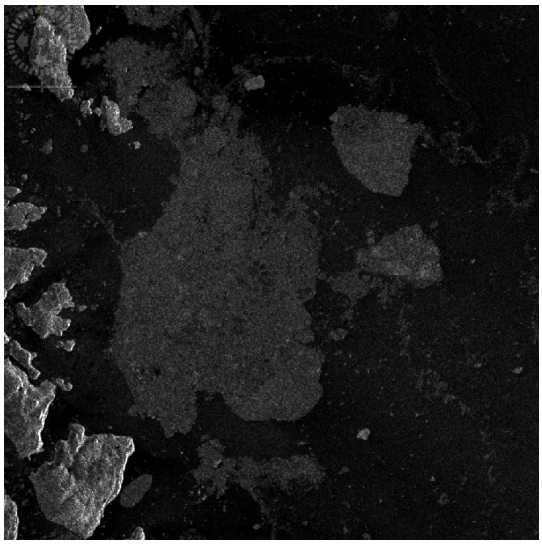

(b) 735 pixel ScanSAR HH data from the same location as in (a).

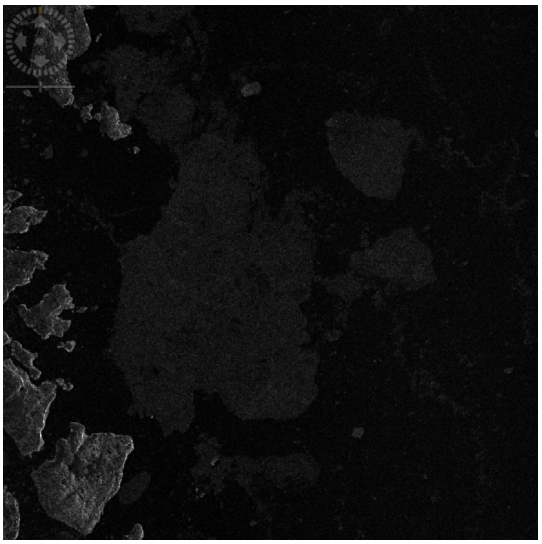

(c) 735 pixel ScanSAR HV data from the same location as in (a).

Figure 6.1: The coast of Greenland, shown in a screenshot from Google Maps (Map data ©2015 Google), and in images with polarization in channel HH and channel HV. RADARSAT-2 Data and Products © MacDondald, Dettwiler and associates LTD. (2013) – All Rights Reserved.

Using the image from Google Maps (Figure 6.1a), it is possible to identify the segments which are land in the satellite images (Figures 6.4a-6.4b). The remaining

segments must therefore be ice segments.

By looking at the satellite images, it is obvious that both land and ice segments have different brightness in the HH and HV channels. To better show this, a horizontal brightness profile was made for each of the satellite images. The profile was taken at 40 % and at 60 % of the image height, as shown in Figure 6.2. The result is seen in Figure 6.3.

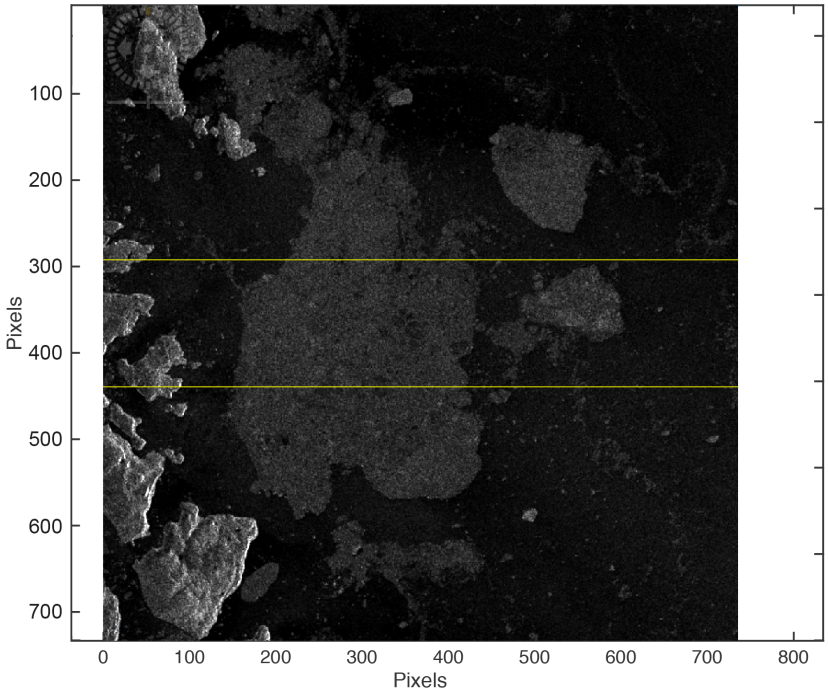


Figure 6.2: Lines showing where the horizontal profiles are taken. The topmost line is at 40 % of the image height and the bottom line is at 60 % of the image height.

The profiles show how the brightness return (given in grayscale levels) varies for different segments in the image. For the profiles taken at 40 % of the image height, it is observed that the land segments have the brightest return, averaging at about 60-80 grayscale levels in the HH channel, and 30-50 in the HV channel. For ice, the return is lower, with an average of 40-60 in the HH channel, and of 15-25 in the the HV channel. The water background has an average return of around 20 in HH and of 10 in HV. Very similar results can be deducted from the profiles taken at 60 % of the image height. The return from the land segments averages to about 70-90 grayscale levels in the HH channel, and to 35-50 in the HV channel. For ice segments and the water background, the average return are the same as in the 40 % profiles. From this it can be deducted that the average brightness return of

land segments is higher than the return from ice. It can also be concluded that both land and ice have a higher return in the HH channel than in the HV channel. Further on, since the different image profiles had very similar results, it follows that the average brightness return is similar across the area of a segment.

Another ice object (Figure 6.4) was analyzed to see if there is a pattern in the brightness return for ice targets. Here it is observed that the average grayscale level return for ice is around 55-65 in HH, while in HV it is 25-35. These are not the same values as in Figure 6.3, however the HV/HH return ratio for each target type is similar. Thus, our conclusion on the brightness return being stronger in HH polarized images than in HV polarized images is reinforced.

Further on, the brightness return of vessel targets were looked into. Figure 6.5 displays sub-images of satellite image 1 and satellite image 3, which show the identified vessels: vessel 1 and vessel 2. These are the same vessel as the ones used in the classification feature in the previous chapter. In image 3 (Figures 6.5a-6.5b), the vessels show a bright and very distinct return in both channels. However, in image 1 (Figures 6.5c-6.5d) the vessel is only distinct in the HH channel. In the HV channel the return is very weak, and not easily distinguishable.

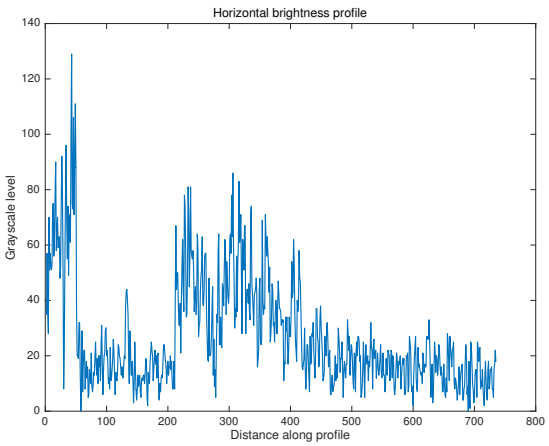


(a) Horizontal brightness with profile at 40 % image height of the HH image in Figure 6.4a.

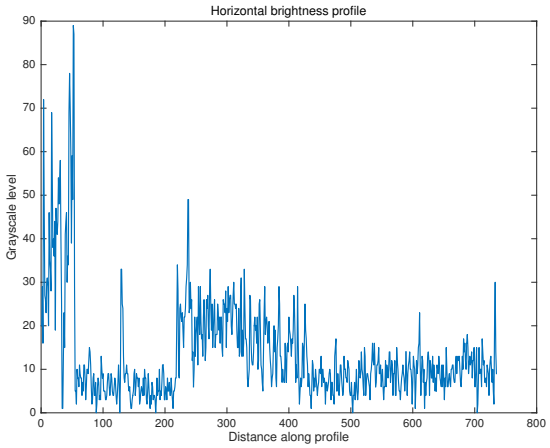


(b) Horizontal brightness with profile at 40 % image height of the HV image in Figure 6.4b.

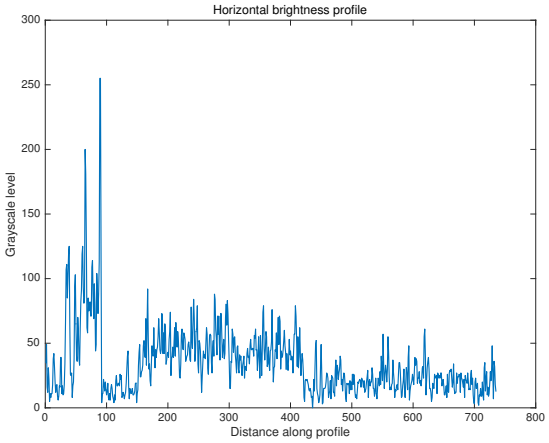


(c) Horizontal brightness with profile at 60 % image height of the HH image in Figure 6.4a.

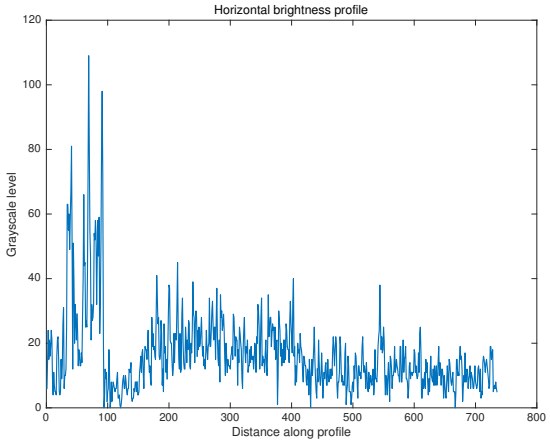


(d) Horizontal brightness with profile at 60 % image height of the HV image in Figure 6.4b.

Figure 6.3: Brightness profile of satellite image with different target elements, with polarization in the HH and HV channels. The distance on the x-axis are in number of pixels.

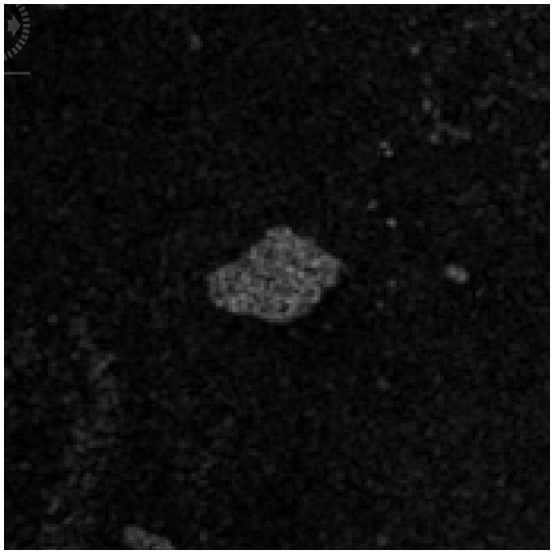

(a) 700 pixel ScanSAR HH data of an ice floe.

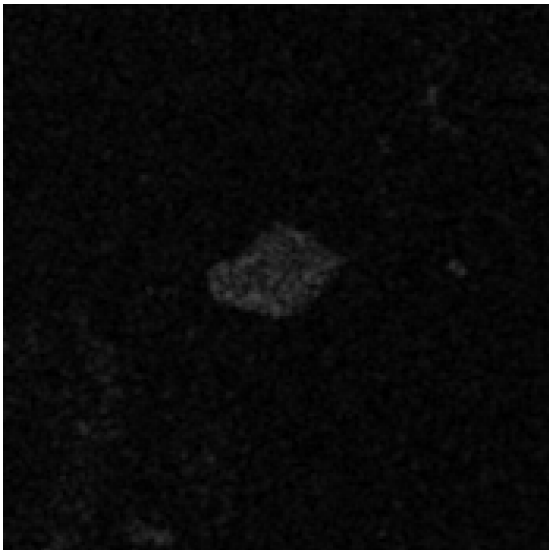

(b) 700 pixel ScanSAR HV data of an ice floe.

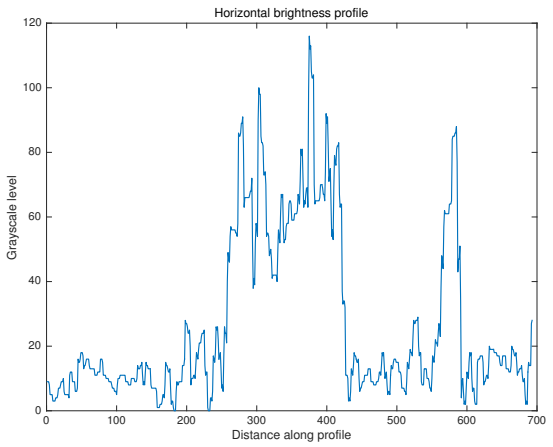


(c) Horizontal brightness profile through the center of Figure 6.4a.

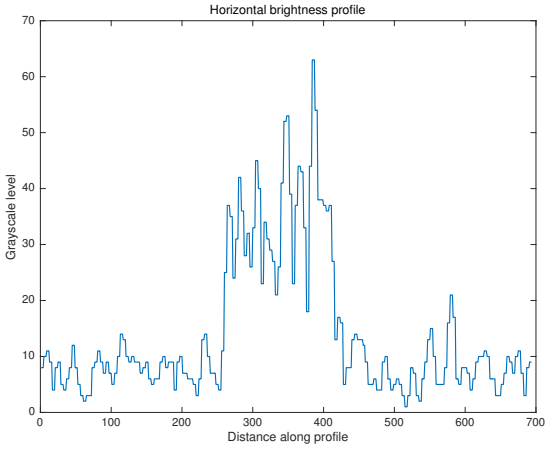


(d) Horizontal brightness profile through the center of Figure 6.4b.

Figure 6.4: Comparison of images of an ice floe with polarization in channel HH and channel HV. RADARSAT-2 Data and Products © MacDondald, Dettwiler and associates LTD. (2013) – All Rights Reserved.

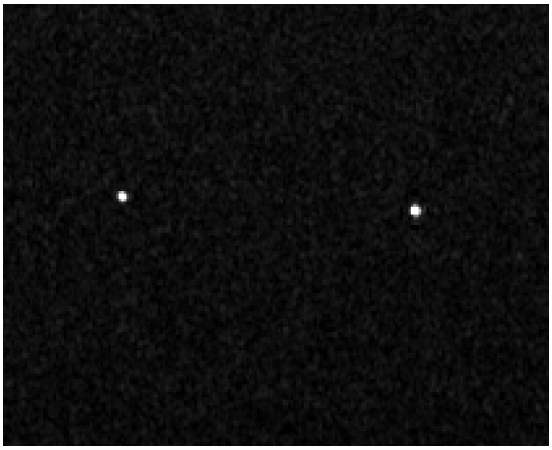

(a) Vessels 1 and 2 in a section of image 3 in HH channel.

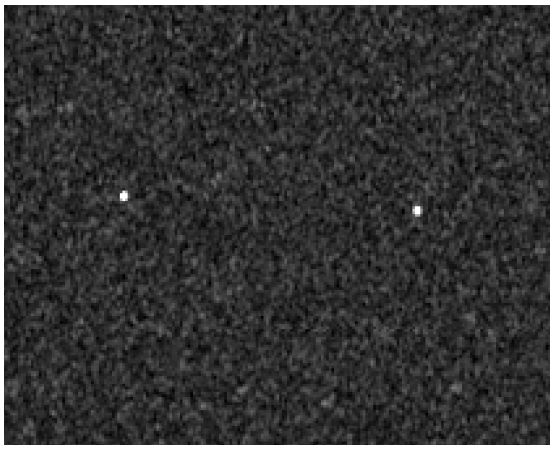

(b) Vessels 1 and 2 in a section of image 3 in HV channel.

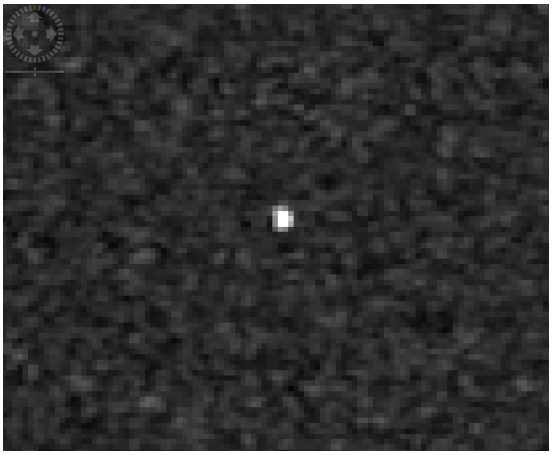

(c) Vessel 1 in a section of image 1 in HH channel.

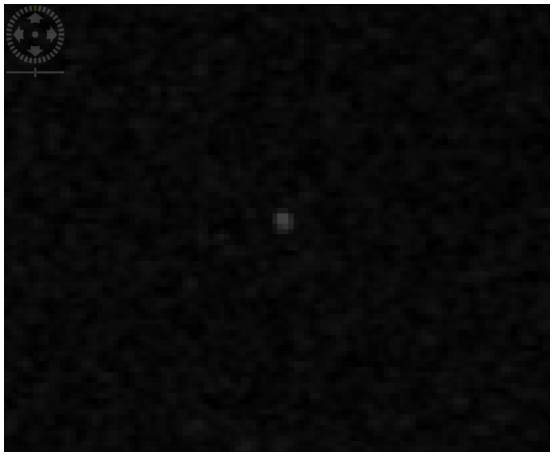

(d) Vessel 1 in a section of image 1 in HV channel.

Figure 6.5: Comparison of images of vessels with polarization in channel HH and channel HV. RADARSAT-2 Data and Products © MacDondald, Dettwiler and associates LTD. (2013) – All Rights Reserved.

To see if it was possible to find a pattern, 9 ice targets and 8 vessel targets were randomly chosen, and the HV/HH area ratio was calculated for each target. This was done by finding a local brightness threshold for segmentation, and then applying methods from the detection and tracking algorithm to find the area in pixels for each target. This was done in both the HH and HV channels for each target, thus making it possible to find the HV/HH area ratio. The result is presented in Figure 6.6.

The HH and HV target area values for vessels and ice are significantly different.

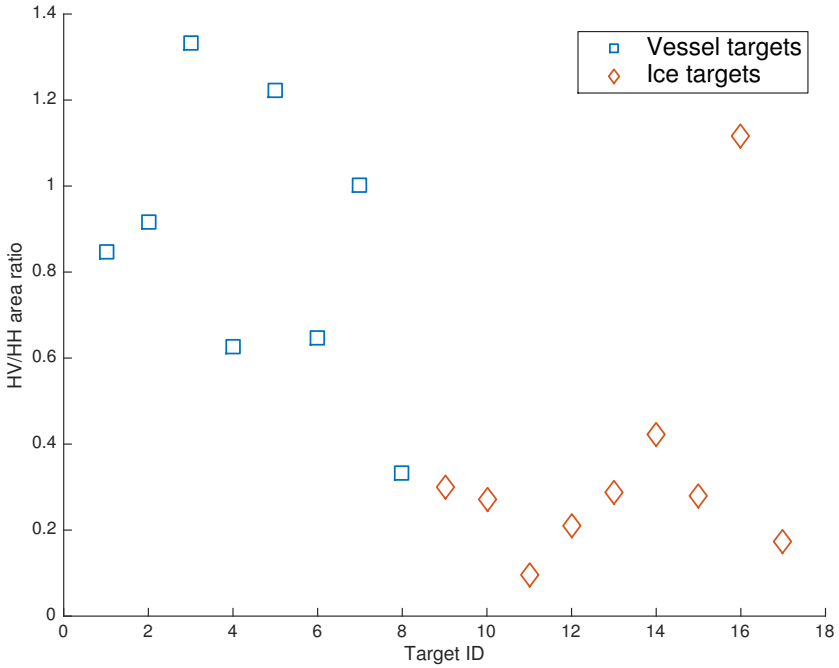


Figure 6.6: HV/HH area ratio for vessel and ice targets.

The HV/HH area ratios for vessel targets are scattered between the values 0.4 and 1.4. There is no pattern that shows the targets having a more significant brightness return in either channels. However, since the measurements are quite evenly distributed, the average HV/HH area ratio is close to 1. Thus, the conclusion is that there is a high correlation between HH and HV areas for vessel. For the ice targets, however, the correlation is low. The majority of the ice targets have twice as large HH area than HV area, which results in most of the them having a ratio under 0.4.

By analyzing all targets in a satellite image and comparing the HV/HH area ratio, it is possible to use this information as a method for target discrimination. The criteria should be that all targets with a low ratio (in this case $< 0.4$) are ice targets. However, since the ratio for vessel targets fluctuates, the accuracy would be compromised by occasional vessel targets having a low ratio. In addition, there would be some incidents of ice targets having a higher ratio. In this scenario, using the value 0.4 as a separator between ratios for ice and vessel targets would result in a target discrimination feature with 82 % accuracy.

By applying dual-polarized imagery to the detection and tracking algorithm presented by this thesis, this methodology can be used to improve the classification capabilities of the algorithm.

Even though this method could be used as an indicative discriminator, this test does not support the results from the same type of multi-polarization tests done in Howell et al. (2004). There, the majority of the ice targets are not even detected in the HV channel, resulting in a HV/HH ratio equal to zero, which makes the discrimination feature much more accurate. The fact that this thesis presents different results than Howell et al. (2004), shows that in addition to comparing polarization channels, test should be done where multi-polarized images from different types of satellites (RADARSAT, ENVISAT etc.) were compared.

## 6.2 Motion Patterns of Targets

In this section, the aim was to compare the motion patterns of human-controlled vessels and free-floating ice to see if this could be used to distinguish between vessel and ice targets.

In Section 6.2.1 it is shown how positional data from AIS data can be used to find the motion patterns of vessel. By using this methodology, a check on the validity of the chosen speed limit in the classification feature is done (Section 6.2.2). Further on, in Section 6.2.3 it is discussed how motion patterns of free-floating ice targets in the case study can be found from observing the East Greenland Current. Lastly, a comparison of the motion of vessel and ice targets on the Greenland East Coast is shown in Section 6.2.4.

### 6.2.1 Vessel Motion

When looking through the acquired AIS data for the vessels identified in the area of interest, it became apparent that the recorded values for speed were not realistic. In some cases, the speed recorded was over 100 knots, which is unlikely. Therefore, an estimation of the speed for each vessel was necessary. To do this, the Haversine formula was used for calculating the distance traveled between each known position of the vessel.

The Haversine formula calculates the great-circle distance between two points. This equals the shortest distance over the earth's surface, when assuming a flat surface.

The formula is customarily written in terms of the Haversine function, but it can

also be formulated in terms of the sine and cosine functions:

$$a = \sin^{(}\frac{\Delta\phi}{2}) + \cos(\phi_1)\cos(\phi_2)\sin^2(\frac{\Delta\lambda}{2}) \tag{6.2.1}$$

$$c = 2atan2(\sqrt{a}, \sqrt{(1-a)}) \tag{6.2.2}$$

where $\phi$ is latitude and $\lambda$ is longitude, both in radians. $R$ is the earth's radius (mean radius = 6.371 km). $atan2(x, y)$ is a function in MATLAB which returns the four-quadrant inverse tangent of x and y.

Using the calculated parameters $c$, it is then possible to calculate the traveled distance

$$d = Rc \tag{6.2.3}$$

Now, using the time $t$ and the distance traveled $d$, the estimated average speed of the vessel is given by:

$$v = \frac{d}{t} \tag{6.2.4}$$

### 6.2.2 The Validity of the Speed Limit for Target Discrimination

To check the validity of the chosen speed limit in the classification feature of the detection and tracking algorithm, the average speed of all AIS detected vessels were found. The goal for this was to see how many of the vessels that actually had an average speed of travel above 0.25 $m/s$ between two sequential images. The results are presented in Table 6.1. Since the average speed is based on the distance a target has traveled between two images, only vessels that appear in several images are used. The positional data used for calculating the speed values are listed in Appendix C.2.

Table 6.1: The average speed [m/s] of vessels between pairs of images. Values below 0.25 are in bold.

| Image pairing | Vessel number | | |
|---|---|---|---|
| | 1 | 2 | 4 |
| 1-2 | 0.9846 | 1.0373 | - |
| 2-3 | 0.3317 | 0.2758 | 3.5242 |
| 3-4 | 0.8341 | 0.7786 | 2.0871 |
| 4-5 | 1.6761 | 1.6747 | 0.5471 |
| 5-6 | - | - | **0.0003** |
| 5-7 | 0.7784 | 0.7738 | - |
| 6-7 | - | - | **-0.0002** |
| 7-9 | 1.3287 | 1.3271 | **0.1811** |
| 9-10 | 1.8710 | 1.8724 | 1.5863 |
| 10-11 | 1.0979 | 1.2944 | 0.2737 |
| 11-12 | 0.6725 | 0.5336 | 0.6706 |
| 12-13 | 0.4691 | 0.4740 | **0.2178** |
| 13-15 | 0.8530 | 0.8530 | 2.2275 |

Of all the calculated speed values, only four values are below 0.25 $m/s$. These are marked in bold in the table. If classifying all targets with a speed higher than 0.25 $m/s$ as vessels, this case would give a classification accuracy of 88 percent. In the previous chapter it was concluded that if a target had a speed higher than 0.25 $m/s$, then it was most likely a vessel. However, if the speed was lower than 0.25 $m/s$ a decision could not be made if the target was a vessel or if it was ice. When taking these quantitative results into account, it can be assumed that targets with a low speed probably are ice targets. Hence, by using the speed limit as a separator between ice and vessel targets, it is possible to classify both vessels and ice targets, while still maintaining a high percentage of accuracy.

### 6.2.3 Ice Motion due to the East Greenland Current

Ice motion is largely determined by currents. This is especially true for ice floes and icebergs surrounded by sea ice. For icebergs in open water, the wave drift may become the most important forcing. However, for the case study in this thesis, the ice targets are in close proximity and consist mainly of pack ice and ice floes. Consequently, the ice motion follows the motion of currents on the Greenland East Coast.

The East Greenland Current (EGC) flows southward along the eastern coast of Greenland. It follows the coast all the way from Fram Strait (79°N) and down to Cape Farewell (60°N).

Figure 6.7 shows a representation of the current, found by the US Coast Guard's Mariano Global Surface Velocity Analysis (Mariano et al., 2015).

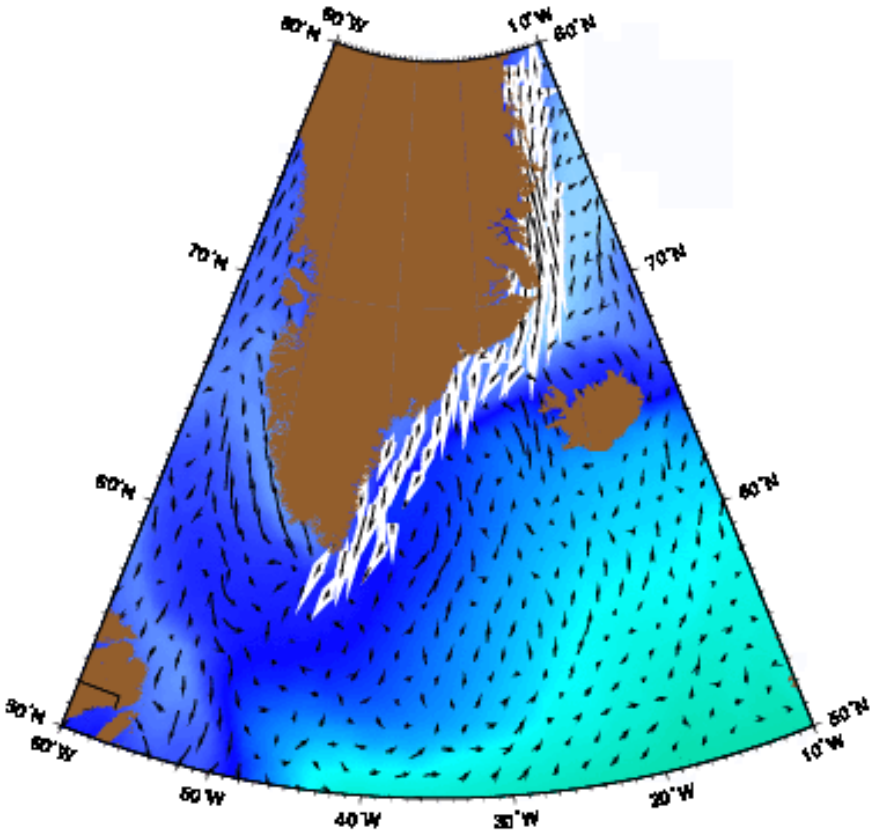


Figure 6.7: The East Greenland Current as represented by the Mariano Global Surface Velocity Analysis (Gyory et al., 2015).

As the only major southward flowing current in the Greenland Sea, the EGC transports > 90 % of the ice exported from the Arctic Ocean (Woodgate et al., 1999).

There have been several attempts to measure the current speed of the EGC. Aagaard and Coachman (1968) found that typical current speeds were 10 to 15 $cm\ s^{-1}$. Other studies have shown that the mean current speed is between 8 and 10 $cm\ s^{-1}$ (Foldvik et al., 1988). The maximum speeds were measured at 20-30 $cm\ s^{-1}$ by Bersch (1995). It was also showed that the current is typically faster on the eastern edge of the current, than further inshore.

With its high surface current velocities, the EGC carries sea ice and Polar Water out of the Arctic Ocean through Fram Strait. By assuming that the motion of the ice follows the current, an upper speed limit for ice targets at 0.25 $m\ s^{-1}$ (or 25 $cm\ s^{-1}$) is a good estimate. The ice may reach a higher maximum speed, however since measurements from the satellite images are intermittent, the average speed will probably be below this limit.

### 6.2.4 Comparison of Vessel and Ice Motion

To illustrate the difference in motion of free-floating ice targets and human controlled vessel targets, the motion of a few targets were mapped.

The position of three different pieces of ice were manually tracked in the 15 satellite images from the East Coast of Greenland. The resulting trails are drawn in the Google Earth map in Figure 6.8.

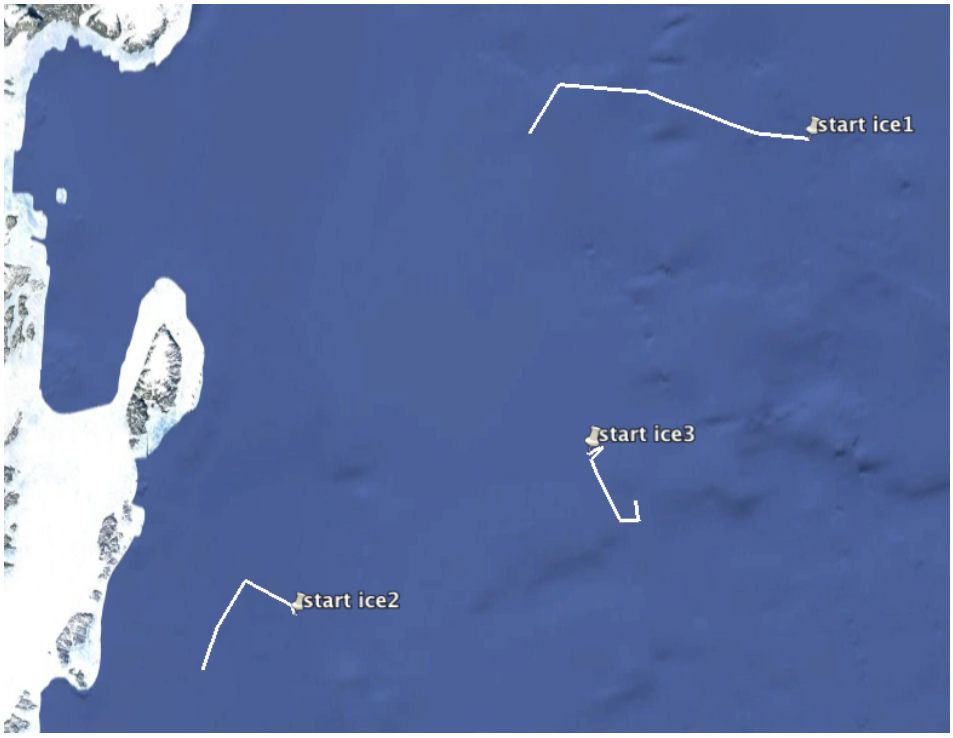


Figure 6.8: The tracked motion of ice targets over the course of 11 days. The pins show the start points.

For comparison, the trajectories of two vessels are drawn in the Google Earth maps in Figure 6.9 and Figure 6.10.

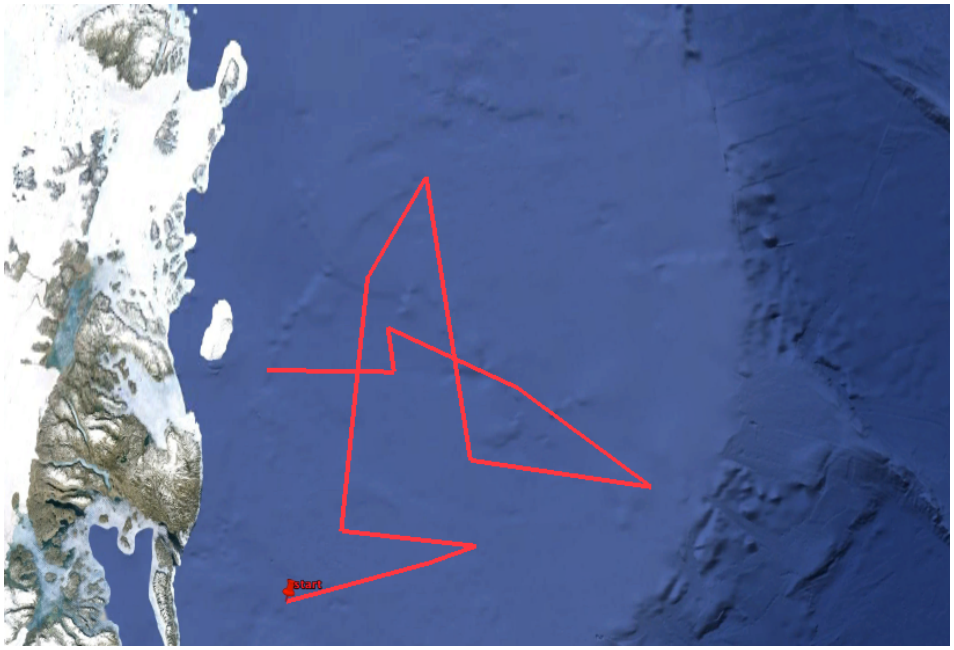


Figure 6.9: The tracked motion of vessel 1 over the course of 11 days. The pin shows the start point.

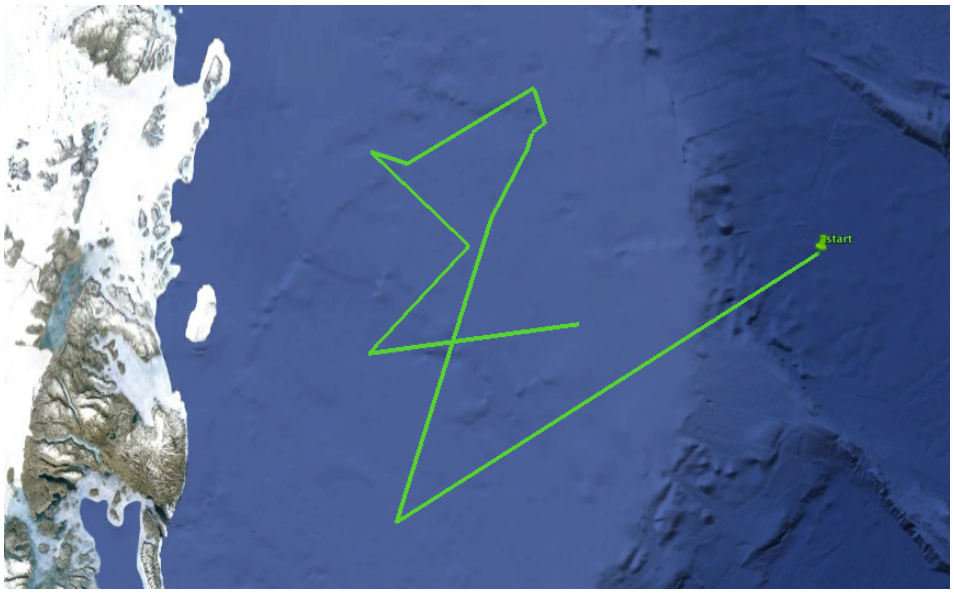


Figure 6.10: The tracked motion of vessel 4 over the course of 10 days. The pin shows the start point.

The distance traveled is much longer for the vessels than for the pieces of ice. In

addition, the motion patterns are very different for the two target types. For the vessels no distinct patterns are observed. This matches the statement of vessels being human-controlled targets. For the ice targets, it looks like the ice drifts either west (towards land), or south. When comparing this with the EGC in Figure 6.7, the motion of the tracked ice targets correlates with the EGC.

In this scenario only three ice targets have been tracked, over a relatively short time period. This is not sufficient to conclude that ice targets will always follow the current. However, the fact that the motion of the tracked targets correlates with the EGC, gives us an indication that ice targets will follow the current.

# Chapter 7

# A Model for Iceberg Drift Forecasting

In the previous chapter, observations showed that ice targets move in accordance with the current. Thus, by overlaying satellite images with current fields, it is possible to approximate the drift of an ice target.

This chapter presents a dynamic model made for estimating the drift of an iceberg. Current fields are used as an input in the model, estimating the position and velocity of the ice target. The model is the same as was presented in the author's project thesis (Larssen, 2014).

Initially, an objective of the thesis was to simulate the model by using the case study from the Greenland East Coast. However, sufficient current data were not available. Therefore, in this chapter, a simulation using synthetic data is performed. Ergo, the model is not correlated with the satellite images from the case study.

## 7.1 Simulation Setup

This is a model which uses weather data such as current, wind and waves as an input and utilizes this to predict the motion of the ice. The model is the same as the model presented in Eik (2009*b*), and is explained in Section 2.3.5.

To be able to make a model, some values had to be assumed for the wind, current, and wave parameters. The assumed values and other parameters used is given in Table 7.1.

Table 7.1: Parameters used in the dynamic model

| Description | Parameter | Value | Reference |
|---|---|---|---|
| Air density | $\rho_a$ | 1.225 $[km/m^3]$ | |
| Water density | $\rho_w$ | 1027 $[km/m^3]$ | |
| Air drag coefficient | $C_a$ | 1.3 [-] | Bigg et al. (1997) |
| Water drag coefficient | $C_w$ | 0.9 [-] | Bigg et al. (1997) |
| Sea ice density | $\rho_{si}$ | 900 $[km/m^3]$ | |
| Block coefficient | $C_b$ | 0.45 [-] | Kubat et al. (2005) |
| Iceberg waterline length | $L_i$ | 20 [m] | |
| Cross-section above water | $A_a$ | 10 $[m^2]$ | |
| Cross-section below water | $A_w$ | 71 $[m^2]$ | |
| Iceberg length | $L$ | 100 [m] | |
| Gravity | $g$ | 9.81 $[m/s^2]$ | |
| Wind velocity | $V_a$ | 10 $[m/s]$ | |
| Wind direction, North-East | $\theta_a$ | $\frac{\pi}{4}$ (45 degrees) | |
| The residual current velocity | $V_{res}$ | 1 $[cm/s]$ | |
| The tidal current velocity | $V_{tc}$ | 2 $[cm/s]$ | |
| The current velocity | $V_w$ | $V_{res} + V_{tc}$ | |
| Current direction | $\theta_c$ | $\frac{\pi}{2}$ (90 degrees) | |
| Significant wave height | $H_s$ | 2 $[m]$ | Faltinsen (1990) |
| Wave amplitude | $a$ | $0.5H_s$ | |

On state space form the model is given as the nonlinear system

$$\dot{\mathbf{x}} = \mathbf{f}(\mathbf{x}) + B\mathbf{u}, \tag{7.1.1}$$

shown as a block diagram from Simulink in Figure 7.1.

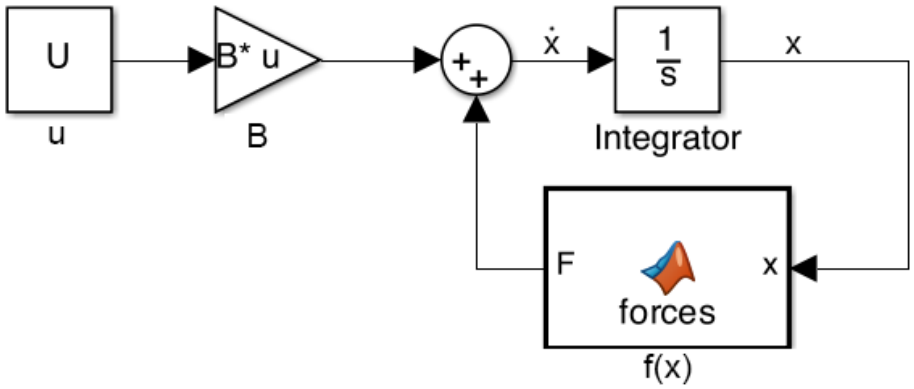


Figure 7.1: Block diagram of the dynamic model in Simulink.

The states of the iceberg model are

$$\mathbf{x} = \begin{bmatrix} x & y & u & v & a_x & a_y & c_x & c_y & w_x & w_y \end{bmatrix}^T, \tag{7.1.2}$$

with $x$ and $y$ as the position in north-south and east-west direction, respectively, and with $u$ and $v$ as the iceberg velocities. The other states are the air (wind), current velocities, and wave elevation, also decomposed in north-south and east-west direction, respectively.

The input used is

$$\mathbf{u} = \begin{bmatrix} 10 & 10 & 10 & 10 & 10 \end{bmatrix}^T \tag{7.1.3}$$

and the $B$ matrix is given as

$$B = \begin{bmatrix} 0 & 0 & 0 & 0 & 0 & 0 \\ 0 & 0 & 0 & 0 & 0 & 0 \\ 0 & 0 & 0 & 0 & 0 & 0 \\ 0 & 0 & 0 & 0 & 0 & 0 \\ 1 & 0 & 0 & 0 & 0 & 0 \\ 0 & 1 & 0 & 0 & 0 & 0 \\ 0 & 0 & 1 & 0 & 0 & 0 \\ 0 & 0 & 0 & 1 & 0 & 0 \\ 0 & 0 & 0 & 0 & 1 & 0 \\ 0 & 0 & 0 & 0 & 0 & 1 \end{bmatrix} \tag{7.1.4}$$

The nonlinear function $f(x)$ contains the equations described in Section 2.3.5, and has the output

$$\mathbf{f}(\mathbf{x}) = \begin{bmatrix} u & v & f_x & f_y & a_x & a_y & c_x & c_y & w_x & w_y \end{bmatrix}^T \tag{7.1.5}$$

where $f_x$ and $f_y$ are the accelerations of the iceberg calculated by the momentum balance, in north-south and east-west direction, respectively.

For simplicity, the model assume that the iceberg is on open water.

## 7.2 Simulation Results

Figures 7.2 and 7.3 show the resulting states, with a time series of 100 seconds.

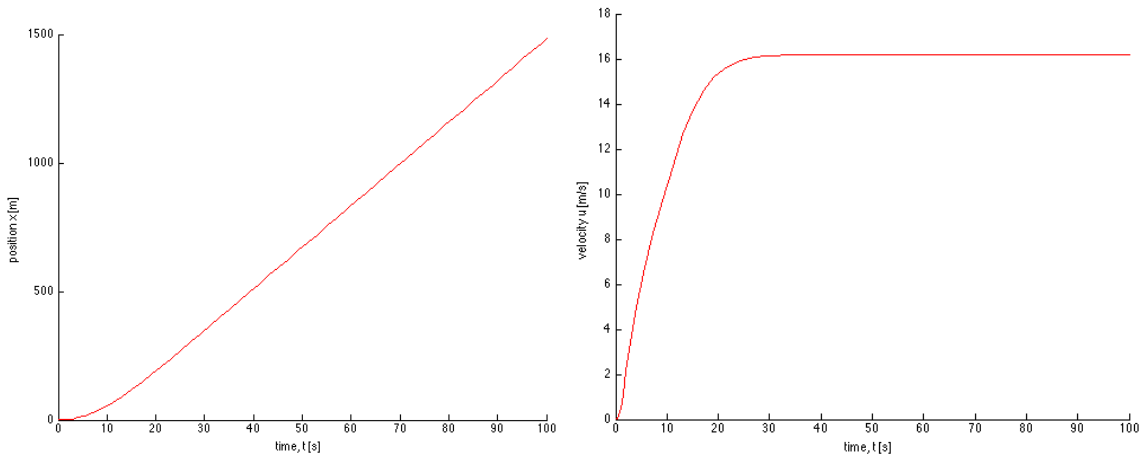


(a) The position (b) The velocity

Figure 7.2: Position and velocity of the iceberg in north-south direction. The results in east- direction are identical.

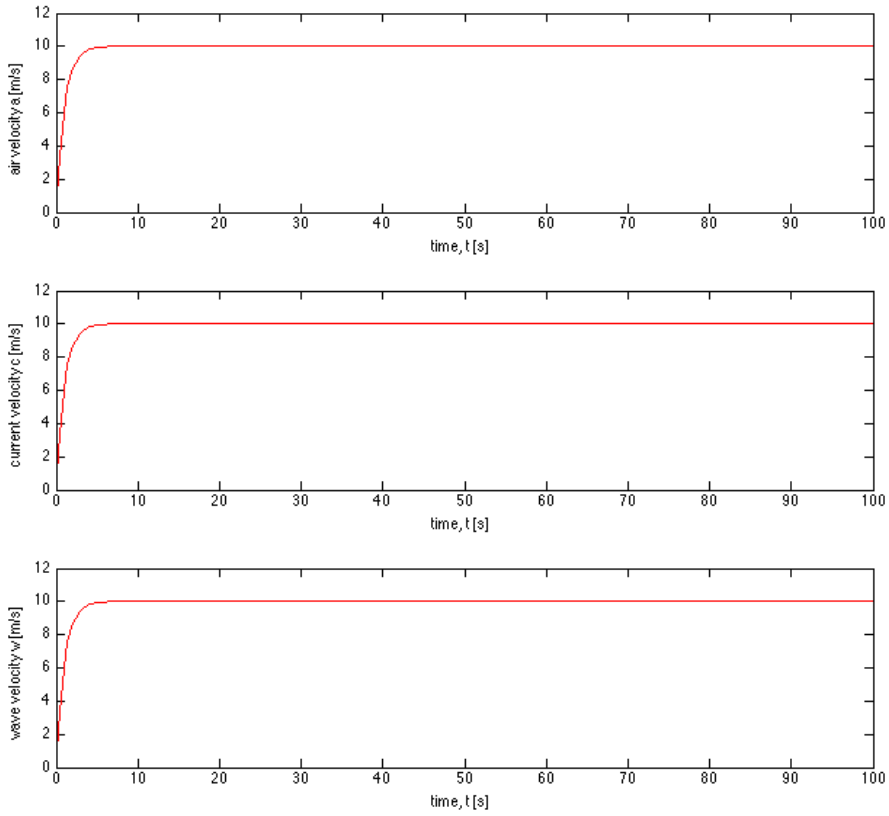


Figure 7.3: The wind and current velocity and wave elevation in north-south direction. The results in east-west direction are identical.

The time window is very short, and the input $U$ is extremely high, making the iceberg move unrealistically fast. This is done only to illustrate how the model works, and to show that ice velocity converges to a constant value after a short period of time (Figure 7.2b).

Lower input values would give the same convergence rate in wind and current velocity, and wave elevation; however, the convergence rate for the velocity varies according to the input. This is illustrated in figures 7.4 and 7.5 where the input

$$U = [1\ 1\ 1\ 1\ 1\ 1]^T \tag{7.2.1}$$

have been used.

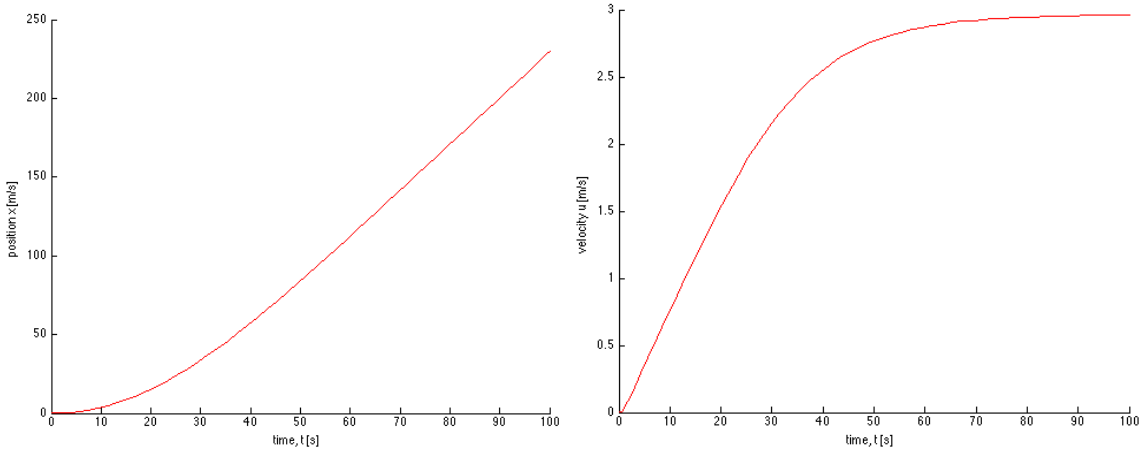


(a) The position (b) The velocity

Figure 7.4: Position and velocity of the iceberg in north-south direction for a decreased input $U$

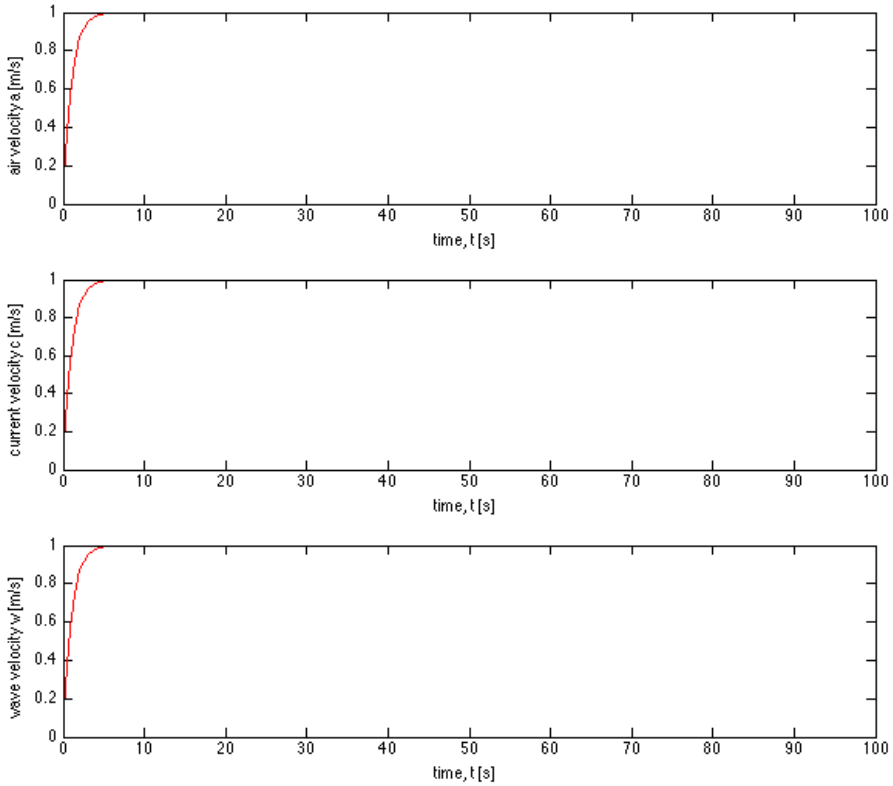


Figure 7.5: The wind, current and wave velocity in north-south direction for a decreased input $U$

### 7.2.1 Model uncertainties

The model relies both on the ability to describe physical actions from the environment on the iceberg and the accuracy of the applied variables (wind, waves and currents). Thus, in a real case scenario, it would be more difficult to get an accurate modeling of the iceberg drift. Also, there are some uncertainties in the model. For instance, it is assumed that the iceberg is in open water (less than 15 % ice concentration), thus, forces from surrounding sea ice are not included. In a case where the iceberg is surrounded by sea ice, these additional forces would need to be included. It is, however, important to note that forces from waves and sea ice are not allowed to act simultaneously. So, for a higher ice concentration, where forces from sea ice are present, the wave drift forces are omitted. In addition, the model assumes an iceberg shape that have the same added mass in both directions, which would also be different in a real case scenario.

One of the forces working on the iceberg, is the mean wave drift force, which depends on the icebergs capability to generate waves. In the calculation, the wavelengths $\lambda$ are assumed to be small compared to the iceberg. This means that the model would be inaccurate for small icebergs in large waves, where the the condition $\lambda << L$ is not fulfilled. Another assumption done is that the iceberg walls are vertical, so that all the encountered waves are reflected. Thus, an iceberg that consist of walls that are not completely vertical, would not be suitable for this model. These uncertainties show that making an iceberg drift model that applies to all kinds of icebergs, in all kinds of water, would be very complex. The best solution would be to use statistics to find common iceberg shapes, and weather conditions in specific regions. That way, models can be tailored for specific regions, as the model used in this thesis is. Another solution would also be to multiply the wave drift force with a wave drift coefficient, $C_w$, which will depend on ratios between parameters such as iceberg characteristic length, draft, wave length and water depth (Isaacson, 1988). The coefficient will be a replacement for the unfulfilled assumptions.

The deterioration of icebergs embedded in sea ice is limited and generally less than 25 cm/day, however, the reduction in length of icebergs drifting in open waters may be several meters per day (Eik, 2009*a*). This is because the wave erosion process is the main contribution to iceberg deterioration, causing more than 70 % of the mass reduction. Consequently, for regions with open waters and high wave drift forces, the deterioration should be taken into account in the drift model. This have not been taken into consideration in this thesis, and is another cause for uncertainties in the model.

## 7.3 Estimation of Iceberg Velocity using Kalman Filtering

To be able to estimate unknown states of the system, a Kalman filter have been implemented. This can be used to estimate the velocity of the iceberg. The estimation have been simulated for both continuous and intermittent observations.

### 7.3.1 Continuous Observations

The Kalman filter is made using the equations presented in Section 2.3.6. To test a case where not all states are being measured, the measurements are set to

$$y = [x \quad u \quad a_x \quad a_y \quad c_x \quad c_y \quad w_x \quad w_y], \tag{7.3.1}$$

which means all states, except the velocities $u$ and $v$, are being measured. For the input to the model, the input in (7.1.3) have been used.

The added measurement noise has a variance of one on each measurement, thus giving us

$$R = diag([1\ 1\ 1\ 1\ 1\ 1\ 1\ 1]). \tag{7.3.2}$$

The $Q$ matrix is found from tuning each diagonal value to fit with the model. The resulting values are

$$Q = diag([430\ 430\ 2\ 2\ 0.0008\ 0.0008\ 0.0008\ 0.0008\ 0.001\ 0.001]), \tag{7.3.3}$$

and the estimation results in north-south direction are in the figures 7.6-7.8.

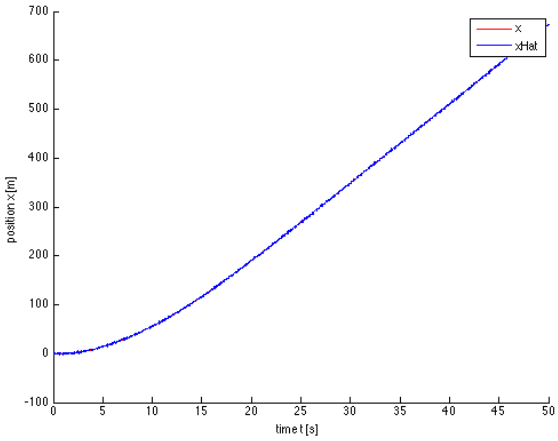


(a) The modeled and the estimated position of the iceberg in north-south direction.

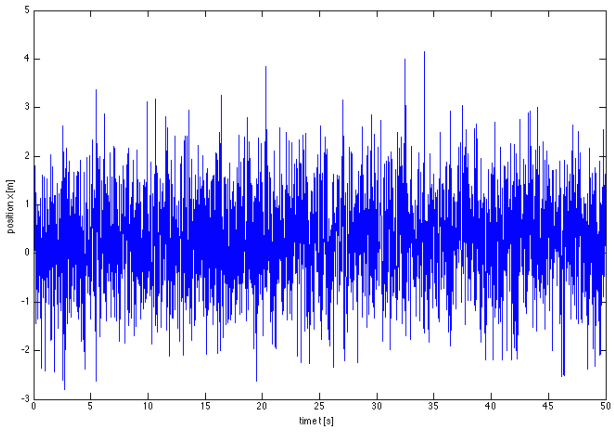


(b) The error $e = \hat{x} - x$ of the estimated position of the iceberg in north-south direction.

Figure 7.6: The modeled and the estimated position of the iceberg and the estimation error.

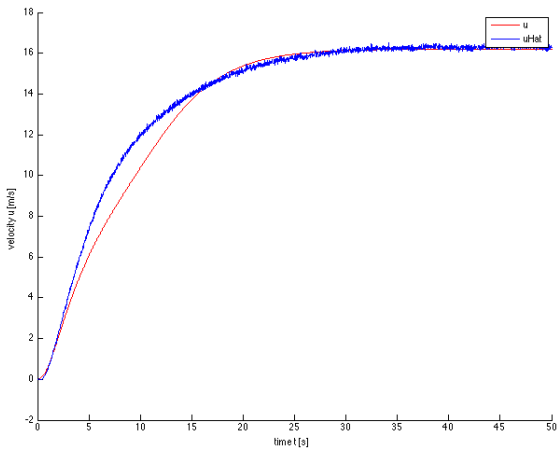


(a) The modeled and the estimated velocity of the iceberg in north-south direction.

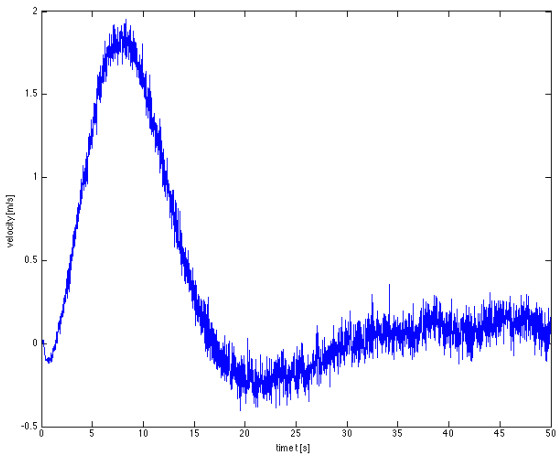


(b) The error $e = \hat{u} - u$ of the estimated velocity of the iceberg in north-south direction.

Figure 7.7: The modeled and the estimated velocity of the iceberg and the estimation error.

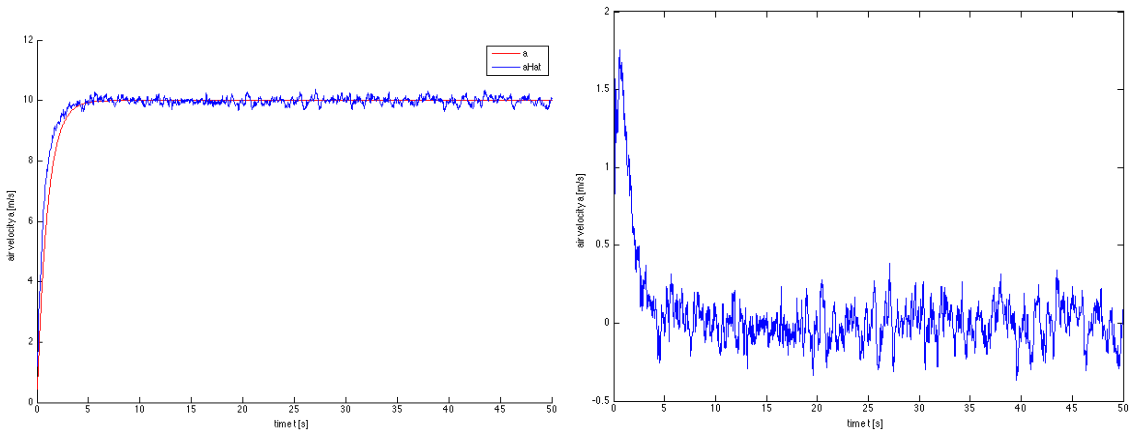


(a) The modeled and the estimated wind velocity of the iceberg in north-south direction.

(b) The error $e = \hat{a} - a$ of the estimated wind velocity of the iceberg in north-south direction.

Figure 7.8: The modeled and the estimated wind velocity of the iceberg and the estimation error.

The current velocity and wave elevation estimations are not included because their plots are identical to the wind velocity's plot.

For the estimated position of the iceberg in Figure 7.6a it looks as though the estimation is good. However, the error $e$ between the estimated and the actual state (Figure 7.6b) shows that the estimation gives a rapid error between $-3$ and 4. This is measurement noise, and has a range of 7 meters, which is quite large. However, compared to the rate of the movement (nearly 700 meters after 50 seconds) this deviation is small. In a real case, where the movement would be largely decreased, the error from the noise would be decreased accordingly.

When estimating the velocity of the iceberg (Figure 7.7), the Kalman filter was not tuned well enough for the estimation to follow the actual state perfectly. The estimation overshoots, which results in a big error of almost 2 $m/s$ after around 8 seconds. However, the estimation does converge after a short amount of time, and the noise is not too significant.

For the estimation of the wind velocity (Figure 7.8), there is also a case of overshoot in the estimation, as in the iceberg velocity estimation. In this case, however, the estimation does converge more quickly. The downfall is that there are more noise. This is not ideal, because too much noise can render the state unstable. To improve the estimation, a bias force could be included as a state in the model. This should be able to account for deviations and model uncertainties.

The choice of input in this model makes the estimation very artificial and unrealistic. A significantly lower input, could change the system dynamics, thus changing the whole model and the way the estimation is tuned. This implementation does, however, show that it is possible to estimate the velocity of the iceberg, even though it is not measured. This is valuable information.

### 7.3.2 Intermittent Observations

When using a Kalman filter (KF) for estimation, images from satellites and radars can be used as measurements. However, image based observations are not continuous. To see how this affects the estimation, a KF with intermittent observations have been implemented.

For this purpose, a binary signal has been added as an input to the Kalman filter. The ones tell the KF that there have been a measurement, and that the states can be updated. The zeros tell the KF that there are no measurements, and that it should use the same state as in the last iteration. A normal distribution have been used to simulate the binary signal, and 6 different scenarios have been used to illustrate the rate of measurement:

- Scenario 1 : 97.7 % measurements
- Scenario 2 : 84.1 % measurements
- Scenario 3 : 50 % measurements
- Scenario 4 : 15.9 % measurements
- Scenario 5 : 2.2 % measurements
- Scenario 6 : 0.1 % measurements.

These scenarios correspond to areas of the graph in intervals between $-3$ and 3 in Figure 7.9. Starting at $-3$ in the first scenario, each scenario step one standard deviation, $\sigma = 1$, to the right on the horizontal axis, making the total of measurements allowed smaller accordingly.

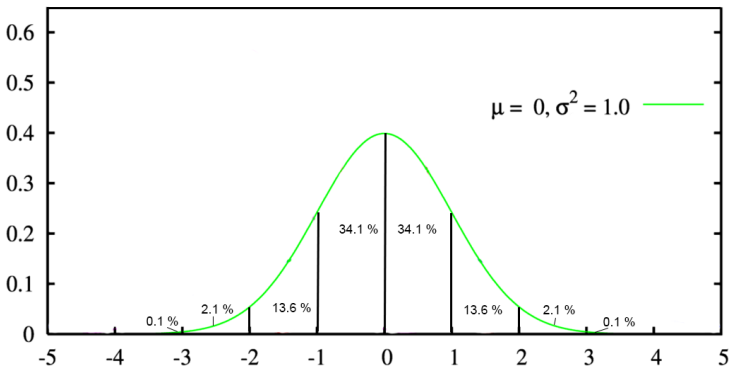


Figure 7.9: A normal distribution, with zero mean and a variance of one, and the areas for each standard deviation.

The plots in Figure 7.10 show the resulting estimations of the iceberg velocity $\hat{u}$ compared to the model values $u$ in each case.

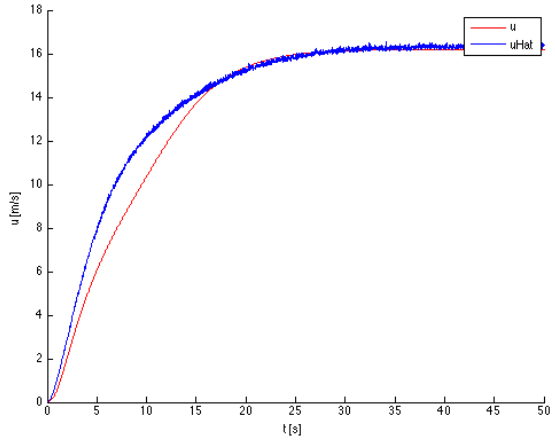


(a) Scenario 1: The percentage of real measurements is 92.7%

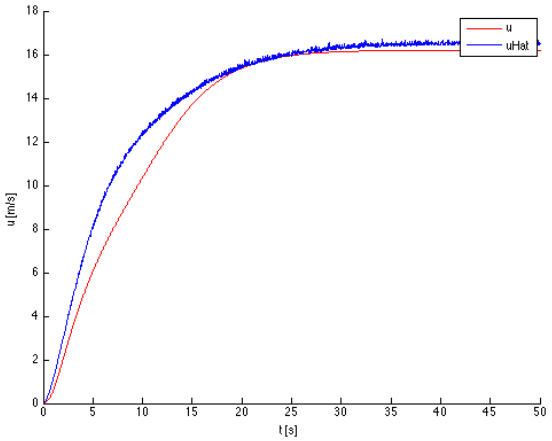


(b) Scenario 2: The percentage of real measurements is 84.1%

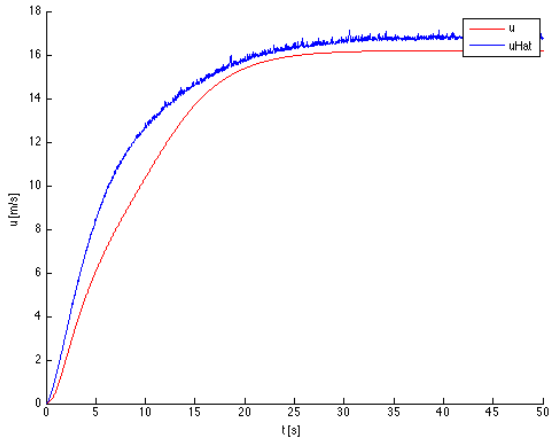


(c) Scenario 3: The percentage of real measurements is 50%

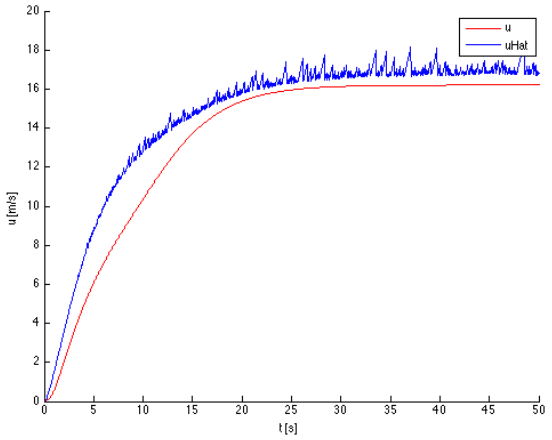


(d) Scenario 4: The percentage of real measurements is 15.9%

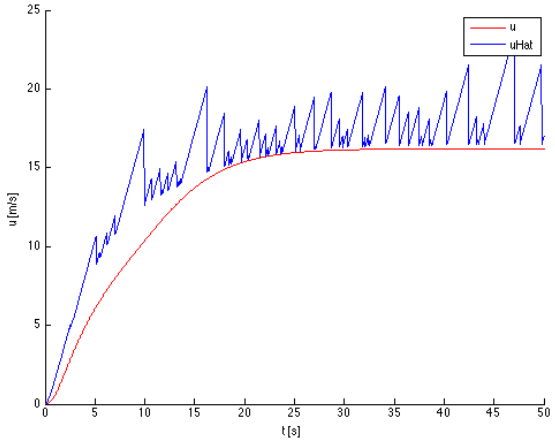


(e) Scenario 5: The percentage of real measurements is 2.2%

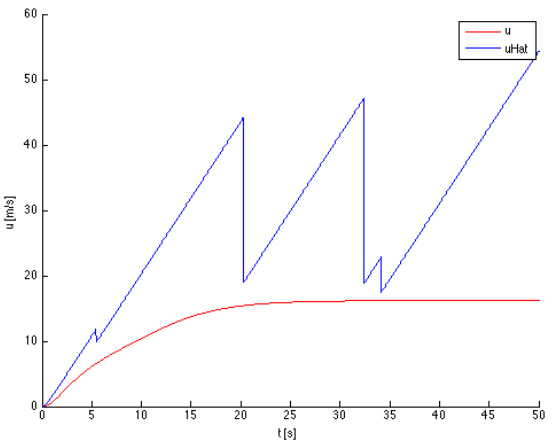


(f) Scenario 6: The percentage of real measurements is 0.1%

Figure 7.10: Kalman filtering with intermittent observations

In scenarios 1 and 2, the rate of measurement is high, and the estimation is very close to the estimation found when using continuous observations. In Scenario 2, however, the estimated velocity does converge to a value slightly higher than the converged value of the estimation in Scenario 1.

For Scenario 3, the rate of measurement is down to 50%, but the estimation does still converge to a value quite close to the original estimation. The estimate is becoming more noisy, but the estimation is still passable. In Scenario 4 however, the noise in the estimation starts to get big, and for scenarios 5 and 6, the estimation is not longer usable because of large errors and instability.

Consequently, a Kalman filter with intermittent observations can be used, under the condition that the rate of measurements is higher than a certain limit. For this simulation, a rate lower than 50% is not recommended. However, this value will vary with implementation and tuning of the model, and can not be used as a rule for all intermittent estimations. It does, however, confirm that if the time between measurements is too long, large errors will occur.

# Chapter 8

# Concluding Remarks

## 8.1 Conclusions

This master thesis presents an algorithm for detection and tracking of targets in satellite images. The algorithm also includes a classification feature for distinguishing between vessel and ice targets.

The tracking capabilities of the algorithm was tested on a set of satellite images from the Greenland East Coast. From this, it was concluded that for the detection to be successful, the targets must have a distinct shape with a brightness return which is moderately different than the background. This meant that the detection of targets surrounded by ice proved troublesome. However, for targets which were in close proximity to ice, but not completely enclosed by it, the detection part of the algorithm proved effective.

The geometrical representation of a target always deviates in between images. This is taken into account in the tracking algorithm, however, for small targets, the deviations can become very large. The limit for the allowed deviations have to be increased accordingly, however, this can also increase the risk of getting false alarms in the matching process. The case study showed that for targets only spanning a few pixels, tracking is not possible.

The classification feature of the algorithm is very simple. It introduces a speed limit to separate between ice and vessel targets. In the case study, the speed limit was set to 0.25 $m/s$, which was tested, and proved to be a good limit. However, since the shape of the vessels in the case study were indistinguishable, it was impossible to successfully track them by the tracking algorithm. Thus, a valid calculation of speed was not possible.

By investigating the brightness returns of different targets in dual-polarized imagery, it was found that vessels had a higher HV/HH area ratio than ice targets. This could be used to discriminate between these two target types.

By analyzing patterns of target motions, it was found that ice vessels usually follow the current. In contrary to vessels, the motion of ice can thus be predicted, if the current in the area is known. This information can also be used to distinguish between target types.

Lastly, a dynamic model for iceberg drift was made and simulated. With a Kalman filter it was possible to estimate the velocity of the iceberg, by measuring the position of the target, and the wind, wave and current forces working on it. Theoretically, measurements for the position of the iceberg could be found from using the tracking algorithm on satellite images of the target. This would result in a better estimation of speed than the average speed calculation used in the rest of the thesis. Unfortunately, the performance of the estimation is hugely dependent on the frequency of the measurements. This can prove problematic, due to the intermittent nature of satellite image acquisition.

The model was not tested on a real case scenario, and is therefore only theoretical.

## 8.2 Recommendations for Further Work

For this thesis, the algorithm was only tested on images with a very high swath width. For further improvements, the algorithm could be tested on satellite images with other swath widths and resolutions.

A choice was made not to link the positional data from the georeferenced images with the tracking algorithm in MATLAB. The positional data was instead found using an external toolbox, NEST. By automating this process, and making the positional data directly available in the algorithm, the images used in the classification feature would no longer need to be from the exact same geographical location. In addition, by having positional data available, a method for automatically matching targets with vessels identified by AIS data could be made.

Due to the lack of proper current data, the model for iceberg drift was not tested with measurements from the satellite images. Further work on the model should include combining it with weather data and positional data from images. By doing this, another classification feature could be added by using hypothesis testing to distinguish free-floating icebergs from human-controlled vessels.

# Bibliography


Aagaard, K. and Coachman, L. K. (1968), 'The east greenland current north of denmark strait: part i', *Arctic* pp. 181–200.

Alexandrov, V., Sandven, S., Kloster, K., Bobylev, L. and Zaitsev, L. (2004), 'Comparison of sea ice signatures in okean and radarsat radar images for the northeastern barents sea', *Canadian journal of remote sensing* **30**(6), 882–892.

Anderberg, M. (1973), *Cluster analysis for applications*, Academic Press, London.

Banfield, J. D. and Raftery, A. E. (1992), 'Ice floe identification in satellite images using mathematical morphology and clustering about principal curves', *Journal of the American Statistical Association* **87**(417), 7–16.

Bersch, M. (1995), 'On the circulation of the northeastern north atlantic', *Deep Sea Research Part I: Oceanographic Research Papers* **42**(9), 1583–1607.

Beucher, S. (1994), Watershed, hierarchical segmentation and waterfall algorithm, *in* 'Mathematical morphology and its applications to image processing', Springer, pp. 69–76.

Beucher, S. and Lantuéjoul, C. (1979), Use of watersheds in contour detection, *in* 'International workshop on image processing, real-time edge and motion detection'.

Bigg, G. R., Wadley, M. R., Stevens, D. P. and Johnson, J. A. (1997), 'Modelling the dynamics and thermodynamics of icebergs', *Cold Regions Science and Technology* **26**(2), 113–135.

Blunt, J. D., Garas, V. Y., Matskevitch, D. G., Hamilton, J. M. and Kumaran, K. (2012), Image analysis techniques for high arctic deepwater operation support, *in* 'OTC Arctic Technology Conference', Offshore Technology Conference.

Brekke, C. and Anfinsen, S. N. (2011), 'Ship detection in ice-infested waters based on dual-polarization sar imagery', *Geoscience and Remote Sensing Letters, IEEE* **8**(3), 391–395.

Brown, R. G. and Hwang, P. Y. C. (2012), *Introduction to random signals and applied Kalman filtering*, John Wiley & Sons, Inc, 111 River Street, Hoboken.

Dierking, W. and Busche, T. (2006), 'Sea ice monitoring by l-band sar: An assessment based on literature and comparisons of jers-1 and ers-1 imagery', *Geoscience and Remote Sensing, IEEE Transactions On* **44**(4), 957–970.

Dierking, W. and Dall, J. (2007), 'Sea-ice deformation state from synthetic aperture radar imagery—part i: Comparison of c-and l-band and different polarization', *Geoscience and Remote Sensing, IEEE Transactions on* **45**(11), 3610–3622.

Dierking, W. and Dall, J. (2008), 'Sea ice deformation state from synthetic aperture radar imagery—part ii: Effects of spatial resolution and noise level', *Geoscience and Remote Sensing, IEEE Transactions on* **46**(8), 2197–2207.

Egset, C. and Nost, E. (2007), 'Oil spill detection system based on marine x-band radar', *Sea Technology* **48**(4), 41.

Eik, K. (2009*a*), Iceberg deterioration in the barents sea, *in* 'Proceedings-International Conference on Port and Ocean Engineering under Arctic Conditions'.

Eik, K. (2009*b*), 'Iceberg drift modelling and validation of applied metocean hindcast data', *Cold Regions Science and Technology* **57**(2), 67–90.

Elachi, C. and Van Zyl, J. J. (2006), *Introduction to the physics and techniques of remote sensing*, Vol. 28, John Wiley & Sons.

English, J., Hewitt, R., Power, D. and Tunaley, J. (2013), Ice-sais—space-based ais and sar for improved ship and iceberg monitoring, *in* 'Radar Conference (RADAR), 2013 IEEE', IEEE, pp. 1–6.

ESA (2015), 'Specifications for the Advanced Synthetic Aperture Radar (ASAR).', [Online] Available: `https://earth.esa.int/web/guest/missions/esa-operational-eo-missions/envisat/instruments/asar`. (May, 2015).

Ezman, A., Murphy, D., Fogt, V. and Reed, S. (1991), 'Forward-looking airborne radar (flar) evaluation', *International Ice Patrol Technical Report* pp. 93–01.

Faltinsen, O. (1990), *Sea loads on ships and offshore structures*, Vol. 1, Cambridge university press.

Foldvik, A., Aagaard, K. and Tørresen, T. (1988), 'On the velocity field of the east greenland current', *Deep Sea Research Part A. Oceanographic Research Papers* **35**(8), 1335–1354.

Gade, M., Alpers, W., Bao, M. and Huhnerfuss, H. (1996), Measurements of the radar backscattering over different oceanic surface films during the sir-c/x-sar campaigns, *in* 'Geoscience and Remote Sensing Symposium, 1996. IGARSS'96.'Remote Sensing for a Sustainable Future.', International', Vol. 2, IEEE, pp. 860–862.

Gladstone, R. and Bigg, G. (2002), 'Satellite tracking of icebergs in the weddell sea', *Antarctic Science* **14**(03), 278–287.

Gonzalez, R. C. and Woods, R. E. (2002), *Digital Image Processing*, second edition edn, Prentice-Hall, Inc, Upper Saddle River, New Jersey.

Grimaud, M. (1992), New measure of contrast: the dynamics, *in* 'San Diego'92', International Society for Optics and Photonics, pp. 292–305.

Gyory, J., Mariano, A. and Ryan, E. (2015), 'The East Greenland Current', [Online] Available: `http://oceancurrents.rsmas.miami.edu/atlantic/east-greenland.html`. (May, 2015).

Haarpaintner, J. (2006), 'Arctic-wide operational sea ice drift from enhanced-resolution quikscat/seawinds scatterometry and its validation', *Geoscience and Remote Sensing, IEEE Transactions on* **44**(1), 102–107.

Haarpaintner, J. and Solbø, S. (2007), 'Automatic ice-ocean discrimination in sar imagery', *Norut IT-report* **6**, 28.

Hall, J. A., Bigg, G. R. and Hall, R. (2012), 'Identification and tracking of individual sea ice floes from envisat wide swath sar images: a case study from fram strait', *Remote Sensing Letters* **3**(4), 295–304.

Hannevik, T. (2012), 'Radarsat-2 new modes', *FFI-report 2012/01094* .

Howell, C., Mills, J., Power, D., Youden, J., Dodge, K., Randell, C., Churchill, S. and Flett, D. (2006), A multivariate approach to iceberg and ship classification in hh/hv asar data, *in* 'Geoscience and Remote Sensing Symposium, 2006. IGARSS 2006. IEEE International Conference on', IEEE, pp. 3583–3586.

Howell, C., Youden, J., Lane, K., Power, D., Randell, C. and Flett, D. (2004), Iceberg and ship discrimination with envisat multipolarization asar, *in* 'Geoscience and Remote Sensing Symposium, 2004. IGARSS'04. Proceedings. 2004 IEEE International', Vol. 1, IEEE.

Isaacson, M. (1988), Influence of wave drift force on ice mass motions, *in* 'Proceedings of the Seventh International Conference on Offshore Mechanics and Arctic Engineering, OMAE'88', pp. 125–130.

Kalman, R. E. (1960), 'A new approach to linear filtering and prediction problems', *Journal of Fluids Engineering* **82**(1), 35–45.

Kubat, I., Sayed, M., Savage, S. B. and Carrieres, T. (2005), 'An operational model of iceberg drift', *International Journal of Offshore and Polar Engineering* **15**(2), 125–131.

Kumaran, K. (2012), 'Geophysical data texture segmentation using double-windowed clustering analysis'. US Patent App. 13/408,419.

Kwok, R., Curlander, J. C., McConnell, R. and Pang, S. S. (1990), 'An ice-motion tracking system at the alaska sar facility', *Oceanic Engineering, IEEE Journal of* **15**(1), 44–54.

Kwok, R. and Rothrock, D. (2009), 'Decline in arctic sea ice thickness from submarine and icesat records: 1958–2008', *Geophysical Research Letters* **36**(15).

Kwok, R. and Rothrock, D. A. (1999), 'Variability of fram strait ice flux and north atlantic oscillation', *Journal of Geophysical Research: Oceans (1978–2012)* **104**(C3), 5177–5189.

Lane, K., Power, D., Chakraborty, I., Youden, J., Randell, C., McClintock, J. and Flett, D. (2002), Radarsat-1 synthetic aperture radar iceberg detection performance adro-2 a223, *in* 'Geoscience and Remote Sensing Symposium, 2002. IGARSS'02. 2002 IEEE International', Vol. 4, IEEE, pp. 2273–2275.

Langlois, A. and Barber, D. G. (2007), 'Passive microwave remote sensing of seasonal snow-covered sea ice', *Progress in Physical Geography* **31**(6), 539–573.

Larssen, G. (2014), *Ide detection and tracking based on satellite and radar images*. Project thesis, as a part of MSc in Marine Cybernetics, NTNU.

Liu, A. K., Martin, S. and Kwok, R. (1997), 'Tracking of ice edges and ice floes by wavelet analysis of sar images', *Journal of Atmospheric and Oceanic Technology* **14**(5), 1187–1198.

Lubin, D. and Massom, R. (2006), *Polar Remote Sensing: Volume II: Ice Sheets*, Springer Science & Business Media.

MacQueen, J. et al. (1967), Some methods for classification and analysis of multivariate observations, *in* 'Proceedings of the fifth Berkeley symposium on mathematical statistics and probability', Vol. 1, California, USA, pp. 281–297.

Madigan, D. (2012), 'What is cluster analysis?', lecture notes distributed in Statistics W2025 at Columbia University.

Mariano, A., Ryan, E., Perkins, B. and Smithers, S. (2015), 'TThe Mariano Global Surface Velo city Analysis 1.0', [Online] Available: `http://www.rsmas.miami.edu/personal/eryan/tech-reports/mgsva.pdf`. (May, 2015).

Marko, J., Fissel, D. and Borg, K. (2003), 'Ice-type characterization in a marginal ice zone using radarsat and ice-profiling sonar: Tools for structural design and navigation planning in ice infested waters', *Presented at POAC03 June* **16**, 19.

Otsu, N. (1975), 'A threshold selection method from gray-level histograms', *Automatica* **11**(285-296), 23–27.

O'Connell, B. (2006), Marine radar for improved ice detection, *in* 'Proceedings of the 8th International Conference on Ships and Marine Structures in Ice (ICETECH 2008)'.

Power, D., Youden, J., Lane, K., Randell, C. and Flett, D. (2001), 'Iceberg detection capabilities of radarsat synthetic aperture radar', *Canadian Journal of Remote Sensing* **27**(5), 476–486.

Prewitt, J. and Mendelsohn, M. L. (1966), 'The analysis of cell images*', *Annals of the New York Academy of Sciences* **128**(3), 1035–1053.

Puestow, T., Parsons, L., Zakharov, I., Cater, N., Bobby, P., Fuglem, M., Parr, G., Jayasiri, A., Warren, S. and Warbanski, G. (2013), 'Oil spill detection and mapping in low visibility and ice: surface remote sensing', *Report from Joint Industry Programme* **5.1**.

Sandven, S., Babiker, M. and Kloster, K. (2007), 'Iceberg observations in the barents sea by radar and optical satellite images', *Proceedings for Envisat Symposium* .

Shaw, V., Berchi, F. and McRue, W. (1988), Auto and cross correlation analysis of environment, system and target parameters for iceberg detection using airborne radar, *in* 'Geoscience and Remote Sensing Symposium, 1988. IGARSS'88. Remote Sensing: Moving Toward the 21st Century., International', Vol. 2, IEEE, pp. 809–816.

Sheng, G., Yang, W., Deng, X., He, C., Cao, Y. and Sun, H. (2012), 'Coastline detection in synthetic aperture radar (sar) images by integrating watershed transformation and controllable gradient vector flow (gvf) snake model', *Oceanic Engineering, IEEE Journal of* **37**(3), 375–383.

Silva, T. A. and Bigg, G. R. (2005), 'Computer-based identification and tracking of antarctic icebergs in sar images', *Remote sensing of Environment* **94**(3), 287–297.

Silva, T. A. M. d. (2006), Quantifying Antarctic icebergs and their melting in the ocean, PhD thesis, University of Sheffield, Department of Geography.

Sinopoli, B., Schenato, L., Franceschetti, M., Poolla, K., Jordan, M. I. and Sastry, S. S. (2004), 'Kalman filtering with intermittent observations', *Automatic Control, IEEE Transactions on* **49**(9), 1453–1464.

Skolnik, M. (1990), '1990: Radar handbook', *New York: McGraw-lIill* .

Smith, SD. & Donaldson, N. (1987), 'Dynamic modelling of iceberg drift using current profiles', *Canadian technical report of hydrography and ocean science* **91**.

Spreen, G., Kern, S., Stammer, D., Forsberg, R. and Haarpaintner, J. (2006), 'Satellite-based estimates of sea-ice volume flux through fram strait', *Annals of Glaciology* **44**(1), 321–328.

USCG, U. S. C. G. (2015), 'Automatic Identification System Messages', [Online] Available: `http://www.navcen.uscg.gov/?pageName=AISMessages`. (May, 2015).

Van Zyl, J. and Kim, Y. (2011), *Synthetic Aperture Radar Polarimetry*, John Wiley & Sons, New Jersey.

Vincent, L. and Soille, P. (1991), 'Watersheds in digital spaces: an efficient algorithm based on immersion simulations', *IEEE transactions on pattern analysis and machine intelligence* **13**(6), 583–598.

Walker, N. P., Partington, K. C., Van Woert, M. L. and Street, T. L. (2006), 'Arctic sea ice type and concentration mapping using passive and active microwave sensors', *Geoscience and Remote Sensing, IEEE Transactions on* **44**(12), 3574–3584.

Williams, R., Rees, W. and Young, N. (1999), 'A technique for the identification and analysis of icebergs in synthetic aperture radar images of antarctica', *International Journal of Remote Sensing* **20**(15-16), 3183–3199.

Woodgate, R. A., Fahrbach, E. and Rohardt, G. (1999), 'Structure and transports of the east greenland current at 75 n from moored current meters', *Journal of Geophysical Research: Oceans (1978–2012)* **104**(C8), 18059–18072.

Woodhouse, I. H. (2005), *Introduction to microwave remote sensing*, CRC press.

Xu, C. and Prince, J. L. (1998), 'Snakes, shapes, and gradient vector flow', *Image Processing, IEEE Transactions on* **7**(3), 359–369.

Zhang, Q. e. a. (2012), Image processing for the analysis of an evolving broken-ice field in model testing.

Zhang, Q. and Skjetne, R. (2013), 'Image processing for identification of sea-ice floes and the floe size distributions'.

Zhang, Q., Skjetne, R. and Su, B. (2013), Automatic image segmentation for boundary detection of apparently connected sea-ice floes, *in* 'proc. 22nd Int. Conf. Port and Ocean Engineering under Arctic Conditions (POAC 2013)'.

# Appendices

# Appendix A

# Satellite Information



Table A.1: No longer operational satellites with active or passive sensors

| Name | Operator | Sensor type | Resolution | Swath width | Beam modes and polarizations |
|---|---|---|---|---|---|
| ALOS | JAXA | SAR with L-band | 2.5-100 m | 7-350 km | 5 polarization modes |
| ENVISAT | European Space Agency (ESA) | Advanced SAR with C-Band. | 30-1000 m | 5-400 km | |
| ERS-1,2 | ESA | SAR with C-band. | 30 m | 100 km | |
| IKONOS | GeoEye/DigitalGlobe | Panchromatic and multispectral imagery (optical) | 0.8 - 4 m | 11 km | |
| Quickbird | DigitalGlobe | Multispectral and panchromatic (optical) | 0.6 - 2.4 m | Not available | Average revisit time was 2-3 days |
| RADARSAT-1 | CSA | SAR with C-Band | 8-100 m | 50-500 km | 7 beam modes and 35 beam positions |

Table A.2: Operational satellites with active or passive sensors

| Name | Operator | Sensor type | Resolution | Swath width | Other information |
|---|---|---|---|---|---|
| ALOS-2 | Japan Aerospace Exploration Agency (JAXA) | SAR with L-Band | 1-100 m | 25-490 km | Has three imaging modes: SpotLight, StripMap and ScanSAR. |
| Blackbridge (Earlier RapidEye) | MacDonald Dettwiler (MDA) | Panchromatic and multispectral imagery (optical) | 5 m | 77 km | Is actually a constellation of five identical satellites. Has a global revisit time of 1 day. |
| COSMO-SkyMed 1,2,3,4 | The Italian Space Agency (ASI) | SAR with X-Band | 1-100 m. | 10-200 km | Capable of both single and dual-polarization. Has three imaging modes: SpotLight, StripMap and ScanSAR. |
| Deimos-2 | Deimos Space | Panchromatic and multispectral imagery (optical) | 1-4 m | 12 km | |
| GeoEye-1 | GeoEye | Panchromatic and multispectral imagery (optical) | 0.4-1.65 m | 15 km | Revisit time >3 days. |
| RADARSAT-2 | Canadian Space Agency (CSA) | SAR with C-Band. | 1-160 m | 18-500 km | Has 18 beam modes. Capable of single, dual and quad polarizations. |
| RISAT-1 | Indian Space Research Organisation (ISRO) | SAR with C-Band | 1-50 m | Not available | |
| SENTINEL-1A | ESA | SAR with C-Band | 5-40 m | 20-250 km | Capable of dual-polarization. Has four operational modes: StripMap, Wide-Swath, Extra-Wide Swath and Wave mode. |
| SPOT 6,7 | The French space agency (CNES) | Panchromatic and multispectral imagery (optical) | 1.5-6 m | 60 km | Capacity to acquire up to 3 million $km^2$ daily |
| TanDEM-X | The German Aerospace Center (DLR) and EADS Astrium | SAR with X-Band. | 1-18.5 m | 5-150 km | Is the twin satellite of TerraSAR-X. |
| TerraSAR-X | DLR and EADS Astrium. | SAR with X-band | 1-18.5 m | 5-150 km | Has three imaging modes: SpotLight, StripMap and ScanSAR. |
| WorldView-1 | DigitalGlobe | Panchromatic (optical) | 0.5 m | NA | Average revisit time is 1.7 days |
| WorldView-2 | DigitalGlobr | Multispectral and panchromatic (optical) | 0.5 - 1.8 m | NA | Average revisit time is 1.1 day |

Table A.3: RADARSAT-2 beam modes (Hannevik, 2012).

| Beam mode | Appr. nominal swath width | Swath width for regular corresponding mode | Appr. resolution | | Appr. incidence angle | Polarization (pol) |
|---|---|---|---|---|---|---|
| | | | Range | Azimuth | | |
| Spotlight | 18 km | NA | 1.6-4.6 m | 0.8 m | 20°-49° | Single-pol (HH, VV, HV or VH) |
| Ultra-Fine | 20 km | NA | 1.6-4.6 m | 2.8 m | 20° - 49° | |
| Wide Ultra-Fine | 50 km | 20 km | 1.6-3.3 m | 2.8 m | 30°-50° | |
| Multi-Look Fine | 50 km | NA | 3.1-10.4 m | 4.6-7.6 m | 30° - 50° | |
| Wide Multi-Look Fine | 90 km | 50 km | 3.1-10.4 m | 4.6-7.6 m | 29°-50° | |
| Fine | 50 km | NA | 5.2-10.4 m | 7.7 m | 30° - 50° | Single-pol or dual-pol |
| Wide Fine | 120-170 km | 50 km | 5.2-15.2 m | 7.7 m | 20°-45° | |
| Standard | 100 km | NA | 9-26.8 m | 7.7-24.7 m | 20° - 49° | |
| Wide | 120-170 km | NA | 13.5-40 m | 7.7-24.7 m | 20° - 45° | |
| ScanSAR Narrow | 300 km | NA | 37.7-79.9 m | 60 m | 20° - 47° | |
| ScanSAR Wide | 450-500 km | NA | 72.1-160 m | 100 m | 20° - 49° | |
| Extended High | 70 – 80 km | NA | 13.5-18.2 m | 7.7-24.7 m | 49° - 60° | Single-pol (HH) |
| Extended Low | 170 km | NA | 9-52.7 m | 7.7-24.7 m | 10° - 23° | |
| Fine Quad-Pol | 25 km | NA | 5.2-16.5 m | 7.6 m | 18° - 49° | Quad-pol |
| Wide Fine Quad-Pol | 50 km | 25 km | 5.2-17.3 m | 7.6 m | 18°-42° | |
| Standard Quad-Pol | 25 km | NA | 9-28.6 m | 7.6 m | 18° - 49° | |
| Wide Standard Quad-Pol | 50 km | 25 km | 9-30.0 m | 7.6 m | 18°-42° | |

# Appendix B

# Overview of the Vessels Identified from the AIS-Data

Table B.1: Overview of vessels identified from the AIS-data

| Vessel number | MMSI number | Name | Type | Dimensions | Images identified in |
|---|---|---|---|---|---|
| 1 | 273452600 | AKADEMIK SHATSKIY | Research vessel | 82 x 15 m | Images 1-5, 7, 9-13 and 15. |
| 2 | 265829000 | BALDER VIKING | Tug/Supply vessel | 83.7 x 18.04 m | Images 11-5, 7, 9-13 and 15. |
| 3 | 231053000 | ARCTIC VIKING | Fishing trawler | 114 x 17 m | Image 2. |
| 4 | 265182000 | ODEN | Icebreaker | 107.42 x 31.08 m | Images 2-7, 9-13 and 15. |
| 5 | 273454860 | POLAR PIONEER | Research vessel | 71 x 13 m | Image 10 |
| 6 | 246573000 | PLANCIUS | Passenger ship | 60 x 40 m | Image 11 |
| 7 | 257219000 | NORTHEASTERN | Sealer | 57.91 x 8.54 m | Image 11 |
| 8 | 258236000 | LANCE | Research/survey vessel | 60.71 x 12.65 m | Image 15 |

# Appendix C

# Geographical Data and Timestamps

## C.1 Satellite Images

Table C.1: Dates, time and corresponding timestamps for the satellite images

| Image number | Date | Time | Timestamp |
|---|---|---|---|
| 1 | 20-Aug-2013 | 08:24:49 | 1376987089 |
| 2 | 21-Aug-2013 | 07:55:35 | 1377071735 |
| 3 | 22-Aug-2013 | 07:26:19 | 1377156379 |
| 4 | 23-Aug-2013 | 08:37:20 | 1377247020 |
| 5 | 24-Aug-2013 | 08:08:07 | 1377331687 |
| 6 | 24-Aug-2013 | 16:26:33 | 1419092793 |
| 7 | 25-Aug-2013 | 07:38:51 | 1377416331 |
| 8 | 26-Aug-2013 | 08:50:13 | 1377507013 |
| 9 | 26-Aug-2013 | 17:07:29 | 1377536849 |
| 10 | 27-Aug-2013 | 08:20:38 | 1377591638 |
| 11 | 28-Aug-2013 | 07:51:24 | 1377676284 |
| 12 | 29-Aug-2013 | 17:20:01 | 1377796801 |
| 13 | 30-Aug-2013 | 08:33:09 | 1377851589 |
| 14 | 30-Aug-2013 | 16:51:38 | 1377881498 |
| 15 | 31-Aug-2013 | 08:03:56 | 1377936236 |

Table C.2: Overview of the geographical data (DMS) for each image

| Image number | Center | | Upper left | | Upper right | | Lower left | | Lower right | |
|---|---|---|---|---|---|---|---|---|---|---|
| | Latitude | Longitude | Latitude | Longitude | Latitude | Longitude | Latitude | Longitude | Latitude | Longitude |
| 1 | 78°08'03" N | 17°26'21" W | 79°00'06" N | 1°31'43" W | 80°55'33" N | 26°33'47" W | 75°07'59" N | 11°58'18" W | 76°33'54" N | 30°27'59" W |
| 2 | 77°37'46" N | 11°03'49" W | 78°34' N | 4°06'37" E | 80°24'02" N | 19°54'32" W | 74°38'56" N | 5°37'36" W | 76°01'57" N | 23°29'57" W |
| 3 | 77°14'18" N | 4°22'12" W | 78°13'18" N | 10°17'28" E | 79°59'52" N | 13°00'27" W | 74°16'09" N | 1°02'07" E | 75°37'22" N | 16°24'01" W |
| 4 | 78°23'06" N | 20°05'53" W | 79°12'50" N | 3°49'44" W | 81°10'52" N | 29°21'48" W | 75°22'50" N | 14°36'48" W | 76°50'08" N | 33°25'25" W |
| 5 | 77°49'53" N | 13°51'03" W | 78°44'20" N | 1°35'27" E | 80°36'17" N | 22°48'37" W | 74°50'55" N | 8°23'25" W | 76°14'59" N | 26°30'21" W |
| 6 | 78°39'09" N | 9°24'55" W | 78°25'05" N | 9°56'36" W | 78°40'01" N | 8°06'34" W | 78°37'56" N | 10°43'03" W | 78°53'09" N | 8°51'51" W |
| 7 | 77°23'13" N | 7°14'53" W | 78°21'22" N | 7°37'53" E | 80°09'30" N | 15°57'35" W | 74°24'21" N | 1°50'24" W | 75°46'22" N | 19°26'37" W |
| 8 | 78°31'49" N | 12°16'54" W | 78°31'25" N | 10°59'21" W | 78°45'25" N | 12°53'39" W | 78°18'09" N | 11°41'35" W | 78°31'54" N | 13°34'28" W |
| 9 | 78°20'08" N | 5°32'53" W | 75°19'58" N | 11°01'16" W | 76°46'48" N | 7°42'07" E | 79°10'31" N | 21°43'56" W | 81°07'47" N | 3°40'31" E |
| 10 | 78°04'13" N | 16°29'28" W | 78°56'45" N | 0°40'37" W | 80°51'36" N | 25°34'27" W | 75°04'18" N | 11°01'54" W | 76°29'56" N | 29°26'40" W |
| 11 | 77°33'35" N | 10°06'31" W | 78°30'15" N | 4°58'54" E | 80°19'50" N | 18°54'56" W | 74°34'46" N | 4°40'39" W | 75°57'35" N | 22°28'41" W |
| 12 | 78°07'28" N | 8°18'42" W | 75°07'47" N | 13°46'19" W | 76°33'33" N | 4°41'13" E | 78°59'30" N | 24°10'34" W | 80°54'39" N | 0°47'23" E |
| 13 | 78°19'07" N | 19°09'47" W | 79°09'20" N | 2°59'40" W | 81°06'45" N | 28°23'21" W | 75°18'59" N | 13°40'57" W | 76°45'59" N | 32°24'36" W |
| 14 | 78°35'23" N | 12°41'43" W | 78°21'38" N | 13°17'04" W | 78°35'32" N | 11°23'27" W | 78°34'54" N | 13°59'56" W | 78°49'04" N | 12°04'53" W |
| 15 | 77°45'29" N | 12°53'38" W | 78°40'28" N | 2°28'06" E | 80°32'03" N | 21°48'51" W | 74°46'21" N | 7°26'35" W | 76°10'16" N | 25°29'06" W |

## C.2 Vessels Identified

Table C.3: Identified vessel positions in decimal format

| Image number | Vessel number | Interpolated position | | Manually found position | |
|---|---|---|---|---|---|
| | | Latitude [°] | Longitude [°] | Latitude [°] | Longitude [°] |
| 1 | 1 | 76.4318 | -16.2282 | 76.42959 | -16.226862 |
| | 2 | 76.3728 | -16.323 | 76.36773 | -16.315145 |
| 2 | 1 | 76.6147 | -13.1238 | 76.6129 | -13.1086 |
| | 2 | 76.6144 | -13.116 | 76.6123 | -13.1009 |
| | 3 | 78.2364 | 1.4849 | 78.2362 | 1.4973 |
| | 4 | 77.782 | -2.2231 | 77.7833 | -2.2162 |
| 3 | 1 | 76.6856 | -12.0668 | 76.6883 | -12.0649 |
| | 2 | 76.6987 | -12.2763 | 76.7010 | -12.2765 |
| | 4 | 76.6819 | -13.2322 | 76.6610 | -13.2599 |
| 4 | 1 | 76.7907 | -14.9955 | Not found | Not found |
| | 2 | 76.794 | -15.0153 | Not found | Not found |
| | 4 | 78.2561 | -10.4175 | 78.2475 | -10.4259 |
| 5 | 1 | 78.0565 | -14.2965 | 78.0576 | -14.2868 |
| | 2 | 78.0585 | -14.293 | 78.0592 | -14.2829 |
| | 4 | 78.5913 | -9.268 | 78.5916 | -9.2564 |
| 6 | 4 | Not available | Not available | 78.6822 | -09.0702 |
| 7 | 1 | 78.5561 | -12.7216 | 78.5551 | -12.6983 |
| | 2 | 78.5546 | -12.7177 | 78.5529 | -12.6977 |
| | 4 | 78.7294 | -8.6935 | 78.7291 | -8.6829 |
| 8 | No vessels found | | | | |
| 9 | 1 | 77.1222 | -12.0626 | 77.1213 | -12.0588 |
| | 2 | 77.122 | -12.0556 | 77.1210 | -12.0495 |
| | 4 | 78.9206 | -8.8885 | 78.9207 | -8.9034 |
| 10 | 1 | 76.8964 | -8.0809 | Not found | Not found |
| | 2 | 76.897 | -8.0673 | Not found | Not found |
| | 4 | 78.5772 | -12.5099 | 78.5799 | -12.5099 |

*Continued on next page*

Table C.3 – *Continued from previous page*

| Image number | Vessel number | Interpolated position | | Manually found position | |
|---|---|---|---|---|---|
| | | Latitude [°] | Longitude [°] | Latitude [°] | Longitude [°] |
| | 8 | 76.9409 | -9.4097 | Not found | Not found |
| 11 | 1 | 77.4631 | -10.869 | 77.4617 | -10.8561 |
| | 2 | 77.4602 | -11.716 | 77.4612 | -11.7093 |
| | 4 | 78.6521 | -13.4809 | 78.6617 | -13.4812 |
| | 9 | 76.126 | -8.8741 | 76.1244 | -8.8771 |
| | 10 | 77.4629 | -11.707 | 77.4612 | -11.7088 |
| 12 | 1 | 77.8094 | -13.8318 | 77.8125 | -13.8407 |
| | 2 | 77.8102 | -13.8384 | 77.8143 | -13.8492 |
| | 4 | 78.1168 | -11.0315 | 78.12 | -11.0723 |
| 13 | 1 | 77.5839 | -13.7275 | 77.5828 | -13.7205 |
| | 2 | 77.5782 | -13.7211 | 77.5826 | -13.7117 |
| | 4 | 78.0578 | -11.4857 | 78.0564 | -11.4910 |
| 14 | No vessels found | | | | |
| 15 | 1 | 77.5955 | -16.7087 | 77.5806 | -16.7402 |
| | 2 | 77.5978 | -16.6927 | 77.5801 | -16.7316 |
| | 4 | 77.6446 | -8.4635 | 77.6612 | -8.4207 |
| | 11 | 78.9035 | -4.0817 | 78.8982 | -4.1122 |

# Appendix D

# Source Code Contents

The MATLAB/SimuLink files for the algorithm and the ice drift model are added in a compressed zip-file called `sourcecode.zip`. The contents are split up into two main folders: "Detection and tracking" and "Iceberg drift modeling".

In addition the poster made in relation with the Master Thesis Poster Exhibition at the Center for Marine Technology is included.

## D.1 Detection and Tracking

This folder contains all the scripts used for detection, tracking and classification used in this thesis. The file `run.m` initiates the tracking process of a simple case, not using satellite images. The file `satrun2.m` initiates the tracking process tailored for satellite images. The file `classifyrun.m` initiates the tracking algorithm including the classification feature.

In addition the file used for processing of AIS data was included. It is called `AISanalyser.m`, and the input of it should be a .cvs file containing the MMSI vessel number, timestamp, latitude, longitude, speed and heading for the vessels.

The testimages used for the two synthetic test cases presented in the thesis is included in the folder "Testimages". Due to distribution rights the satellite images used in the thesis are not included.

## D.2 Iceberg Drift Modeling

This folder contains three subfolder: "Dynamic model", "Kalman filter" and "Kalman filter intermittent". These folders include the MATLAB and Simulink files for the iceberg drift model and the Kalman filter.

To run the program for the iceberg drift model, open the folder "Dynamic model" and run the MATLAB-file `run.m`.

To run the program for the Kalman filter with continuous observations, open the folder "Kalman filter" and run the MATLAB-file `run.m`.

To run the program for the Kalman filter with intermittent observations, open the folder "Kalman filter intermittent" and run the MATLAB-file "run.m".